

1

UNIVERSITY OF BRISTOL

2

DOCTORAL THESIS

3

4

Investigating, implementing, and creating methods for analysing large neuronal ensembles

5

6

Author:

Thomas J. DELANEY

Supervisors:

Dr. Cian O'DONNELL

Dr. Michael C. ASHBY

7

*A thesis submitted in fulfillment of the requirements
for the degree of Doctor of Philosophy*

8

in the

9

Biological Intelligence & Machine Learning Unit
Department of Computer Science

10

11

12

July 7, 2020

¹⁵ Declaration of Authorship

¹⁶ I, Thomas J. DELANEY, declare that this thesis titled, "Investigating, implementing, and
¹⁷ creating methods for analysing large neuronal ensembles" and the work presented in it are
¹⁸ my own. I confirm that:

- ¹⁹ • This work was done wholly or mainly while in candidature for a research degree at this
²⁰ University.
- ²¹ • Where any part of this thesis has previously been submitted for a degree or any other
²² qualification at this University or any other institution, this has been clearly stated.
- ²³ • Where I have consulted the published work of others, this is always clearly attributed.
- ²⁴ • Where I have quoted from the work of others, the source is always given. With the
²⁵ exception of such quotations, this thesis is entirely my own work.
- ²⁶ • I have acknowledged all main sources of help.
- ²⁷ • Where the thesis is based on work done by myself jointly with others, I have made
²⁸ clear exactly what was done by others and what I have contributed myself.

²⁹

³⁰ Signed:

³¹ _____

³² Date:

³³ _____

34

UNIVERSITY OF BRISTOL

35

Abstract

36

Engineering

37

Department of Computer Science

38

Doctor of Philosophy

39

**Investigating, implementing, and creating methods for analysing large neuronal
ensembles**

41

by Thomas J. DELANEY

42

The Thesis Abstract is written here (and usually kept to just this page). The page is kept centered vertically so can expand into the blank space above the title too...

44

Acknowledgements

45 The acknowledgments and the people to thank go here, don't forget to include your project

46 advisor...

⁴⁷ Contents

⁴⁸	Declaration of Authorship	iii
⁴⁹	Abstract	v
⁵⁰	Acknowledgements	vii
⁵¹	1 Introduction	1
⁵²	1.1 Overview	1
⁵³	2 Sensitivity of the spikes-to-fluorescence transform to calcium indicator and neu-	
⁵⁴	ron properties	7
⁵⁵	2.1 Introduction	8
⁵⁶	2.2 Results	10
⁵⁷	2.2.1 A biophysical computational model can generate accurate fluores-	
⁵⁸	cence traces from spike trains	10
⁵⁹	2.2.2 Spike inference algorithms perform similarly on real data compared	
⁶⁰	with time series simulated from the model	11
⁶¹	2.2.3 Relative effects of various buffers to the fluorescence signal	12
⁶²	2.2.4 Spike inference accuracy is sensitive to indicator properties, and likely	
⁶³	varies within and between cells	13
⁶⁴	2.2.5 Single spike inference accuracy drops for high firing rates, but firing	
⁶⁵	rate itself can be estimated from mean fluorescence amplitude	18
⁶⁶	2.3 Discussion	21
⁶⁷	2.4 Methods	23
⁶⁸	2.4.1 Calcium dynamics model	23
⁶⁹	Photon release & capture	25
⁷⁰	2.4.2 Parameter optimisation	26
⁷¹	Fixed parameters	27
⁷²	2.4.3 Julia	27

73	2.4.4	Spike inference	29
74		Comparing spike inference quality	31
75	2.4.5	Perturbation analysis	31
76	2.4.6	Signal-to-noise ratio	31
77	2.4.7	Data sources	32
78	3	Functional networks expand across anatomical boundaries as correlation time-scale increases	33
79	3.1	Introduction	34
80	3.2	Results	35
81	3.2.1	Average correlation size increases with increasing time bin width	35
82	3.2.2	Goodness-of-fit for Poisson and Gaussian distributions across increasing time bin widths	36
83	3.2.3	Differences between and inter- and intra- regional correlations decrease with increasing bin width	38
84	3.2.4	Connected and divided structure in correlation based networks reduces in dimension with increasing bin width	41
85	3.2.5	Detecting communities in correlation based networks	42
86	3.2.6	Functional communities resemble anatomical division at short timescales	42
87	3.2.7	Conditional correlations & signal correlations	46
88	3.2.8	Absolute correlations and negative rectified correlations	50
89	3.3	Discussion	53
90	3.4	Data	56
91	3.4.1	Brain regions	56
92	3.4.2	Video recordings	57
93	3.5	Methods	57
94	3.5.1	Binning data	57
95	3.5.2	Correlation coefficients	57
96		Total correlations, r_{SC}	58
97		Shuffled total correlations	58
98		Separating Correlations & Anti-correlations	58
99	3.5.3	Conditioning on behavioural data	59
100		Linear regression	59
101		Elastic net regularisation	59

106	Conditional covariance	60
107	Measures of conditional correlation	61
108	3.5.4 Information Theory	61
109	Entropy $H(X)$	61
110	Maximum entropy limit	62
111	Mutual Information $I(X; Y)$	63
112	Variation of Information $VI(X, Y)$	64
113	Measuring entropies & mutual information	65
114	3.5.5 Network analysis	65
115	Correlation networks	65
116	Rectified correlations	65
117	Sparsifying data networks	66
118	Communities	66
119	Weighted configuration model	66
120	Sparse weighted configuration model	66
121	Spectral rejection	67
122	Node rejection	68
123	Community detection	68
124	3.5.6 Clustering Comparison	69
125	Adjusted Rand Index	69
126	Clusterings as random variables	70
127	Information based similarity measures	70
128	Information based metrics	71
129	Comparing detected communities and anatomical divisions	71
130	4 A simple two parameter distribution for modelling neuronal activity and capturing neuronal association	73
131	4.1 Introduction	74
132	4.2 Data	75
133	4.2.1 Experimental protocol	75
134	4.3 Methods	76
135	4.3.1 Binning data	76
136	4.3.2 Number of <i>active</i> neurons	76
137	4.3.3 Moving windows for measurements	76

139	4.3.4	Fano factor	78
140	4.3.5	Probability Distributions suitable for modelling ensemble activity . .	78
141		Association	78
142		Binomial distribution	79
143		Beta-binomial distribution	79
144		Conway-Maxwell-binomial distribution	80
145	4.3.6	Fitting	82
146	4.3.7	Goodness-of-fit	84
147	4.4	Results	84
148	4.4.1	Increases in mean number of active neurons and variance in number of active neurons at stimulus onset in some regions	84
149		Primary visual cortex	85
150		Hippocampus	85
151		Thalamus	85
152	4.4.2	Conway-Maxwell-binomial distribution is usually a better fit than bi- nomial or beta-binomial	85
153	4.4.3	Conway-Maxwell-binomial distribution captures changes in associ- ation at stimulus onset	90
154	4.4.4	Replicating stimulus related quenching of neural variability	90
155	4.5	Discussion	92
159	5	Studies with practical limitations & negative results	95
160	5.1	Dynamic state space model of pairwise and higher order neuronal correlations	96
161	5.2	A multiscale model for hierarchical data applied to neuronal data	96
162	5.3	Discussion	98
164	Bibliography		99

165 List of Figures

166 2.1	A: Example spike train (blue) and the corresponding GCaMP6s fluorescence 167 trace (green), data replotted from (Berens et al., 2018). Inset shows zoomed 168 section of traces to highlight slow decay of GCaMP6s fluorescence relative 169 to spike time intervals. B: Schematic diagram of the neuron calcium and 170 GCaMP computational model. C: Good visual match of data fluorescence 171 trace (green) and model simulated fluorescence (orange) in response to an 172 identical spike train (blue).	9
173 2.2	A: Workflow to compare spike inference for real versus simulated fluores- 174 cence data. B: True positive rates achieved by three different spike inference 175 algorithms when applied to observed spike trains, and simulated spike trains. 176 Data points overlaid as blue circles. The performance is similar from real 177 and simulated data for each of the algorithms.	12
178 2.3	Calcium Buffering Dynamics (a) The proportions of bound and free cal- 179 cium concentrations within a cell, with the associated spike train. (b)-(f) The 180 dynamics of the concentration of (b) excited indicator bound calcium, (c) in- 181 dicator bound calcium, (d) immobile endogenous buffer bound calcium, (e) 182 mobile endogenous buffer bound calcium, and (f) free calcium in response to 183 an action potential at $\sim 23.2\text{s}$	14
184 2.4	(a) An example trace for each of the five pairs of values used for the binding 185 and unbinding rates of the fluorescent calcium indicator. (b) The signal-to- 186 noise ratio of the modelled fluorescence traces using each of the four per- 187 turbed values, and the experimental value. The SNRs for the two pairs with 188 values lower than the experimental value are lower than the experimental pair 189 or the higher value pairs. (c) The true-positive rates of the deconvolution al- 190 gorithm's predictions when inferring from the observed data, and inferring 191 from modelled traces using the perturbed and experimental values.	16

192	2.5 (a) An example trace for each of the five perturbed values for the concentration of fluorescent calcium indicator. The top two traces are produced by the lower perturbed values, the middle trace is produced by the experimental value, and the lowest two traces are produced when using the higher perturbed values. (b) The signal-to-noise ratio of the modelled fluorescence traces using each of the four perturbed values, and the experimental value. Extreme perturbations of the concentration either above or below the experimental level lowered the SNR. (c) The true-positive rates of the deconvolution algorithm's predictions when inferring from the observed data, and inferring from modelled traces using the perturbed and experimental values. We found that the algorithms performs equally badly on the two most extreme values, and performs equally well on the experimental value, and the next higher perturbed value.	17
205	2.6 (a) An example trace for each of the five perturbed values for the concentration of immobile endogenous buffer. (b) The signal-to-noise ratio of the modelled fluorescence traces using each of the four perturbed values, and the experimental value. The lower values for the immobile buffer produce the same SNR as the experimental value. But the higher perturbed values produce fluorescence traces with a lower SNR. (c) The true-positive rates of the deconvolution algorithm's predictions when inferring from the observed data, and inferring from modelled traces using the perturbed and experimental values.	19
214	2.7 Simulating fluorescence traces at different firing rates Example modelled traces created using simulated spike trains with a mean firing rate of 1Hz (left column), 5Hz (middle column), and 10Hz (right column). Note the difference in amplitude with different mean firing rates.	20
218	2.8 Inference quality and $\Delta F/F_0$ vs Firing rate (left) The spike inference accuracy when applied to 30 traces created using simulated spike trains with mean firing rates of 1, 5, and 10 Hz. (right) The mean $\Delta F/F_0$ across those 30 traces for each frequency.	21

222	3.1 (A) An example of the correlation coefficients between two different pairs 223 of cells, one where both cells are in the same brain region (intra-regional 224 pair), and one where both cells are in different brain regions (inter-regional 225 pair). The correlation coefficients have been measured using different time 226 bin widths, ranging from 5ms to 3s. Note the increasing amplitude of the 227 correlations with increasing bin width. (B) A raster plot showing the spike 228 times of each pair of cells.	36
229	3.2 Mean correlation coefficients measured from pairs of 50 randomly chosen 230 neurons. (A) All possible pairs, (B) positively correlated pairs, and (C) neg- 231 atively correlated pairs. (D) Mean and standard error of χ^2 test statistics for 232 Poisson and Gaussian distributions fitted to neuron spike counts.	37
233	3.3 (Left)The mean intra-region and inter-region correlations using all possible 234 pairs of \sim 500 neurons, spread across 9 different brain regions. (Right) 235 Courtesy of Stringer et al. (2019), mean inter-regional (out-of-area) correla- 236 tion coefficients vs mean intra-regional (within-area) correlation coefficients 237 for a bin width of 1.2s. Note that the intra-regional coefficients are higher in 238 each case.	39
239	3.4 The mean intra-regional correlations (coloured dots) and mean inter-regional 240 correlations (black dots) for a given region, indicated on the x-axis, for dif- 241 ferent time bin widths. Each black dot represents the mean inter-regional 242 correlations between the region indicated on the x-axis and one other region. 243 (A) shows these measurements when we used a time bin width of 5ms. (B) 244 shows these measurements when we used a time bin width of 1s. Note that 245 the difference between the mean inter-regional correlations and mean intra- 246 regional correlations is smaller for 1s bins.	40
247	3.5 Mean inter-regional (main diagonal) and intra-regional (off diagonal) corre- 248 lation coefficients. (A) Shows these measurements when spike times were 249 binned using 5ms time bins. (B) Shows the same, using 1s time bins. Note 250 that the matrices are ordered according to the main diagonal values, therefore 251 the ordering is different in each subfigure.	41

252 3.6	The number of dimensions in the k -partite and connected structure in the cor-		
253	relation based networks beyond the structure captured by a sparse weighted		
254	configuration null network model (see section 3.5.5), shown for different time		
255	bin widths. Note that the k -partite structure disappears for time bin width		
256	greater than 200ms for all three subjects. The dimension of the connected		
257	structure reduces with increasing bin width for 2 of the 3 subjects (top row).	43	
258 3.7	(A-B) Correlation matrices with detected communities indicated by white		
259	lines. Each off main diagonal entry in the matrix represents a pair of neu-		
260	rons. Those entries within a white square indicate that both of those neurons		
261	are in the same community as detected by our community detection proce-		
262	dure. Matrices shown are for 5ms and 1s time bin widths respectively. Main		
263	diagonal entries were set to 0. (C-D) Matrices showing the anatomical dis-		
264	tribution of pairs along with their community membership. Entries where		
265	both cells are in the same region are given a colour indicated by the colour		
266	bar. Entries where cells are in different regions are given the grey colour also		
267	indicated by the colour bar.	44	
268 3.8	(A) The variation of information is a measure of distance between cluster-		
269	ings. The distance between the anatomical ‘clustering’ and community de-		
270	detection ‘clustering’ increases with increasing time bin width. (B) The ad-		
271	justed Rand index is a normalised similarity measure between clusterings.		
272	The anatomical and community detection clusterings become less similar as		
273	the time bin width increases.	45	
274 3.9	Comparing the components of the total covariance across different values for		
275	the time bin width. We observed a consistent increase in $E[\text{cov}(X, Y Z)]$ as		
276	the time bin width increased. But we saw different trends for $\text{cov}(E[X Z], E[Y Z])$		
277	for each mouse.	46	
278 3.10	Comparing the components of the total covariance across different values for		
279	the time bin width. We saw a consistent increase in $\rho_{X,Y Z}$ as the time bin		
280	width increased in all three subjects. But we saw different trends in ρ_{signal} for		
281	each of the subjects.	47	

282	3.11 Matrices showing the regional membership of pairs by colour, and the com-	
283	munities in which those pairs lie. (A-B) Detected communities and regional	
284	membership matrix for network based on rectified spike count correlation	
285	$\rho_{X,Y Z}$, using time bin widths of 0.005s and 1s respectively. (C-D) Detected	
286	communities and regional membership matrix for network based on rectified	
287	signal correlation ρ_{signal} , using time bin widths of 0.005s and 1s respectively.	48
288	3.12 Distance and similarity measures between the anatomical division of the neu-	
289	rons, and the communities detected in the network based on the spike count	
290	correlations $\rho_{X,Y Z}$. (A) The variation of information is a ‘distance’ mea-	
291	sure between clusterings. The distance between the anatomical ‘clustering’	
292	and the community clustering increases as the time bin width increases. (B)	
293	The adjusted Rand index is a similarity measure between clusterings. The	
294	detected communities become less similar to the anatomical division of the	
295	cells as the time bin width increases.	49
296	3.13 Distance and similarity measures between the anatomical division of the neu-	
297	rons, and the communities detected in the network based on the signal cor-	
298	relations ρ_{signal} . (A) The variation of information is a ‘distance’ measure be-	
299	tween clusterings. The distance between the anatomical ‘clustering’ and the	
300	community clustering increases as the time bin width increases. (B) The ad-	
301	justed Rand index is a similarity measure between clusterings. The detected	
302	communities become less similar to the anatomical division of the cells as	
303	the time bin width increases.	50
304	3.14 (A-B) Absolute correlation matrices with detected communities indicated by	
305	white lines. These communities are based on the absolute value of the total	
306	correlation between each pair of cells. Those entries within a white square in-	
307	dicate that both of those neurons are in the same community. Matrices shown	
308	are for 5ms and 1s time bin widths respectively. Main diagonal entries were	
309	set to 0. (C-D) Matrices showing the anatomical distribution of pairs along	
310	with their community membership. Regional membership is indicated by the	
311	colour bar. (E) Variation of information between the anatomical division of	
312	the cells, and the detected communities. (F) Adjusted Rand index between	
313	the anatomical division, and the detected communities.	51

314	3.15 (A-B) Sign reversed rectified correlation matrices with detected communities indicated by white lines. Those entries within a white square indicate that both of those neurons are in the same community. Matrices shown are for 5ms and 1s time bin widths respectively. Main diagonal entries were set to 0. (C-D) Matrices showing the anatomical distribution of pairs along with their community membership. Regional membership is indicated by the colour bar. (E) Variation of information between the anatomical division of the cells, and the detected communities. (F) Adjusted Rand index between the anatomical division, and the detected communities.	52
323	3.16 Probe Locations: The locations of the probes in each of the three mouse brains (Stringer et al., 2019).	57
325	3.17 Entropy Limit: The upper limit on entropy of binned spike count data as a function of the maximum observed spike count. The orange line is the analytical maximum. The blue line is the entropy of samples with $N = 1000$ data points taken from the discrete uniform distribution.	63
329	4.1 Figures showing the over-dispersion possible for a beta-binomial distribution relative to a binomial distribution. Parameters are shown in the captions.	80
331	4.2 Figures showing (A) the under-dispersion and (B) over-dispersion permitted by the COMb distribution relative to a binomial distribution. (C) illustrates that the p parameter of the COMb distribution does not correspond to the mean of the distribution, as it does for the binomial and beta-binomial distributions. (D) shows a heatmap for the value of the Kullback-Liebler divergence between the COMb distribution and the standard binomial distribution with same value for n , as a function of p and ν . Parameters are shown in the captions.	83

339	4.3 (A) Raster plot showing the spikes fired by 33 randomly chosen neurons in 340 the primary visual cortex. (B-C) (B) average and (C) variance of the number 341 of active neurons, measured using a sliding window 100ms wide, split into 342 100 bins. The midpoint of the time interval for each window is used as the 343 timepoint (x-axis point) for the measurements using that window. The grey 344 shaded area indicates the presence of a visual stimulus. The opaque line is 345 an average across the 160 trials that included a visual stimulus of any kind. 346 We can see a transient increase in the average number of active neurons and 347 the variance of this number, followed by a fluctuation and another increase.	86
348	4.4 (A) Raster plot showing the spikes fired by 33 randomly chosen neurons in 349 the hippocampus. (B-C) (B) average and (C) variance of the number of active 350 neurons, measured using a sliding window 100ms wide, split into 100 bins. 351 The midpoint of the time interval for each window is used as the timepoint (x- 352 axis point) for the measurements using that window. The grey shaded area 353 indicates the presence of a visual stimulus. The opaque line is an average 354 across the 160 trials that included a visual stimulus of any kind. We can see 355 a transient increase in the average number of active neurons and the variance 356 of this number at stimulus onset.	87
357	4.5 (A) Raster plot showing the spikes fired by 33 randomly chosen neurons in 358 the thalamus. (B-C) (B) average and (C) variance of the number of active 359 neurons, measured using a sliding window 100ms wide, split into 100 bins. 360 The midpoint of the time interval for each window is used as the timepoint (x- 361 axis point) for the measurements using that window. The grey shaded area 362 indicates the presence of a visual stimulus. The opaque line is an average 363 across the 160 trials that included a visual stimulus of any kind. We can 364 see in immediate increase at stimulus onset, a subsequent fall, and another 365 sustained increased until the stimulus presentation ends.	88

366	4.6 (A) An example of the binomial, beta-binomial, and Conway-Maxwell-binomial	
367	distributions fitted to a sample of neural activity. The Conway-Maxwell-	
368	binomial distribution is the best fit in this case. The histogram shows the	
369	empirical distribution of the sample. The probability mass function of each	
370	distribution is indicated by a different coloured line. (B) Across all samples	
371	in all trials, the proportion of samples for which each fitted distribution was	
372	the best fit. The Conway-Maxwell-binomial distribution was the best fit	
373	for 93% of the samples taken from V1 using a bin width of 1ms.	89
374	4.7 (A) We fit a Conway-Maxwell-binomial distribution to the number of active	
375	neurons in 1ms time bins of a 100ms sliding window. We did this for all	
376	trials with a visual stimulus and took the average across those trials. We	
377	see a transient drop in value for the distribution's ν parameter at stimulus	
378	onset. This shows an increase in association between the neurons. (B) We	
379	measured the correlation coefficient between the spike counts of all possible	
380	pairs of neurons in the same sliding window. The took the average of those	
381	coefficients. We also did this for every visually stimulated trial, and took	
382	the average across trials. The increase in association is not reflected with an	
383	increase in average correlation.	91
384	4.8 (A) The mean Fano factor of the spike counts of the cells in the primary visual	
385	cortex. Means were taken across cells first, then across trials. There was a	
386	significant decrease in the Fano factors immediately after stimulus onset. (B)	
387	The mean Fano factor of the spike counts of the cells in the motor cortex. No	
388	significant change in measurements at any point.	92

389 List of Tables

390 2.1	Fixed parameters A table of the parameters fixed before optimising the	
391	model. The values of these parameters could be changed to model differ-	
392	ent fluorescent calcium indicators.	28
393 4.1	Details of the different bin width and analysis window sizes used when bin-	
394	ning spike times, and analysing those data.	77
395 4.2	Relative dispersion of the COMb distribution, and association between Bernoulli	
396	variables as represented by the value of the ν parameter.	82
397 4.3	Proportion of samples for which each distribution was the best fit, grouped	
398	by bin width. The COMb distribution is the best fit most of the time.	90

For/Dedicated to/To my...

400 **Chapter 1**

401 **Introduction**

402 **1.1 Overview**

403 Ideas (not in order):

- 404 • From small to big datasets (in terms of number of neurons)
- 405 • Big datasets mean statistical methods are more necessary (curse of dimensionality)
- 406 • Big datasets mean higher order correlations are more meaningful (schneidman)
- 407 • Exploit pairwise correlations in different way (eight probe)
- 408 • abandon correlations embrace association (COMB)
- 409 • electrophysiology drawbacks vs calcium benefits
- 410 • calcium drawbacks (fluorescence modelling) (mention nuclear filling and cell pathology) (mention that calcium imaging can only be used near the surface of the brain, e-phys can go deeper, especially with new probes)

413 Since Hodgkin and Huxley's squid experiments featuring a single axon (Hodgkin and
 414 Huxley, 1939), to more recent research with spike sorted data from ~ 24000 neurons from
 415 34 brain regions from 21 mice (Allen et al., 2019), the number of neurons contributing to
 416 electrophysiological datasets has been growing. Recording methods using two-photon cal-
 417 cium imaging have also been used to extract data from populations containing over 10000
 418 neurons (Peron et al., 2015). This dramatic growth in the number of neurons to analyse
 419 required a dramatic change in analysis methods.

420 To focus on calcium imaging for a start, a neuron that contains a fluorescent calcium
 421 indicator in its cytoplasm will fluoresce when bombarded with photons. The amount that the
 422 cell will fluoresce is dependent on the concentration of fluorescent indicator within the cell,

and the concentration of calcium within the cell. When a neuron fires an action potential, the influx of free calcium ions causes an increase in fluorescence when those ions bond with the fluorescent indicator and those bounded molecules are bombarded with photons. After the action potential, as calcium is extruded from the cell the fluorescence returns to a baseline level. This is the basic mechanism of fluorescent calcium indicator based imaging.

This method has some advantages over electrophysiology as measure of neuronal ensemble activity. Isolating individual neurons is easier and more reliable than identifying unique spike sources in electrophysiology. Also, spike sorting methods can only detect spikes, but imaging methods can also detect cells that are not spiking. Cells will emit a baseline level of fluorescence when not firing action potentials. Calcium imaging sites can be re-used for weeks for longitudinal studies (Chen et al., 2013). Because the fluorescent indicator is delivered to the cell by adeno-associated viruses, there can be problems with indicator gradients around the infection site, and expression levels will change in individual cells over weeks (Tian et al., 2009; Chen et al., 2013). This delivery method can also cause cell pathology, and nuclear filling (Zariwala et al., 2012), but these problems can be solved by using lines of transgenic mice (Dana et al., 2014).

If the imaging data is collected at a high enough frequency, and the signal-to-noise ratio of the fluorescence trace is high enough, it should be possible to infer the spike times to some level of accuracy. For example, the calmodulin based indicator GCaMP6s has a sufficiently high signal-to-noise ratio that isolated action potentials can be detected and inferred (Chen et al., 2013). Many spike inference algorithms exist (Vogelstein et al., 2010; Pnevmatikakis et al., 2016; Friedrich and Paninski, 2016; Pnevmatikakis et al., 2013; Pnevmatikakis et al., 2014; Deneux et al., 2016; Greenberg et al., 2018), and some of these can perform both cell isolation and spike detection simultaneously (Vogelstein et al., 2010; Pnevmatikakis et al., 2016; Pnevmatikakis et al., 2014; Deneux et al., 2016). But the relationship between spiking and fluorescence change is not fully understood. For example, the fluorescent indicator will act like an additional calcium buffer within the cell cytoplasm and will compete with the other endogenous buffers to bind with free calcium cells. Therefore, the concentration of those endogenous buffers, and the binding dynamics of those buffers will have an effect on the change in fluorescence in response to an action potential. Furthermore, the binding dynamics of the fluorescent indicator itself will have an effect on the change in fluorescence. For example, the GCaMP series of fluorescence indicators are based on the calcium buffer protein calmodulin. This protein has four binding sites, whose affinities interact non-linearly. But most of the spike inference algorithms model the fluorescence as a linear function of a

457 calcium trace, and they model this calcium trace as a first or second order autoregression with
458 a pulse input to represent action potentials. Deneux et al. (2016) developed a spike inference
459 algorithm with a bit more biological inspiration, but this amounted to a very similar process.
460 While this autoregression idea appears to be a reasonable approximation, the algorithms that
461 use this approximation are outperformed by the most recently published spike inference al-
462 gorithm to be cited here ((Greenberg et al., 2018)). This algorithm does take into account the
463 binding dynamics of both the endogenous buffers and fluorescent calcium indicator, and the
464 concentrations of free calcium, indicator, and endogenous buffer within the cell cytoplasm.
465 This shows that there is value in more biologically inspired models of fluorescent calcium
466 indicators.

467 In light of the growing popularity of two-photon calcium imaging, and the lack of biolog-
468 ically inspired spike inference algorithms (Greenberg et al. developed their spike inference
469 algorithm in parallel to our work), we decided to develop a biologically inspired model for
470 fluorescent calcium indicator fluorescence. The idea being that our model would take a spike
471 train, or simply spike times, provided by the user, and return the fluorescence trace that would
472 be induced by this spike train or spike times. The model contains parameters for concentra-
473 tions of indicator and endogenous buffers, as well as affinity and unbinding rates for these
474 buffers. There are also parameters for the baseline concentration of free calcium in the cell
475 cytoplasm, and the cell radius (as a means for calculating the cell volume). With this model,
476 we hoped that experimentalists would be able to test out different calcium indicators on the
477 types of spike trains that they expect to encounter. This way they could decide ahead of time
478 which indicator suited them their situation best. Since the output of our model is a fluo-
479 rescence trace, the spike inference models mentioned above can be applied to the modelled
480 fluorescence. This means that the model could also be used to benchmark the performance
481 of these spike inference algorithms, and to investigate the impact of variations in the model
482 on spike inference accuracy.

483 We have outlined some of the advantages that calcium imaging has over electrophysi-
484 ogy. But electrophysiology is more useful in some situations. One particular drawback for
485 two-photon calcium imaging is that it can only be used for imaging near to the surface of the
486 brain. Although imaging with three (or presumably more) photons may solve this problem
487 in the future (Ouzounov et al., 2017). A better option for reading activity from neurons be-
488 yond the surface of the brain is to use Neuropixels probes (Jun et al., 2017). These probes
489 can be used to read from thousands of neurons simultaneously in many different areas of the

490 brain (Allen et al., 2019; Stringer et al., 2019; Steinmetz, Carandini, and Harris, 2019; Stein-
491 metz et al., 2019). This brings us to another problem for which we require new innovations
492 in our analysis methods. Specifically, analysing correlated behaviour in neural ensembles
493 consisting of neurons from many different brain regions.

494 Until the invention of new technologies such as the Neuropixels probes, most elec-
495 trophysiology datasets read from neurons in only one or two regions. Therefore most of
496 the research on interactions between neurons in different regions is limited to two regions
497 (Wierzynski et al., "2009"; Patterson et al., 2014; Girard, Hupé, and Bullier, 2001). In chap-
498 ters 3 and 4 we used datasets with neurons from 9 and 5 different brain regions respectively.

499 In light of recent findings based on correlated behaviour showing that spontaneous be-
500 haviours explain activity in many different parts of the brain that would otherwise be regarded
501 as noise (Stringer et al., 2019), that satiety is represented brain wide Allen et al., 2019, and
502 that exploratory and non-exploratory states are represented in the amygdala Gründemann
503 et al., 2019, it was clear that state representation or motor control had an influence on cor-
504 related behaviour in areas of the brain not usually associated with these tasks. Also, given
505 differences in timescales of fluctuations in different brain regions Murray et al., 2014, and
506 different timescales for event representation in different brain regions Baldassano et al., 2017,
507 we decided to investigate brain wide correlated behaviour at timescales ranging from 5ms up
508 to 3s.

509 We started off measuring the correlations in spike counts between individual neurons in
510 our ensemble. These measurements induced a weighted undirected graph where each node
511 represented a neuron, and the weight of each edge was the strength of the correlation be-
512 tween the neurons represented by the nodes at either end of that edge. In order to put the
513 neurons into groups with correlated behaviour, we applied a novel community detection al-
514 gorithm (Humphries et al., 2019) to this graph. We repeated this analysis for timescales from
515 milliseconds to seconds. Bear in mind that our correlation based graph was completely ag-
516 nistic of the anatomical regions in which our cells resided. We then compared our correlated
517 communities to their anatomy at each timescale. In this way, we used a novel method, never
518 applied neuronal data before, to analyse the makeup of correlated communities across dif-
519 ferent regions at different timescales. We found that for short timescales $< 50\text{ms}$ correlated
520 communities tended to exist within anatomical regions, and for longer timescales $> 100\text{ms}$,
521 the correlated communities tended to exist across anatomical regions. This is broadly in agree-
522 ment with a similar finding for EEG data from humans performing semantic or memory tasks
523 (Stein and Sarnthein, 2000).

524 Many important findings have been made by measuring the correlations between binned
525 spike counts, but there are some problems with this method of analysis. Firstly, the width
526 of the bins used to bin spike times into spike counts has an effect on the magnitude of the
527 correlations measured. Using a short bin width can cause your measurements to be artificially
528 small (Cohen and Kohn, 2011). This may not be an issue if one is considering relative size of
529 correlations when using the same bin width, but it is still not ideal. Secondly, while pairwise
530 correlations can capture most of the information in a small network (up to 40 cells) of highly
531 correlated cells (Schneidman et al., 2006), a model based on pairwise correlations alone will
532 fail to capture the activity of larger (~ 100 cells) networks, higher order correlated activity
533 is required (Ganmor, Segev, and Schneidman, 2011). The problem with these higher order
534 correlations is that they may be defined in different ways (Staude, Grün, and Rotter, 2010),
535 and if we want to include them in a model, this usually involves greatly increasing the number
536 of parameters to fit, leading to the ‘curse of dimensionality’.

537 bin width affects the magnitude of correlations (cohen 2) problem with correlations is
538 that pairwise correlations may not be sufficient for large populations (schneidman) need to
539 capture high order correlations hard to define some attempts at capturing interaction between
540 individual cells and whole population (o donnell, okun) for short bin widths reject correlation,
541 embrace association

542 **Chapter 2**

543 **Sensitivity of the**
544 **spikes-to-fluorescence transform to**
545 **calcium indicator and neuron**
546 **properties**

547 *Abstract*

548 Fluorescent calcium indicators such as GCaMP are widely used to monitor neuronal activity.
549 However the relationship between the fluorescence signal and the underlying action potential
550 firing is poorly understood. This lack of knowledge makes it difficult for experimenters
551 to decide between different indicator variants for a given application. We addressed this
552 problem by studying a basic biophysical model of calcium dynamics in neuronal soma. We
553 fit the model parameters to publicly available data where GCaMP6s fluorescence and whole-
554 cell electrophysiological recordings were made simultaneously in the same single neurons.
555 We systematically varied the model's parameters to characterise the sensitivity of spike train
556 inference algorithms to the calcium indicator's main biophysical properties: binding rate,
557 dissociation rate, and molecular concentration. This model should have two potential uses:
558 experimental researchers may use it to help them select the optimal indicator for their desired
559 experiment; and computational researchers may use it to generate simulated data to aid design
560 of spike inference algorithms.

561

2.1 Introduction

562 Although fluorescent calcium indicators such as GCaMP are widely used to monitor neuronal
563 activity, the relationship between the fluorescence signal and the underlying action potential
564 firing is imperfect. The fluorescence signal has a low signal-to-noise ratio, and most indi-
565 cators' kinetics are slow relative to the millisecond-timescale dynamics of the membrane
566 voltage (example in Figure 1). This makes spike inference difficult. Furthermore, the effects
567 of the indicator and cell properties on the fluorescence signal are unknown. For example,
568 genetically encoded indicators can accumulate within neurons over weeks and months (Chen
569 et al., 2013). Studies using calcium-sensitive fluorescent dyes have shown that indicator con-
570 centration has substantial effects on the spike-to-fluorescence relationship (Maravall et al.,
571 2000). Therefore spike rates inferred from GCaMP fluorescence signals may give mislead-
572 ing results if comparing across imaging sessions. More generally, the poor understanding of
573 the spike-to-fluorescence transform means experimenters may not know whether to trust the
574 outputs of spike train inference methods in any given application.

575 Spike trains are usually inferred from the time series of intensity values of one pixel of the
576 fluorescence image, where the pixel is located at the cell's soma. The problems of identifying
577 these pixels, and inferring spikes from their time series can solved separately or together.
578 When attempting to infer spikes, the fluorescence trace is modelled as a linear combination of
579 calcium concentration dynamics, a baseline calcium concentration, and some Gaussian noise.
580 The calcium concentration dynamics are modelled as an autoregressive process of degree 1
581 or 2 with a pulse input corresponding to the spike train, or the number of spikes fired in a
582 time step. The model includes no dynamics for the fluorescent indicator itself. Furthermore,
583 in order to make this model into an easily solvable linear programming problem the number
584 of spikes fired in a timestep is not restricted to non-negative integers but to arbitrary non-
585 negative values (Vogelstein et al., 2010; Pnevmatikakis et al., 2016; Friedrich and Paninski,
586 2016; Pnevmatikakis et al., 2013; Pnevmatikakis et al., 2014). More biologically inspired
587 spike inference models do exist (Deneux et al., 2016), but their fundamentals are very similar.
588 In this work, we investigated the effect of changing dynamics and buffer concentrations on
589 the accuracy of the inference algorithms based on these models.

590 The aim of this project was to model the fluorescence traces produced by a fluorescent
591 calcium indicator in a neuron soma resulting from a specific spike train, given calcium indi-
592 cator parameters such as binding rate, dissociation rate, and molecular concentration. Such

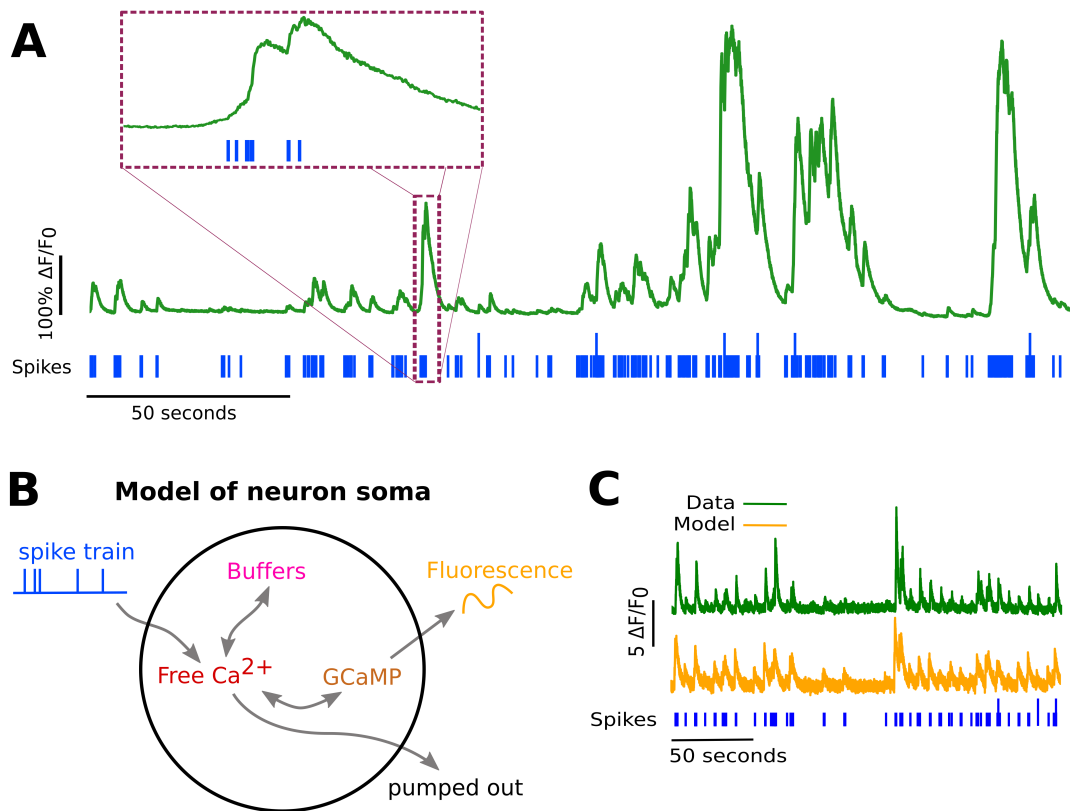


FIGURE 2.1:

A: Example spike train (blue) and the corresponding GCaMP6s fluorescence trace (green), data replotted from (Berens et al., 2018). Inset shows zoomed section of traces to highlight slow decay of GCaMP6s fluorescence relative to spike time intervals.

B: Schematic diagram of the neuron calcium and GCaMP computational model.

C: Good visual match of data fluorescence trace (green) and model simulated fluorescence (orange) in response to an identical spike train (blue).

593 a model would allow benchmarking of various spike inference algorithms, and enable under-
594 standing of how indicator characteristics affect the quality of spike train inference.

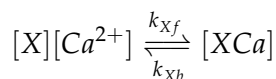
595 The model we developed consisted of free calcium, fluorescent indicator molecules, and
596 mobile and immobile endogenous calcium buffers. The indicator molecules which were
597 bound to a calcium molecule could be either excited, i.e. able to release a photon, or relaxed.
598 In order to reproduce the noise inherent in the data collection, we modelled the release of
599 photons from the excited indicator bound calcium as a stochastic process.

600 The fluorescence traces produced by the simulation were calibrated to reproduce the
601 signal-to-noise ratio observed in experimental data. Previously published spike inference
602 algorithms were then used to infer spike trains from the experimental fluorescence traces and
603 the modelled fluorescence traces. The parameters of the model were then varied in order to
604 determine the effect on the system dynamics and the effects on spike inference.

605 2.2 Results

606 2.2.1 A biophysical computational model can generate accurate fluorescence 607 traces from spike trains

To study the relationship between action potential firing and calcium fluorescence, we built a computational model of calcium dynamics in a neuronal soma. The model consisted of four dynamic variables: the concentration of free calcium, two types of endogenous buffer, and the calcium-sensitive fluorescent indicator. Each of the buffers and the indicator could independently bind and unbind with calcium. These reactions were modelled as



608 where X is the buffer concentration and Ca^{2+} is the calcium concentration. Each species
609 could therefore exist in two states: either bound with calcium or unbound. To model the
610 imaging process, we also added a third, excited state to the indicator. When in the calcium-
611 bound state, the indicator could be converted to an excited state, corresponding to the absorp-
612 tion of a photon. The rate of this excitation process could be interpreted as the intensity of
613 the light illuminating the sample. Once excited, the species decayed back to the unexcited
614 state at a fixed rate, corresponding to the spontaneous emission of photons. The total emitted
615 fluorescence signal was interpreted as proportional to this de-excitation flux. To represent
616 experimental noise in the photon capture process, we drew a random number of captured

617 photons at each time step from a binomial distribution, parameterised by a number p that
618 corresponds to the mean fraction of released photons that are captured.

619 The model had 17 parameters in total describing the molecules' concentrations and re-
620 action rates (Methods). We set 13 of these parameters to values from the literature. The
621 remaining 4 parameter values we fit to publicly-available data (Berens et al., 2018), briefly
622 explained as follows (see Methods for full details). Single neurons from acute rat cortical
623 slices expressing GCaMP6f were imaged with two-photon microscopy while the membrane
624 potentials of the somata of the same neurons were simultaneously recorded via whole-cell
625 patch clamp electrophysiology. In this dataset, the electrical recordings give unambiguous
626 information about neurons' spike times. To do the parameter fitting, we feed these spike
627 trains as inputs to the computational model. After running, the model returns a simulated
628 fluorescence trace. We aimed to find the model parameter values that give the best match
629 between this simulated fluorescence trace and the real fluorescence time series recorded in
630 the corresponding neuron. To do this we used a suite of optimisation procedures to jointly
631 fit both the real neuron's fluorescence time series and power spectrum, which capture com-
632 plementary information about the spikes-to-fluorescence mapping (Methods). We performed
633 the fitting procedure independently for each of the 20 neurons in the spikefinder dataset
634 (<http://spikefinder.org>). After fitting, the model produced realistic-looking fluorescence time
635 series (Figure 2.1).

636 **2.2.2 Spike inference algorithms perform similarly on real data compared with**
637 **time series simulated from the model**

638 Researchers often pass the fluorescence time series through a spike inference tool before per-
639 forming further statistical analyses. These spike inference algorithms take the fluorescence
640 trace as input and attempt to estimate the neuronal spike train that triggered them (Vogelstein
641 et al., 2010; Pnevmatikakis et al., 2016; Friedrich and Paninski, 2016; Pnevmatikakis et al.,
642 2013; Pnevmatikakis et al., 2014; Deneux et al., 2016). Part of our motivation for building
643 this model was to allow us to ask the question: how do the properties of the cell and the
644 calcium indicator affect the quality of spike inference? In order to trust the conclusions from
645 our model, we should first be confident that spike inference from our simulated fluorescence
646 traces is similar to that from the real data. To test this we passed each of the simulated fluores-
647 cence traces through three previously published spike inference algorithms, quantified their
648 performance against the ground-truth electrophysiology data, repeated the procedure for the
649 real calcium fluorescence time series, and compared the accuracy of the inference processes

in all cases. The *true positive rate*, also known as the *recall*, the *sensitivity*, or the *probability of detection* of spike inference varied across the three inference algorithms we tried (p value and statistical test here). The constrained non-negative matrix deconvolution algorithm (Pnevmatikakis et al., 2016) (CNMD algorithm) correctly detected approximately 45% of the true spikes, the OASIS algorithm (Friedrich and Paninski, 2016) correctly detected approximately 35% of the true spikes, and the ML spike algorithm (Deneux et al., 2016) correctly detected approximately 15% of the true spikes (see figure 2.2). Notably, for two of the three inference algorithms, the quality of inference was also fairly consistent for individual spike trains, not just the group means ($p > 0.05$, paired t-test). This demonstrates that the models were generating fluorescence time series that were similarly difficult to decode as the real data, in ways that were not specific to any one inference algorithm. This is evidence that the models captured real aspects of the spikes-to-fluorescence transform.

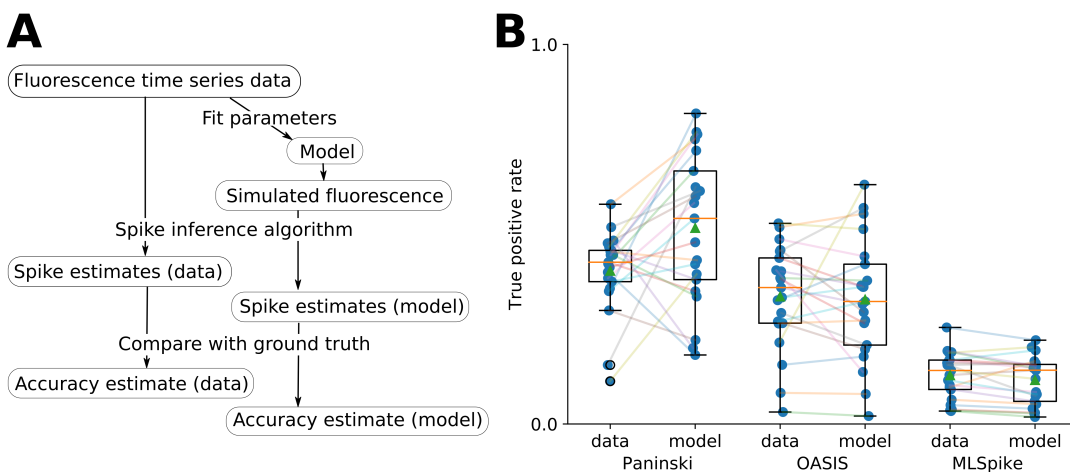


FIGURE 2.2:
A: Workflow to compare spike inference for real versus simulated fluorescence data.
B: True positive rates achieved by three different spike inference algorithms when applied to observed spike trains, and simulated spike trains. Data points overlaid as blue circles. The performance is similar from real and simulated data for each of the algorithms.

661

662 2.2.3 Relative effects of various buffers to the fluorescence signal

One of the benefits of computational models over laboratory experiments is that we can observe all the variables in the simulation to gain insight into the system's dynamics, which can be difficult to do in the lab. We plotted the concentrations of the various species over time for a version of the model fit to one data set, in response to the same train of spikes used for fitting (figure 2.3). Figure 2.3a shows the absolute values of the species concentrations,

668 summed. Consistent with experimental estimates (Maravall et al., 2000), only a small fraction
669 ($\sim 0.1\%$) of calcium is free and unbound to any buffer. Of the bound calcium, the vast
670 majority, ($\sim 96\%$) is bound to the GCaMP indicator. The two types of endogenous buffer
671 are bound to the remaining calcium ($\sim 4\%$). An influx of calcium from a single spike adds
672 very little to the total calcium, in relative terms (red line in Figure 3a).

673 When calcium entered the model neuron it was rapidly buffered (Bartol et al., 2015).
674 However the relative fractions of which buffer molecules bound to the influxed calcium was
675 dynamic, and changed over time . Figure 2.3 (b-f) shows the time course of the various
676 species over time in response to a calcium influx event from a single action potential. Cru-
677 cially, the indicator $[BCa]$ competed with the endogenous buffers $[ImCa]$ and $[ECa]$ – all
678 three bind calcium on similar timescales. This implies that the timecourse and amplitude of
679 the $[BCa]$ variable will also depend on the binding rates and availabilities of the endogenous
680 buffers. For example if we decreased the concentration of an endogenous buffer, we might
681 expect both a faster rise time and greater peak amplitude of the $[BCa]$ signal in response to
682 a calcium influx event. The slowest component of the decay had a similar time constant for
683 $[BCa]$, $[ImCa]$ and $[ECa]$, which in turn matched the $[Ca]$ extrusion time constant in our
684 model ($\sim 6.29 \times 10^{-22} \text{Ms}^{-1}$). This implies that the buffers and the indicator had reached
685 a dynamic equilibrium and were jointly tracking the free calcium concentration as calcium
686 was slowly extruded from the cell.

687 Interestingly the excited bound calcium species ($[BCa^*]$) showed a qualitatively different
688 timecourse in response to a calcium influx event. This concentration is subject to the added
689 ‘excitation and release’ dynamic, where a certain proportion of the concentration absorbs the
690 energy from an incoming photon and goes into an ‘excited state’ at each time step. A certain
691 proportion of the concentration releases a photon and reverts to a ‘relaxed state’ at each
692 timestep also. This means that the excited bound calcium lags behind the bound calcium
693 trace. We could think of the excited bound calcium trace as a low pass filtered version of the
694 bound calcium trace.

695 **2.2.4 Spike inference accuracy is sensitive to indicator properties, and likely
696 varies within and between cells**

697 The above results imply that the fluorescence signal depends on the relative properties of
698 both GCaMP and the endogenous buffers. We next used the model to directly ask how
699 sensitive spike inference was to these components. We focused on three key parameters that

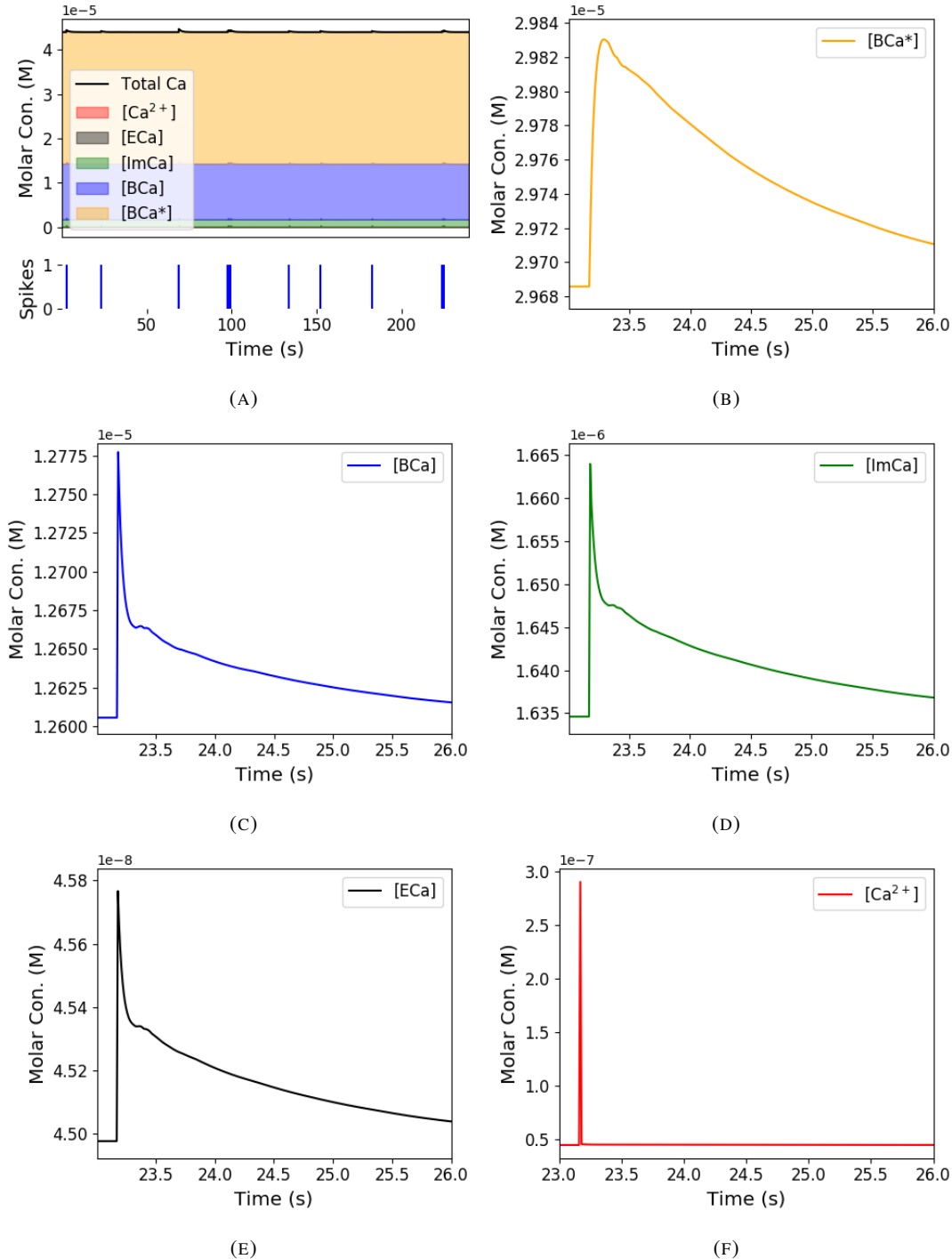


FIGURE 2.3: **Calcium Buffering Dynamics** (a) The proportions of bound and free calcium concentrations within a cell, with the associated spike train. (b)-(f) The dynamics of the concentration of (b) excited indicator bound calcium, (c) indicator bound calcium, (d) immobile endogenous buffer bound calcium, (e) mobile endogenous buffer bound calcium, and (f) free calcium in response to an action potential at $\sim 23.2s$.

700 likely vary from cell to cell and experiment to experiment: GCaMP binding kinetics, GCaMP
701 concentration, and endogenous buffer concentration.

702 Several variants of GCaMP itself have been made that differ in calcium binding kinetics,
703 baseline fluorescence, fluorescence efficiency, and other factors. For example, GCaMP6f has
704 a decay time constant of ~ 1 s, while GCaMP6s has a decay time constant of ~ 2 s (Chen
705 et al., 2013). Here we asked how these differences in binding kinetics affect spike inference.
706 We jointly varied the calcium binding and unbinding rates of the indicator by the same factor
707 over a range from 100-fold slower to 100-fold faster from the fitted values, and simulated the
708 fluorescence response for each of the parameter settings in response to the same spike trains
709 as before (figure 2.4). Notably this manipulation does not affect the indicators affinity, and
710 therefore would not affect steady-state responses to prolonged changes in calcium. Instead
711 it is likely to affect its sensitivity to the spike train dynamics. We computed two summary
712 measures from the simulated fluorescence traces: the signal-to-noise ratio for a single spike
713 (Methods, section 2.4.6), and the accuracy of spike inference for each of the spike trains. We
714 observed a reduction in the signal-to-noise ratio and the spike inference quality when we set
715 the binding and unbinding rates were set to one hundredth of their fitted values, and to one
716 tenth of their fitted values. When we increased the value of both binding rates, we observed
717 no change in these measurements. The reduction in both rates lead to smaller increases in
718 fluorescence in response to an action potential and a longer decay time (figure 2.4a), this
719 caused the reduction in signal-to-noise ratio. As both rates were increased, the change in
720 $\Delta F/F_0$ in response to an action potential increased and the decay time decreased slightly,
721 but the fluorescence trace created by these values was very similar to the trace created by the
722 fitted values.

723 Second, the overall concentrations of GCaMP often varies from cell to cell. For exam-
724 ple different cells, even of the same type in the same tissue, can express different levels of
725 GCaMP, due to proximity to the infection site, or the cell becoming ‘nuclear-filled’ (Tian et
726 al., 2009; Chen et al., 2013). Also, GCaMP is often used for longitudinal experiments where
727 the same cells are re-imaged across multiple days or weeks. However since GCaMP expres-
728 sion typically ramps up over time (Chen et al., 2013), the accuracy of spike inference may
729 differ across multiple longitudinal recordings in the same cell. We addressed this by varying
730 the concentration of calcium indicator in the model, simulating spike trains and measuring
731 signal-to-noise ratio and spike inference accuracy on the resulting fluorescence traces. Both
732 increasing and decreasing the concentration of the indicator had effects on the fluorescence

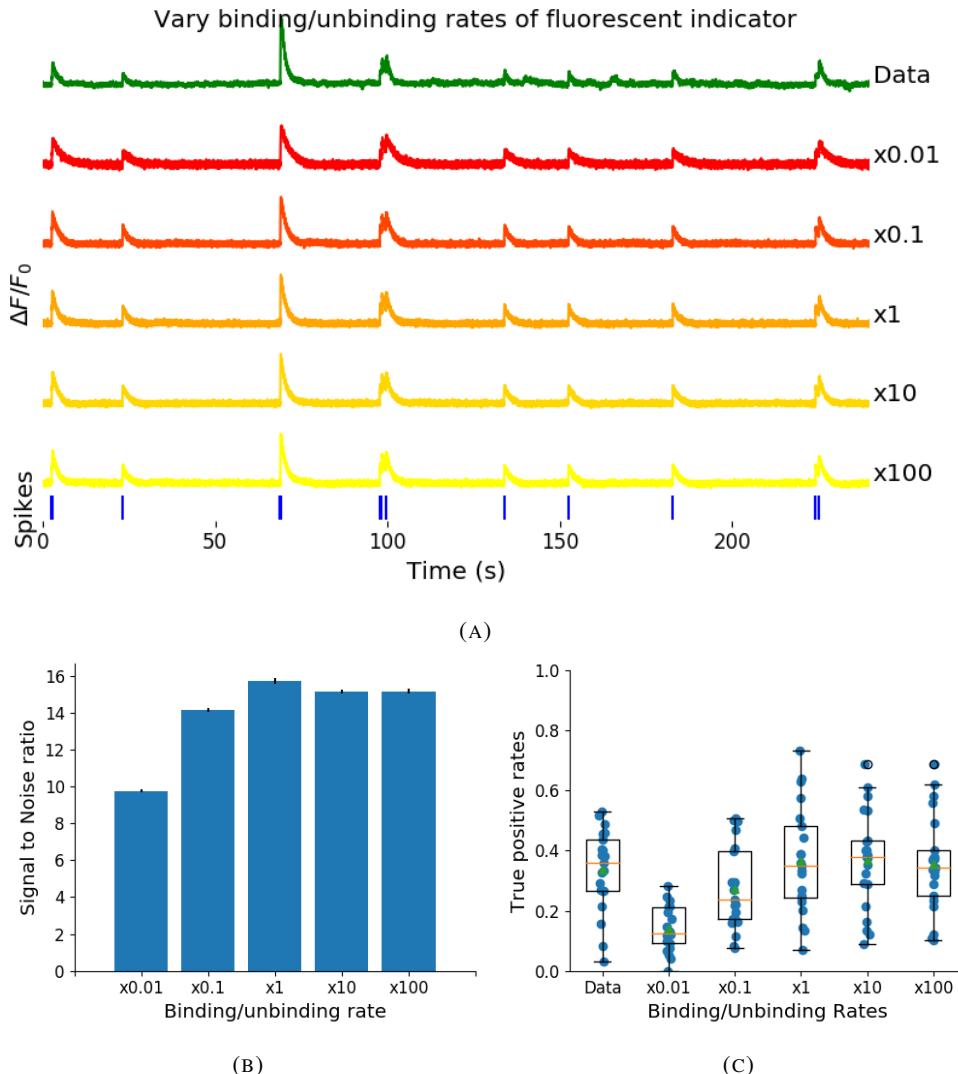


FIGURE 2.4: (a) An example trace for each of the five pairs of values used for the binding and unbinding rates of the fluorescent calcium indicator. (b) The signal-to-noise ratio of the modelled fluorescence traces using each of the four perturbed values, and the experimental value. The SNRs for the two pairs with values lower than the experimental value are lower than the experimental pair or the higher value pairs. (c) The true-positive rates of the deconvolution algorithm's predictions when inferring from the observed data, and inferring from modelled traces using the perturbed and experimental values.

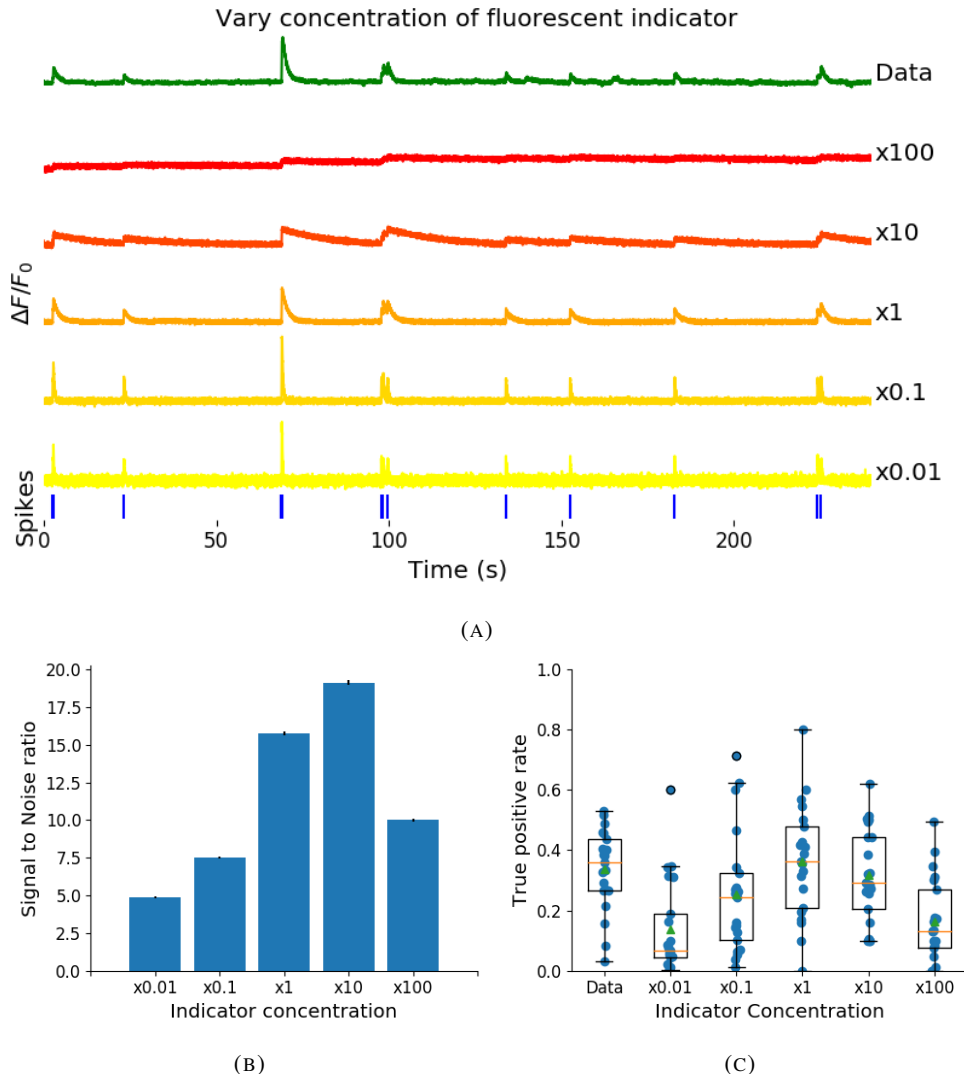


FIGURE 2.5: (a) An example trace for each of the five perturbed values for the concentration of fluorescent calcium indicator. The top two traces are produced by the lower perturbed values, the middle trace is produced by the experimental value, and the lowest two traces are produced when using the higher perturbed values. (b) The signal-to-noise ratio of the modelled fluorescence traces using each of the four perturbed values, and the experimental value. Extreme perturbations of the concentration either above or below the experimental level lowered the SNR. (c) The true-positive rates of the deconvolution algorithm's predictions when inferring from the observed data, and inferring from modelled traces using the perturbed and experimental values. We found that the algorithms performs equally badly on the two most extreme values, and performs equally well on the experimental value, and the next higher perturbed value.

733 trace, signal-to-noise ratio, and spike inference. The signal-to-noise ratio and spike inference
734 quality decreased with decreased indicator concentration, and both showed a decrease
735 when the indicator concentration was increased to 100 times its fitted value (figure 2.5).
736 The signal-to-noise ratio showed an increase when the indicator concentration was increased
737 to 10 times its fitted value, but there was no corresponding change in the spike inference
738 quality. The decrease in indicator concentration caused a reduction in the increase in $\Delta F / F_0$
739 in response to an action potential, and an increase in the decay time of this increase (figure
740 2.5a). The increase in indicator concentration had the opposite effect, it caused an increase
741 in the change in $\Delta F / F_0$ in response to an action potential, and a decrease in the decay time.

742 Third, the concentration and types of endogenous calcium buffers also vary from neuron
743 to neuron, both within and between cell types (Bartol et al., 2015; Maravall et al., 2000;
744 Neher and Augustine, 1992). Since the calcium buffer capacity of neurons is high, around
745 50-70 (Lee et al., 2000) in excitatory hippocampal pyramidal cells, around 100-250 (Lee et
746 al., 2000) in inhibitory hippocampal pyramidal cells, and 900-200 in Purkinje cells (depend-
747 ing on the age of the subject), these endogenous buffers compete with GCaMP for binding
748 to calcium, and variations in endogenous buffer concentration may affect GCaMP signal and
749 therefore spike inference. To address this we varied the concentration of the endogenous
750 buffer in the model neuron over five orders of magnitude from 0.8 to 8000 μM , simulated
751 calcium fluorescence traces in response to the same set of spike trains, and performed spike
752 inference on the resulting fluorescence time series. Increasing the endogenous buffer con-
753 centration had a substantial effect on the GCaMP fluorescence signal, both decreasing its
754 amplitude and slowing its kinetics (figure 2.6(a)). This corresponded with a decrease in both
755 single-spike signal-to-noise ratio (figure 2.6(b)) and spike inference accuracy (figure 2.6(c)).
756 In contrast, decreasing endogenous buffer capacity from the fitted value had little effect on
757 either the GCaMP signal or spike inference (figure 2.6).

758 **2.2.5 Single spike inference accuracy drops for high firing rates, but firing rate
759 itself can be estimated from mean fluorescence amplitude**

760 The fluorescence signal recorded from neurons using calcium indicators is typically much
761 slower than changes in membrane potential for two reasons: first, because the calcium and
762 the indicator have slow binding and unbinding kinetics, the signal is a low-pass filtered ver-
763 sion of the membrane potential. Second, neuronal two-photon imaging experiments are often
764 performed in scanning mode, which limits their frame rate to $\sim 10\text{Hz}$ or slower. This im-
765 plies that multiple spike events that occur close in time might be difficult to resolve from a

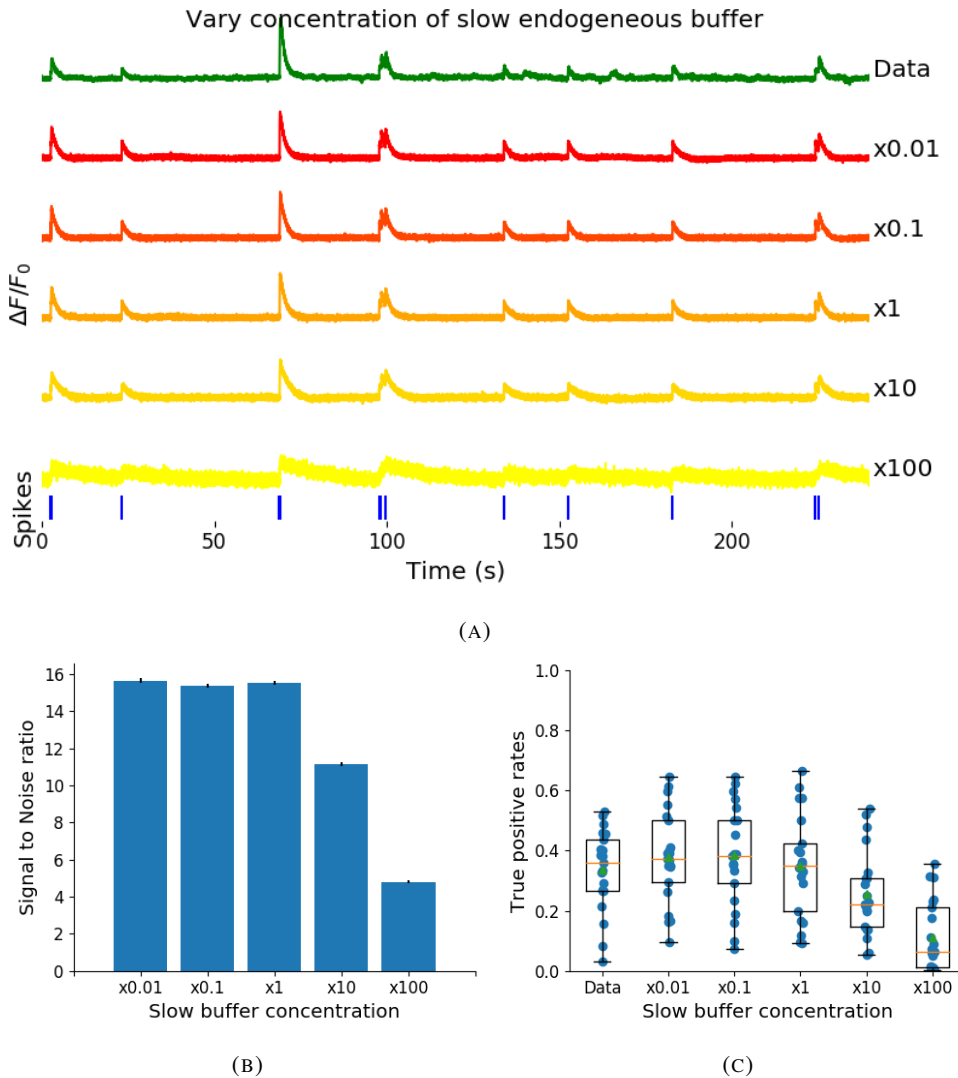


FIGURE 2.6: (a) An example trace for each of the five perturbed values for the concentration of immobile endogenous buffer. (b) The signal-to-noise ratio of the modelled fluorescence traces using each of the four perturbed values, and the experimental value. The lower values for the immobile buffer produce the same SNR as the experimental value. But the higher perturbed values produce fluorescence traces with a lower SNR. (c) The true-positive rates of the deconvolution algorithm's predictions when inferring from the observed data, and inferring from modelled traces using the perturbed and experimental values.

766 calcium indicator time series. Many cells, especially several types of inhibitory interneurons,
 767 fire tonically at rates higher than 10Hz. We used the model to test whether spike inference
 768 accuracy depended on the neuron's firing frequency by driving the cell with spike trains sam-
 769 pled from a Poisson processes of varying frequency. We simulated a variable firing rate using
 770 an Ornstein-Uhlenbeck process, and simulated the spike trains using a Poisson distribution
 771 with its rate taken from this process. Because of the high frequency firing rate of these spike
 772 trains, we used the accuracy as the measure of spike inference quality. We simulated 30
 773 spike trains at average firing rate of 1, 5, and 10Hz, and measured the spike inference quality
 774 of all these traces. Spike inference accuracy decreased with increasing firing rate, for up to
 775 10Hz Poisson spike trains (figure 2.8(left)). Although, the accuracy remained above 90% for
 776 each of the three frequencies. We also plotted the average $\Delta F/F_0$ as a function of stimula-
 777 tion firing rate. We found that it increased monotonically as a function of firing rate (figure
 778 2.8(right)).

779 We expected lower spike inference quality as the average spiking frequency increased.
 780 Since the fluorescence trace, in some sense, is a low pass filtered version of the spike train, a
 781 tightly packed groups of spikes will be more difficult to infer than isolated spikes. However,
 782 the increasing amplitude of the fluorescence trace with increasing frequency suggests that
 783 some spike inference algorithm could be developed based on this amplitude.

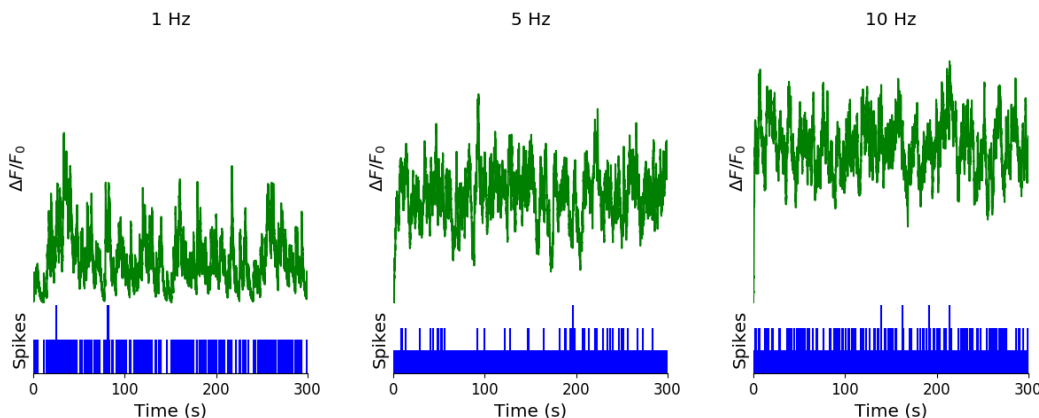


FIGURE 2.7: **Simulating fluorescence traces at different firing rates** Example modelled traces created using simulated spike trains with a mean fir-
 ing rate of 1Hz (left column), 5Hz (middle column), and 10Hz (right col-
 umn). Note the difference in amplitude with different mean firing rates.

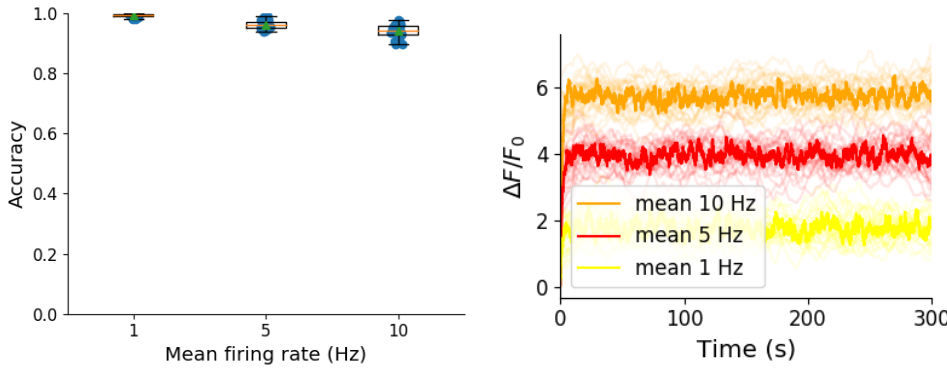


FIGURE 2.8: **Inference quality and $\Delta F/F_0$ vs Firing rate** (left) The spike inference accuracy when applied to 30 traces created using simulated spike trains with mean firing rates of 1, 5, and 10 Hz. (right) The mean $\Delta F/F_0$ across those 30 traces for each frequency.

784 2.3 Discussion

785 We designed a biophysical model for the changes in free calcium and bound calcium con-
 786 centrations within a cell soma with a fluorescent calcium indicator. We used this model to
 787 model the fluorescence trace resulting from a spike train in this cell. We fit the free parame-
 788 ters of the model by matching the power spectrum and amplitude of fluorescence traces with
 789 simultaneously measured spike trains. We inferred spikes from real fluorescence traces and
 790 modelled fluorescence traces, and measured the quality of the spike inference in both cases.
 791 We found that the spike inference quality was similar in both cases. We perturbed the concen-
 792 tration of the calcium buffers in the model, and the binding/unbinding rates of those buffers
 793 in the model, and measured the effect on the signal-to-noise ratio (SNR) of the modelled
 794 fluorescence traces and the spike inference quality.

795 For the fluorescent calcium indicator, we found that any large perturbation away from
 796 the experimental value led to a reduction in SNR, and spike inference quality. For the bind-
 797 ing/unbinding rates, we kept the ratio of these rates constant, but altered their values in paral-
 798 lel. The lower values caused a reduction in SNR, and a reduction in spike inference quality.
 799 For the endogenous buffer concentration, an increase above the experimental value caused a
 800 reduction in SNR and spike inference quality.

801 Although the model produced visually similar time series to the real data, there were a
 802 few aspects it did not capture. First, the real data featured some low-frequency components
 803 that did not appear related to the spike events. These were not captured by the models we
 804 used in this study, but could be added in future by adding a suitable low-frequency term to the
 805 resulting time series. Second, the real data seemed to have some nonlinearities not captured in

806 the model, for example the response to two nearby spikes was greater than expected from the
807 linear sum of two single spikes. This may be due to the co-operative binding of Calmodulin
808 to calcium, which gives calmodulin a supra-linear sensitivity to calcium concentration. The
809 model, in contrast behaved much more linearly, but could be extended in future to include
810 such nonlinearities. Third, in the real data the fluorescence peak amplitude seemed to vary
811 from spike to spike, even for well-isolated spike events. However in our model we assumed
812 each spike lead to the same fixed-amplitude injection of calcium to the cell, leading to much
813 greater regularity in fluorescence peak amplitudes. This variability could be added in future
814 versions of the model by making the injected calcium peak a random variable. Fourth, we
815 modelled the soma as a single compartment, but in reality there is likely a non-uniform spatial
816 profile of calcium concentration. This may matter because some endogenous buffers might
817 access calcium right as it influxes from the extracellular space, whereas the majority of the
818 fluorescence signal is more likely coming from the bulk of the cytoplasm. Future models
819 could attempt to model these spatial dependencies to assess whether they affect the overall
820 spike inference procedure.

821 As well as the optimised parameters, the model has 14 fixed parameters than can be
822 changed to simulate different types of calcium indicators. This model could be used to test
823 the theoretical performance of proposed new types of calcium indicator. The model could
824 also be used by developers of spike inference algorithms to test the effects of changing cal-
825 cium indicator parameters on spike inference, or to test the affects of changing spiking char-
826 acteristics on spike inference. For example, high firing rate vs low firing rate, or bursting vs
827 no bursting. Given the increasing amplitude of the fluorescence trace with increasing mean
828 firing rate, it would be possible to build a spike inference algorithm on this principle at least
829 in part.

830 Our model has already been used as a tool by our colleagues, for simulating fluorescence
831 traces in response to cells that can fire with a continuous rate between 10 and 20Hz, but do
832 not always do so. Our colleagues found that a combination of the amplitude and the variance
833 of the simulated fluorescence trace was the best indicator of firing rate. For example, when
834 a cell was not firing, the amplitude and variance of the fluorescence trace was relatively low.
835 When the cell fired with a low firing rate \sim 1Hz, the mean amplitude was still low but
836 the variance of the fluorescence trace was high, and for high firing rate \sim 10 – 20Hz, the
837 fluorescence amplitude was high, and the variance was low. In this way, our model may be
838 useful for investigating firing rates underlying real fluorescence traces in response to cells
839 which can fire in these rage ranges.

840 A recent paper by Greenberg et al (2018) described a biophysical model for spike train
841 inference called the ‘Sequential binding model’. Similar to our model, this model included
842 parameters for two types of endogenous buffer. But this model also included dynamics for
843 calcium binding to and unbinding from these endogenous buffers. Furthermore, this model
844 included dynamics for calcium binding to and unbinding from the four binding sites present
845 on a GCaMPs6 molecule. In the accuracy measurements specified in that paper, this model
846 performed better than the MLspike algorithm, which is also partially a biophysically model,
847 and it performed better than the constrained non-negative deconvolution algorithm. The se-
848 quential binding model also biophysically interpretable parameters, and its fitted parameters
849 for quantites such as buffering capacity and calcium influx upon action potential firing fall in
850 line with experimental values (Greenberg et al., 2018). Biophysical models like this appear
851 to be the way forward for spike inference algorithms.

852 2.4 Methods

853 2.4.1 Calcium dynamics model

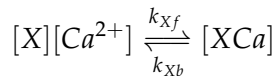
854 We wrote a biophysical model of the calcium dynamics within a cell soma. When a neu-
855 ron fires an action potential, voltage-dependent calcium ion-channels open up that allow a
856 current of Ca^{2+} to flow into the neuron (Koch, 1999). The increase in the free calcium ion
857 concentration inside of the cell, along with changes in the concentration of potassium and
858 sodium, causes the change in cell membrane potential, which must be depolarised. The de-
859 polarising process consists of free calcium ions leaving the cell through open ion channels,
860 or binding to molecules within the cell called buffers, or calcium storage by organelles such
861 as the endoplasmic reticulum. A diagram illustrating the cell, its channels, and its buffers
862 can be seen in figure 2.1A. There are several different types of calcium buffer, each with
863 different dynamics and different concentrations within different types of excitable cell. The
864 fluorescent calcium indicator is another calcium buffer, with the useful property that when it
865 is bound to a calcium ion, the bound molecule may become excited by a photon and release
866 a photon in return. This is what creates the fluorescence. After the action potential has taken
867 place, the free calcium concentration within the cell will return to a baseline level (Maravall
868 et al., 2000).

869 We modelled the the dynamics of five molecular concentrations,

- 870 • Free calcium ion concentration, $[\text{Ca}^{2+}]$

- 871 • Fluorescent indicator bound calcium, $[BCa]$
- 872 • Endogenous mobile buffer bound calcium, $[ECa]$
- 873 • Endogenous immobile buffer bound calcium, $[ImCa]$
- 874 • Excited buffered calcium, $[BCa^*]$

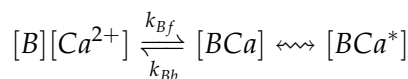
The term ‘buffering’ refers to free calcium ions coming into contact with buffer molecules and binding together. Diagrammatically:



875 where $[X]$ represents any buffer molecule, and k_{X_f} and k_{X_b} represent the binding and un-
 876 binding (dissociation) rates in units of per molar concentration per second ($M^{-1} s^{-1}$) and per
 877 second (s^{-1}) respectively. The speed of this chemical reaction is determined by the binding
 878 and unbinding rates.

879 There are a number different endogenous buffers in any neuron. Which buffers are
 880 present, and the buffers’ concentrations vary from cell to cell. In order to capture the ef-
 881 fects of mobile and immobile endogenous buffers without introducing several parameters,
 882 they were modelled as two buffers. One representing mobile buffers and the other represent-
 883 ing immobile buffers. Each with their own binding and unbinding rates.

The fluorescent calcium indicator behaves similarly to the other calcium buffers. The calcium is buffered by the indicator in the same way. But an indicator bound calcium molecule can become excited by absorbing the energy from a photon. An excited indicator bound calcium molecule can then release a photon to go back to its ‘relaxed’ state.



884 The released photons are captured by a photon collector. This gives us the fluorescence trace.
 885 Ignoring the baseline level of free calcium in a neuron, the system of equations we used
 886 to model all of these interactions is as follows:

$$\begin{aligned} \frac{d[Ca^{2+}]}{dt} = & k_{Bb}[BCa] + k_{Eb}[ECa] + k_{Imb}[ImCa] \\ & - k_{Bf}[B][Ca^{2+}] - k_{Ef}[E][Ca^{2+}] - k_{Imf}[Im][Ca^{2+}] \\ & + \beta([Ca_0^{2+}] - [Ca^{2+}]) \end{aligned} \quad (2.1)$$

$$\frac{d[BCa]}{dt} = k_{Bf}[B][Ca^{2+}] - k_{Bb}[BCa] + r[BCa^*] - \eta[BCa] \quad (2.2)$$

$$\frac{d[ECa]}{dt} = k_{Ef}[E][Ca^{2+}] - k_{Eb}[ECa] \quad (2.3)$$

$$\frac{d[ImCa]}{dt} = k_{Imf}[Im][Ca^{2+}] - k_{Imb}[ImCa] \quad (2.4)$$

$$\frac{d[BCa^*]}{dt} = \eta[BCa] - r[BCa^*] \quad (2.5)$$

where $[Ca_0^{2+}]$ is the baseline calcium concentration within the cell soma, β is a rate defining how quickly free calcium enters or leaves the cell in the absence of an action potential, η is the excitation rate for indicator bound calcium, r is the photon release rate for the excited indicator bound calcium, and f and b are used to indicate the forward and backward rates for chemical reactions respectively. The excitation rate defines the proportion of indicator bound calcium that becomes excited at each time step. The photon release rate defines the proportion of excited indicator bound calcium that releases a photon and returns to its relaxed state at each time step. An action potential is modelled as a discontinuous increase in the free calcium concentration to an appropriate value (Maravall et al., 2000).

Note that each of the three pairs of binding and unbinding terms in the first equation has a corresponding pair in one of the subsequent three equations. Binding removes a free calcium molecule and adds a bound calcium molecule, and unbinding does the opposite.

When using this model to simulate a fluorescence trace, the system of equations above are first solved over a period of 25s without action potentials. This lets each of the five tracked chemical concentrations reach their steady state. Then we use the given spike train and the parameters to model the fluorescence trace.

Note that since the model has no spatial component, the mobile and immobile buffers only differ in their binding and unbinding rates.

Photon release & capture

We used a simple model for the photon release. The number of photons released at each time step was controlled by the number of excited indicator bound calcium molecules in the cell and a parameter called the ‘release rate’. The release rate is an optimised free parameter of the model.

As for the photon capture, in two-photon excitation microscopy the photons scattered by the fluorescent indicator get scattered in all directions. Therefore the number of photons detected is stochastic. This made the process for capturing photons the natural source of noise in the system. The number of photons captured, and therefore the intensity of the

914 fluorescence, is modelled using a binomial distribution. The number of photons released was
915 used as the number of trials. The probability of success, or ‘capture rate’ was a free parameter
916 of the model that we optimised.

917 **2.4.2 Parameter optimisation**

918 The free parameters of the model are as follows:

919 **Calcium rate, β** Controls how quickly the concentration of free calcium will be driven to
920 the baseline concentration.

921 **Capture rate, p** The average proportion of photons captured by the photon detector.

922 **Excitation rate, η** The number of indicator bound calcium molecules that become excited
923 by photon bombardment at each time step.

924 **Release rate, r** The number of excited indicator bound calcium molecules that release a
925 photon at each time step.

926 To optimise the free parameters given a fluorescence trace, we applied the following proce-
927 dure:

- 928 1. The frequency power spectrum of the trace was measured.
- 929 2. The power spectrum was smoothed using a boxcar smoother (aka. sliding average, box
930 smoother).
- 931 3. The log of the smoothed power spectrum was measured.
- 932 4. Use the model to create a modelled fluorescence trace.
- 933 5. Apply steps 1, 2, and 3 to the modelled fluorescence trace.
- 934 6. Calculate the root mean squared difference between the log power of the actual fluo-
935 rescence trace, and the log power of the modelled fluorescence trace.
- 936 7. Calculate the root mean squared difference between the actual fluorescence trace and
937 the modelled fluorescence trace.
- 938 8. Use an optimisation algorithm to reapply this process, attempting to minimize the sum
939 of the two root mean squared differences at each iteration.

940 Using the root mean squared difference of the log power spectra as part of the objective
941 function forces the model to match the noise frequency of the actual fluorescence. Using
942 the root mean squared difference of the traces themselves forces the model to match the
943 amplitude of the fluorescence trace more accurately.

944 In order to minimise the objective function, a suite of meta-heuristic optimisation (aka.
945 black-box optimisation) algorithms were implemented on each of the traces in the dataset.
946 These methods were chosen because they don't require a gradient for the objective function
947 (gradient-free) and they are particularly useful for minimising stochastic objective functions
948 like the one we used here. The free parameters were optimised for each individual fluores-
949 cence trace. The most successful method for each trace was recorded. The method that was
950 most often successful was probabilistic descent, and the second most successful method was
951 generating set search. Both of these methods are examples of pattern search. These two
952 methods were the best optimisers on about 75% of the traces in the dataset.

953 Although this optimisation procedure minimises the value of the optimisation function,
954 the value never reaches zero for a number of reasons. Firstly, the fluorescence traces carry low
955 frequency fluctuations that cannot be captured by the model. Secondly, the model assumes
956 that the process of calcium binding to the fluorescent indicator is linear in time (see equation
957 1), but there are more complicated dynamics involved here. Fluorescent calcium indicators
958 are often built upon the calcium binding protein called 'calmodulin'. This protein has four
959 calcium binding sites. These sites are locally split into two pairs. Each pair has a different
960 affinity for calcium, and the affinity of the binding sites is affected by the occupancy of
961 the other binding sites (Kilhoffer et al., 1992). So the calcium to calcium indicator binding
962 process is non-linear, but the model does not take this into account.

963 **Fixed parameters**

964 As well as the optimised parameters mentioned in section 2.4.2, the model also has thirteen
965 fixed parameters. Please see table 2.1 for details of these parameters and their values. In
966 an application of the model, these parameters can be changed in order to model any given
967 fluorescent calcium indicator.

968 **2.4.3 Julia**

969 The programming language used to write and execute the model was 'Julia'. Julia is a dy-
970 namic programming language designed for technical computing. Julia was designed specif-
971 ically to provide a convenient high-level dynamic language similar to MATLAB, or Python,

Parameter	Description	Value	Source
baseline	The baseline concentration of free calcium within the cell soma	$4.5 \times 10^{-8} \text{M}$	(Maravall et al., 2000)
cell radius	The radius of the soma (assumed to be spherical)	10^{-5}M	(Fiala and Harris, 1999)
endogenous	The concentration of endogenous mobile buffer within the cell soma	10^{-4}M	(Faas et al., 2011)
frequency	The frequency at which the spike trains are sampled.	100Hz	
immobile	The concentration of endogenous immobile buffer within the cell soma	$7.87 \times 10^{-5} \text{M}$	(Bartol et al., 2015)
indicator	The concentration of fluorescent indicator within the cell soma	10^{-4}M	(Maravall et al., 2000)
k_{Bb}	The unbinding rate of the fluorescent calcium indicator	160s^{-1}	(Bartol et al., 2015)
k_{Bf}	The binding rate of the fluorescent calcium indicator	$7.77 \times 10^8 \text{s}^{-1} \text{M}^{-1}$	(Bartol et al., 2015)
k_{Eb}	The unbinding rate of the endogenous mobile buffer	10^4s^{-1}	(Bartol et al., 2015)
k_{ef}	The binding rate of the endogenous mobile buffer	$10^8 \text{s}^{-1} \text{M}^{-1}$	(Bartol et al., 2015)
k_{Imb}	The unbinding rate of the endogenous immobile buffer	524s^{-1}	(Bartol et al., 2015)
k_{Imf}	The binding rate of the endogenous immobile buffer	$2.47 \times 10^8 \text{s}^{-1} \text{M}^{-1}$	(Bartol et al., 2015)
peak	The increase in free calcium concentration within the cell induced by an action potential	$2.9 \times 10^{-7} \text{M}$	(Maravall et al., 2000)

TABLE 2.1: **Fixed parameters** A table of the parameters fixed before optimising the model. The values of these parameters could be changed to model different fluorescent calcium indicators.

972 with improved performance. Julia’s type system and Julia’s direct interfaces with C and
973 Fortran allow this aim to be achieved (Bezanson et al., 2012). The Julia version of the
974 ‘Sundials’ package for ODE solving was used to solve the system of equations above. The
975 BlackBoxOptim.jl package for Julia was used to perform the optimisation.

976 **2.4.4 Spike inference**

977 We used spike inference algorithms to compare the quality of spike inference using the mod-
978 elled traces to the quality of spike inference using the observed traces. We also used the
979 spike inference algorithms to assess the effect of parameter perturbation on the spike infer-
980 ence. Three algorithms were used:

981 **Constrained non-negative deconvolution algorithm (aka Pnevmatikakis algorithm)** This
982 algorithm uses a constrained version of non-negative Weiner deconvolution to infer a
983 calcium signal and a ‘spiking activity signal’ from the fluorescence trace (Vogelstein
984 et al., 2010; Pnevmatikakis et al., 2016). The spiking activity signal is a non-negative
985 vector of real numbers reflecting the cell’s activity rather than an actual spike train. We
986 inferred a spike train by choosing an optimised threshold for the spiking activity sig-
987 nal. Whenever the spiking activity signal exceeded that threshold, an action potential
988 was inferred. The threshold was optimised by minimising the difference between the
989 number of spikes observed and the number of spikes predicted.

990 **ML-Spike algorithm** This algorithm uses a generalised version of the Viterbi algorithm to
991 return the spike train that maximises the likelihood of producing the given fluorescence
992 trace. The Viterbi algorithm is an algorithm for estimating the most likely sequence
993 of hidden states resulting in a sequence of observed states in a discrete-time finite-
994 state Markov process (Forney, 1973). In this case, each hidden state is defined by the
995 presence or absence of an action potential, and each observed state is the value of the
996 fluorescence trace at each time step. This algorithm assumes that the concentration of
997 calcium within the cell will decay to a drifting baseline, rather than a fixed baseline
998 (Deneux et al., 2016).

999 **Online Active Set method to Infer Spikes (OASIS)** This algorithm is once again based on
1000 an auto-regressive model of the fluorescence trace, but can be generalised to any or-
1001 der. The algorithm itself is a generalisation of the pool adjacent violators algorithm
1002 (PAVA) that is used in isotonic regression. The OASIS algorithm works through the

1003 fluorescence trace from beginning to end, this combined with the speed of the algo-
1004 rithm means that it could be used for real-time online spike inference (Friedrich and
1005 Paninski, 2016). Given a fluorescence trace, the algorithm will return the most likely
1006 spike train and an inferred denoised fluorescence signal.

1007 In order to quantify the quality of spike inference for a given algorithm, we ran that algorithm
1008 on all of the fluorescence traces in dataset number eight of the spike finder datasets. Then we
1009 measured some binary classification measures on the results. These measures included

- 1010 • Accuracy
- 1011 • True positive rate (aka recall, sensitivity, hit rate)
- 1012 • True negative rate (aka specificity)
- 1013 • Precision
- 1014 • Negative predicted value
- 1015 • False negative rate (aka miss rate)
- 1016 • False positive rate (aka fall-out)
- 1017 • False discovery rate
- 1018 • False omission rate

1019 In making these measurements, we allowed a tolerance of two subsequent time bins for spike
1020 prediction. For example, the spike train data is a vector of 0s and 1s, with one element for
1021 each time bin. A ‘0’ denotes inactivity, a ‘1’ denotes the presence of at least one action
1022 potential. The inferred spike trains produced by the spike inference algorithms take the same
1023 form. In our analysis, if a spike appeared in the inferred spike train up to two time frames
1024 after a spike in the observed spike train, that spike was considered correctly inferred i.e. a true
1025 positive. However, once a spike in the inferred spike train was matched to a spike from the
1026 observed spike train, the inferred spike could not be matched to another observed spike. To
1027 illustrate, if two spikes were inferred in the two time bins following an isolated observed
1028 spike, the first inferred spike was considered correctly inferred, but the second inferred spike
1029 was considered incorrectly inferred, i.e. a false positive.

1030 The most useful measure was the true positive rate. This is because the spiking is sparse
1031 and this measurement is sensitive to the number of spikes observed and inferred, but is not
1032 affected by the true negative or false negative rates. After optimising the parameters for each

1033 fluorescence trace we measured the spike inference quality for the observed fluorescence
1034 traces, and compared this to the spike inference quality for the modelled traces.

1035 When measuring the spike inference quality for higher frequency spike train (1 – 10Hz),
1036 we used the accuracy as our binary classification measure. At these frequencies the variance
1037 of the fluorescence trace was much higher than for sparser spiking regimes, therefore we
1038 wanted to take into account the number of false negatives inferred by the algorithm.

1039 **Comparing spike inference quality**

1040 In order to compare spike inference quality we had to use methods for comparing samples.
1041 When comparing the true positive rate distributions arising from two different datasets, or
1042 two different algorithms on the same dataset, we compared the distributions using a paired
1043 t-test.

1044 **2.4.5 Perturbation analysis**

1045 In order to measure the sensitivity of spike inference to changes in a given model parameter,
1046 we perturbed the parameter and compared the quality of spike inference with the perturbed
1047 parameters to the quality of spike inference with the experimental or optimised parameters.
1048 In order to maximise the possibility of observing a difference due to the perturbation, we
1049 perturbed the chosen parameter by a relatively large amount. For example, the experimen-
1050 tal value for the molar concentration of the fluorescent indicator within the cell was 10^{-4}M
1051 (Maravall et al., 2000). The perturbed values used for this parameter were 10^{-2}M , 10^{-3}M ,
1052 10^{-5}M , and 10^{-6}M . The quality of the inference was compared by measuring the true posi-
1053 tive rate for each perturbed value and using a t-test to compare the distributions of the results.

1054 This analysis was performed firstly without any optimisation of the free parameters for
1055 use with the perturbed parameters. Then the analysis was performed after the optimised
1056 parameters for each perturbed value were calculated.

1057 **2.4.6 Signal-to-noise ratio**

1058 To assess the effect of perturbation on the modelled traces, we measured and compared the
1059 signal to noise ratio (SNR) on each of the modelled traces. We calculated the SNR as the
1060 peak change in fluorescence divided by the standard deviation of the baseline fluctuation of
1061 the fluorescence trace (Tada et al., 2014). We measured these values by running the model
1062 on a spike train consisting a long period of inactivity followed by one action potential. We
1063 ran the model on this spike train one hundred times. We then measured the mean change

1064 in fluorescence and standard deviation of baseline activity across the one hundred modelled
1065 fluorescence traces, and calculated the SNR.

1066 **2.4.7 Data sources**

1067 All of the data used in this project was sourced from the ‘Spike Finder’ project (spikefinder.codeneuro.org).
1068 The data consisted of a collection of datasets with simultaneously measured fluorescence
1069 traces and action potentials (Berens et al., 2018).

1070 **Chapter 3**

1071 **Functional networks expand across**
1072 **anatomical boundaries as correlation**
1073 **time-scale increases**

1074 *Abstract*

1075 Decades of research has established that correlated spiking plays a crucial role in represent-
1076 ing sensory information. One drawback associated with the recent improvement in recording
1077 technology and consequent large datasets is the difficulty in analysing higher order correla-
1078 tions in large neuronal ensembles. One benefit of these datasets that has not yet been explored
1079 is the opportunity to compare correlations within anatomical regions to correlations across
1080 anatomical regions. In this work, we measured correlations between neurons residing in
1081 nine different brains regions in three awake and behaving mice. Using the these correlation
1082 measurements, we created weighted undirected graph networks and applied network science
1083 methods to detect functional communities in our neural ensembles. We compared these func-
1084 tional communities to their anatomical distribution. We repeated the analysis, using different
1085 timescales for our correlation measurements, and found that functional communities were
1086 more likely to be dominated by neurons from a single brain region at shorter timescales
1087 (< 100ms).

1088 3.1 Introduction

1089 Decades of research has established that correlations play a crucial role in representing sen-
1090 sory information. For example, the onset of visual attention has been shown to have a greater
1091 affect on the correlations in the macaque V4 region than on the firing rates in that region
1092 (Cohen and Maunsell, 2009). Recent findings show that spontaneous behaviours explain cor-
1093 relations in parts of the brain not associated with motor control (Stringer et al., 2019), that
1094 satiety state appears to have a brain wide representation (Allen et al., 2019), and that subject
1095 exploratory and non-exploratory states are represented in the amygdala (Gründemann et al.,
1096 2019). So, behavioural states are likely represented across many regions of the brain, not just
1097 motor related areas. In order to understand the brain, we must understand the interactions
1098 between neurons and regions.

1099 Because of limitations in recording technology almost all research has explored corre-
1100 lations between neurons within a given brain region, or within only two regions at most
1101 (Wierzynski et al., "2009"; Patterson et al., 2014; Girard, Hupé, and Bullier, 2001). Rel-
1102 atively little is known about correlations between neurons in many different brain regions.
1103 However, the recent development of ‘Neuropixels’ probes (Jun et al., 2017) has allowed
1104 extracellular voltage measurements to be collected from multiple brain regions simultane-
1105 ously routinely, and in much larger numbers than traditional methods. In this project we
1106 used a publicly-available Neuropixels dataset to analyse correlations between different brain
1107 regions (Stringer et al., 2019).

1108 A drawback associated with the improvement in recording technology is an increase in
1109 the difficulty in analysing these data. For example, analysing the i th order interactions of
1110 N neurons generally requires estimation of N^i parameters. A number that becomes astro-
1111 nomical for large N . New methods are required for analysing these new large datasets. We
1112 attempted to address this requirement in this piece of research by applying a cutting-edge
1113 network science community detection method to neural data.

1114 Another unexplored area of research is the changes in cell interactions at different timescales.
1115 Studies have shown different timescales for fluctuations in spiking activity (Murray et al.,
1116 2014), and different time scales for event representation (Baldassano et al., 2017) across dif-
1117 ferent brain regions. Still most studies focus on quantifying interactions at a given timescale.
1118 But neurons may interact differently, or may interact with different neurons at different
1119 timescales. Here we explore correlated communities of neurons at different timescales.

1120 In this work, we measured correlations between binned spike counts from neurons from

1121 nine different regions of the mouse brain. These measurements induced a weighted undi-
1122 rected graph or network where each neuron is represented by a node, and the strength of
1123 the connection between these nodes/neurons is the strength of the correlation between their
1124 spike counts. We then applied newly invented network methods (Humphries et al., 2019)
1125 to this network to find any community structure, and place the neurons in these correlation
1126 based communities. Finally, we compared these functional communities to the anatomical
1127 membership of the neurons.

1128 To investigate the functional communities and their relationship with anatomy at different
1129 time scales, we repeated these analyses using different length bin widths when binning spike
1130 times.

1131 To find and analyse functional networks while controlling for the subject’s behaviour, we
1132 conditioned the binned spike counts on data from a video of the subject’s face, and repeated
1133 our analysis for spike count correlations (or noise correlations) and signal correlations.

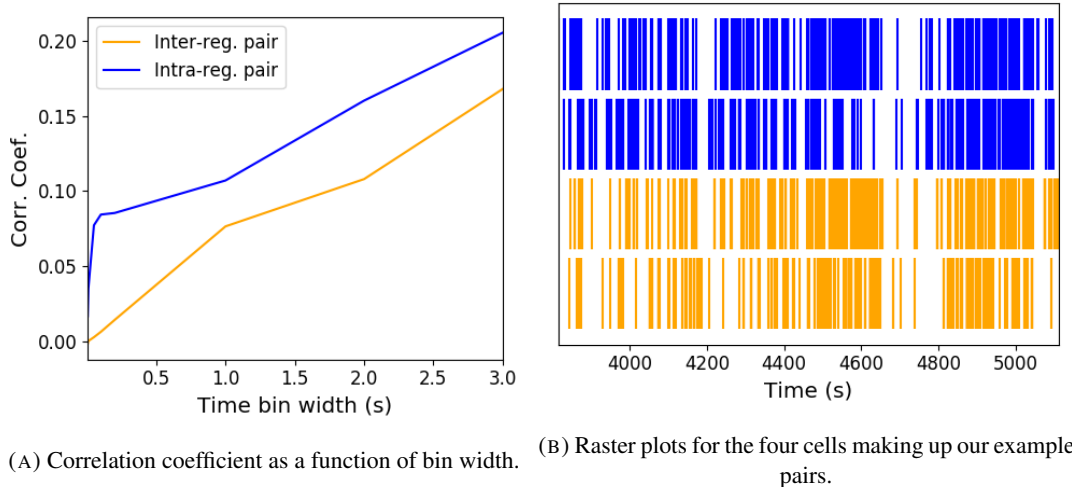
1134 3.2 Results

1135 Note that in the following text, we refer to the correlation coefficient between two sequences
1136 of spike counts from two different cells as the *total correlation*. We refer to the correlation
1137 between spike counts in response to a certain stimulus as the *spike count correlation* aka
1138 *noise correlation*, and we refer to the correlation between mean or expected responses to
1139 different stimuli as the *signal correlation* (Cohen and Kohn, 2011).

1140 The nine different brain regions from which we had data were the caudate putamen (CP),
1141 frontal motor cortex (FrMoCtx), hippocampus (HPF), lateral septum (LS), midbrain (MB),
1142 primary visual cortex (V1), superior colliculus (SC), somatomotor cortex (SomMoCtx), and
1143 thalamus (TH).

1144 3.2.1 Average correlation size increases with increasing time bin width

1145 First we inspected the affect of time bin width on total correlations. We know that using short
1146 time bins results in artificially small correlation measurements (Cohen and Kohn, 2011), so
1147 we expected to see an increase in correlation amplitude with increasing time bin width. That
1148 is exactly what we observed. Taking 50 cells at random, we calculated the total correla-
1149 tion between every possible pair of these cells, using different time bin widths ranging from
1150 0.005s to 3s. We found that the longer the time bin width, the greater the correlations (see
1151 figure 3.2a).



(A) Correlation coefficient as a function of bin width. (B) Raster plots for the four cells making up our example pairs.

FIGURE 3.1: (A) An example of the correlation coefficients between two different pairs of cells, one where both cells are in the same brain region (intra-regional pair), and one where both cells are in different brain regions (inter-regional pair). The correlation coefficients have been measured using different time bin widths, ranging from 5ms to 3s. Note the increasing amplitude of the correlations with increasing bin width. (B) A raster plot showing the spike times of each pair of cells.

1152 We also separated the positively correlated pairs from the negatively correlated pairs
 1153 using the mean correlation of each pair across all bin widths (see section 3.5.2). We found
 1154 that the positively correlated pairs become more positively correlated with increasing time bin
 1155 width, and the negatively correlated pairs become more negatively correlated with increasing
 1156 time bin width (see figures 3.2b and 3.2c).

1157 In figure 3.1a we plot correlations from two example pairs, one pair from within a region,
 1158 and one pair between regions. It can be seen that the correlation coefficient increases with
 1159 bin width. The correlations can be observed by eye in the raster plot for these cells in figure
 1160 3.1b.

1161 When taking the mean across all pairs, the positively correlated pairs dominate in terms
 1162 of both number of pairs, and amplitude of correlations. Therefore the mean across all pairs
 1163 is positive.

1164 These results were observed in each of the three mouse subjects from which we had data.

1165 3.2.2 Goodness-of-fit for Poisson and Gaussian distributions across increasing 1166 time bin widths

1167 We wanted to investigate if the width of the time bin used to bin spike times into spike counts
 1168 had an effect on the distribution of spike counts. We used the χ^2 statistic as a goodness-of-fit
 1169 measure for Poisson and Gaussian (normal) distributions to the spike count of 100 randomly

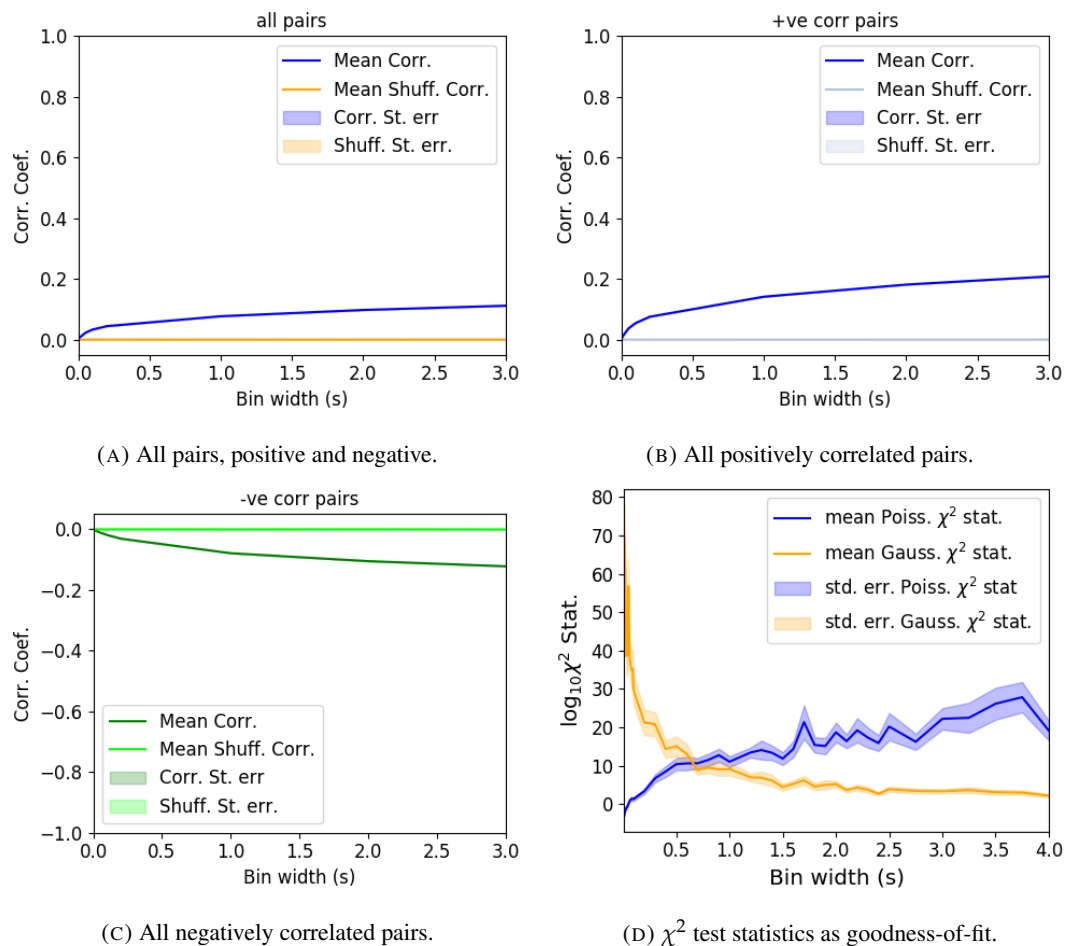


FIGURE 3.2: Mean correlation coefficients measured from pairs of 50 randomly chosen neurons. (A) All possible pairs, (B) positively correlated pairs, and (C) negatively correlated pairs. (D) Mean and standard error of χ^2 test statistics for Poisson and Gaussian distributions fitted to neuron spike counts.

1170 chosen neurons for a number of bin widths ranging from 0.01s to 4s. For the χ^2 statistic, the
1171 higher the value, the worse the fit.

1172 We expected a Poisson distribution to be a better fit for shorter time bin widths because
1173 spike counts must be non-negative, therefore any distribution of spike counts with mass dis-
1174 tributed at or close to 0 will be skewed. The distribution of spike counts is more likely to be
1175 distributed close to 0 when the time bin widths used to bin spike times into spike counts are
1176 small relative to the amount of time it takes for a neuron to fire an action potential ($\sim 1\text{ms}$ in
1177 the case of non-burst firing neurons).

1178 We expected a Gaussian distribution to be a better fit for longer time bin widths, because
1179 a Poisson distribution with a large rate is well approximated by a Gaussian distribution with
1180 mean and variance equal to the Poisson rate. Therefore, a Gaussian distribution would ap-
1181 proximate the mean of a collection of large spike counts, and have more flexibility than a
1182 Poisson distribution to fit the variance.

1183 We found that that a Poisson distribution is the best fit for shorter time bins less than 0.7s
1184 in length. Then a Gaussian distribution is a better fit for time bins greater than 0.7s in length
1185 (see figure 3.2d).

1186 3.2.3 Differences between and inter- and intra- regional correlations decrease 1187 with increasing bin width

1188 We investigated the differences in distribution between inter-regional correlations, i.e. corre-
1189 lations between neurons in different brain regions, and intra-regional correlations, i.e. corre-
1190 lations between neurons in the same brain region.

1191 Firstly, we investigated these quantities for all possible pairs of ~ 500 neurons taken
1192 from across all the 9 brain regions from which we had data. We distributed these neurons as
1193 evenly as possible across all of the regions, so that cells from one region would not dominate
1194 our data. We observed that the mean intra-regional correlations were always higher than the
1195 mean inter-regional correlations for every value of time bin width used. We also observed
1196 that as the time bin width increased these mean correlations increased and the difference
1197 between the mean inter-regional and intra-regional correlations grew (see figure 3.3 (Left)).

1198 Stringer et al. (2019) had a similar finding using the same data. They used only one value
1199 for the time bin width, 1.2s. Using this time bin width to bin spike times and measure total
1200 correlations, they found that the mean ‘within-region’ correlations were always greater than
1201 the ‘out-of-region’ correlations (Stringer et al., 2019). The figure from their paper showing
1202 this result can be seen in figure 3.3 (Right).

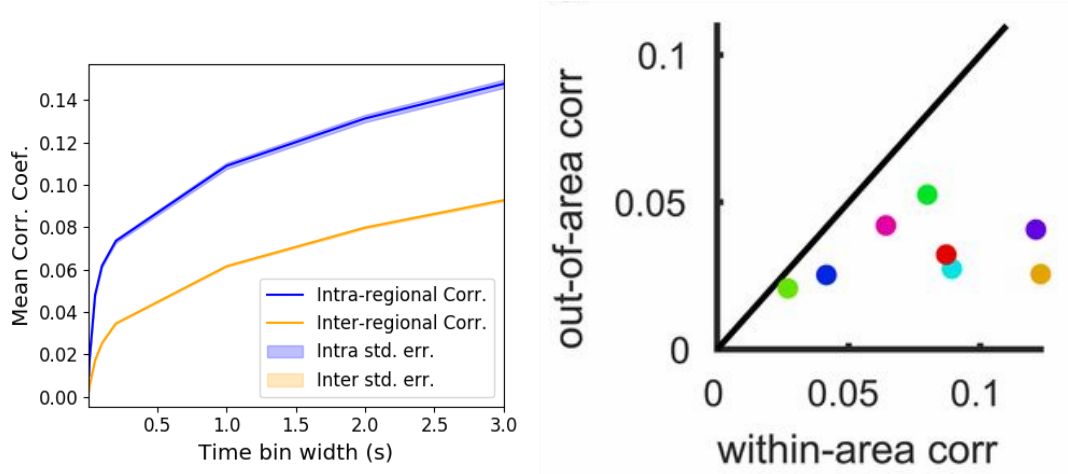


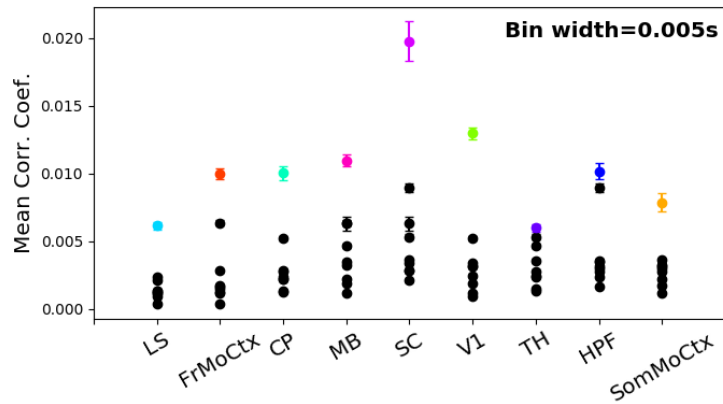
FIGURE 3.3: (Left) The mean intra-region and inter-region correlations using all possible pairs of ~ 500 neurons, spread across 9 different brain regions. (Right) Courtesy of Stringer et al. (2019), mean inter-regional (out-of-area) correlation coefficients vs mean intra-regional (within-area) correlation coefficients for a bin width of 1.2s. Note that the intra-regional coefficients are higher in each case.

1203 Examples of the correlations of one intra-regional pair and one inter-regional pair can be
1204 seen in figure 3.1.

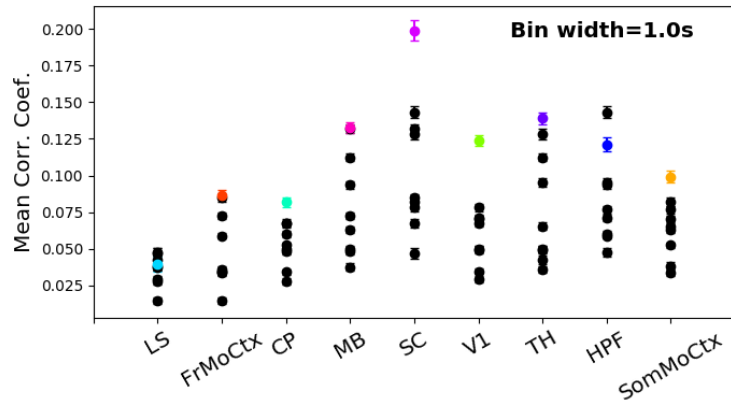
1205 Secondly, we separated those pairs into intra-regional and inter-regional groups. We
1206 noted that the mean intra-regional correlations (coloured dots in figures 3.4a and 3.4b) for
1207 a given region tended to be higher than the mean inter-regional correlations (black dots in
1208 figures 3.4a and 3.4b) involving cells from that region. However, in contrast with our previous
1209 result, we noted that the difference between the mean intra-regional correlations and most
1210 highly correlated inter-regional correlations reduced as we increased the time bin width (see
1211 figures 3.4a and 3.4b). This shows that the mean correlations shown in figure 3.3 are not
1212 distributed evenly across all region pair combinations.

1213 Finally, to see these regional mean correlations in a bit more detail, to examine the indi-
1214 vidual pair combinations in particular, we displayed these data in a matrix of mean corre-
1215 lations (see figure 3.5), showing the mean intra-regional correlations on the main diagonal, and
1216 the mean inter-regional correlations off diagonal. Comparing a version of this figure created
1217 using a short time bin width of 5ms (figure 3.5a) and a version using a longer time bin width
1218 of 1s (figure 3.5b) we observed that the mean intra-regional correlations are always relatively
1219 high in comparison to the mean inter-regional correlations, but the mean correlations in some
1220 inter-regional pairs are relatively much higher when using the longer time bin width.

1221 This could indicate information being processed quickly at a local or within-region level,
1222 and the local representations of this information spreading between regions at longer timescales.



(A) Mean inter-regional and intra-regional correlations using a time bin width of 5ms.



(B) Mean inter-regional and intra-regional correlations using a time bin width of 1s.

FIGURE 3.4: The mean intra-regional correlations (coloured dots) and mean inter-regional correlations (black dots) for a given region, indicated on the x-axis, for different time bin widths. Each black dot represents the mean inter-regional correlations between the region indicated on the x-axis and one other region. (A) shows these measurements when we used a time bin width of 5ms. (B) shows these measurements when we used a time bin width of 1s. Note that the difference between the mean inter-regional correlations and mean intra-regional correlations is smaller for 1s bins.

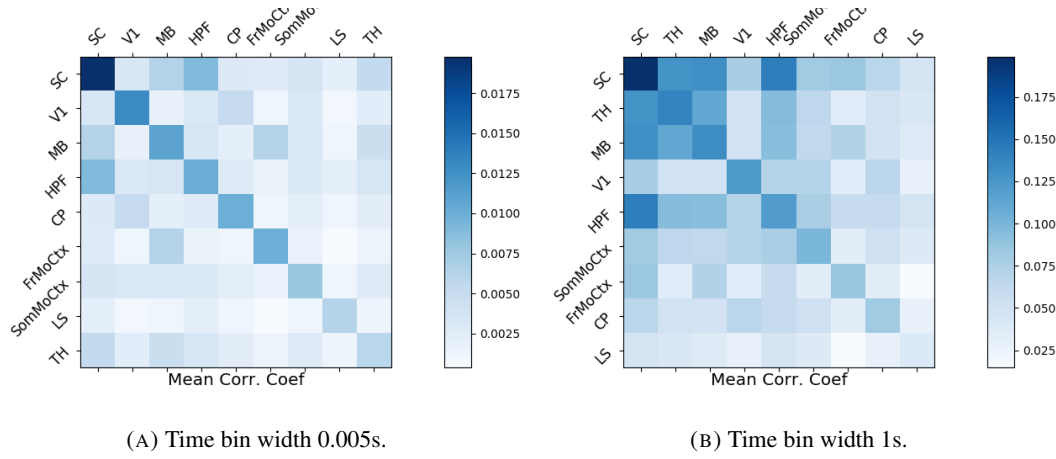


FIGURE 3.5: Mean inter-regional (main diagonal) and intra-regional (off diagonal) correlation coefficients. (A) Shows these measurements when spike times were binned using 5ms time bins. (B) Shows the same, using 1s time bins. Note that the matrices are ordered according to the main diagonal values, therefore the ordering is different in each subfigure.

1223 These results were consistent across the three mouse subjects. But, the relative magni-
 1224 tudes of the mean intra-regional and inter-regional correlations were not consistent. For ex-
 1225 ample, the region with the highest mean intra-regional correlations when using 1s bin widths
 1226 for subject one is the superior colliculus (SC), but for subject two it is the midbrain (MB).

1227 **3.2.4 Connected and divided structure in correlation based networks reduces
 1228 in dimension with increasing bin width**

1229 We used the correlation measurements to create weighted undirected graphs/networks where
 1230 each node represents a neuron, and the weight of each edge is the pairwise correlation be-
 1231 tween those neurons represented by the nodes at either end of that edge. We aimed to find
 1232 communities of neurons within these networks, and compare the structure of these commu-
 1233 nities to the anatomical division of those neurons. The first step of this process involved
 1234 applying the ‘spectral rejection’ technique developed by Humphries et al (2019) (Humphries
 1235 et al., 2019). This technique compares our data network to a chosen null network model, and
 1236 finds any additional structure in the data network beyond that which is captured in the null
 1237 network model (if there is any such structure).

1238 By comparing the eigenspectrum of the data network to the eigenspectrum of many sam-
 1239 ples from the null network model, this technique allows us to estimate the dimensionality of
 1240 the additional structure in the data network, and gives us a basis for that vector space. It also
 1241 divides the additional structure into connected structure, and k -partite (or divided) structure.
 1242 For example, if our algorithm found two dimensions of additional connected structure, and

1243 one dimension of additional divided structure. We might expect to find three communities,
1244 that is groups more strongly connected within group than without, and we might expect to
1245 find bi-partite structure, that is two sets that are more strongly connected between groups
1246 than within groups.

1247 The technique also finds which nodes contribute to this additional structure, and divides
1248 our data network into signal and noise networks. The details of spectral rejection and node
1249 rejection can be found in sections 3.5.5 and 3.5.5 respectively, and a full overview can be
1250 found in (Humphries et al., 2019).

1251 We chose the sparse weighted configuration model (see section 3.5.5) as our null network
1252 model. This model matches the sparsity and the total weight of the original network but
1253 distributes the weight at random across the sparse network.

1254 We applied the spectral rejection method to our networks based on total correlations using
1255 different values for the time bin width. We observed that for smaller time bin widths, our data
1256 networks had both k -partite structure, and community structure. As the width of the time bin
1257 increased, we found that the k -partite structure disappeared from our data networks, and the
1258 dimension of the community structure reduced in two of the three mice from which we had
1259 data (see figure 3.6).

1260 3.2.5 Detecting communities in correlation based networks

1261 We applied the community detection procedure described in section 3.5.5 to our signal net-
1262 works for our various time bin widths. We detected a greater number of smaller communities
1263 at shorter time bin widths, and a smaller number of larger communities for longer time bin
1264 widths (see figure 3.7). This was expected after the results found in section 3.2.4. We found
1265 more dimensions of additional structure at shorter time bin widths, therefore we found more
1266 communities at shorter time bin widths.

1267 We also noticed that at short time bin widths the communities detected tended to be
1268 dominated by cells from one region. Whereas communities existing in networks created
1269 using wider time bin widths tended to contain cells from many different brain regions. More
1270 on this in the next section.

1271 3.2.6 Functional communities resemble anatomical division at short timescales

1272 In order to quantify the similarity of the communities detected to the anatomical division of
1273 the cells. We treated both the anatomical division and the communities as clusterings of these
1274 cells. We then used measures for quantifying the difference or similarity between clusterings

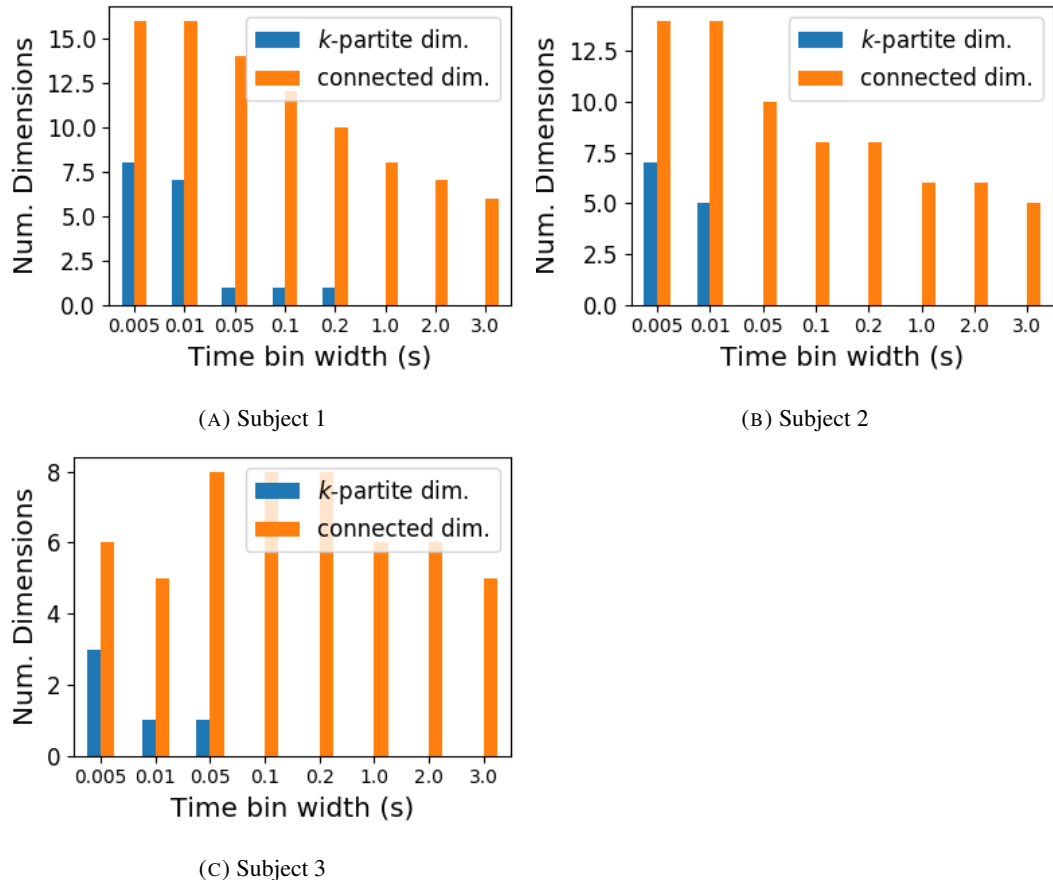


FIGURE 3.6: The number of dimensions in the *k*-partite and connected structure in the correlation based networks beyond the structure captured by a sparse weighted configuration null network model (see section 3.5.5), shown for different time bin widths. Note that the *k*-partite structure disappears for time bin width greater than 200ms for all three subjects. The dimension of the connected structure reduces with increasing bin width for 2 of the 3 subjects (top row).

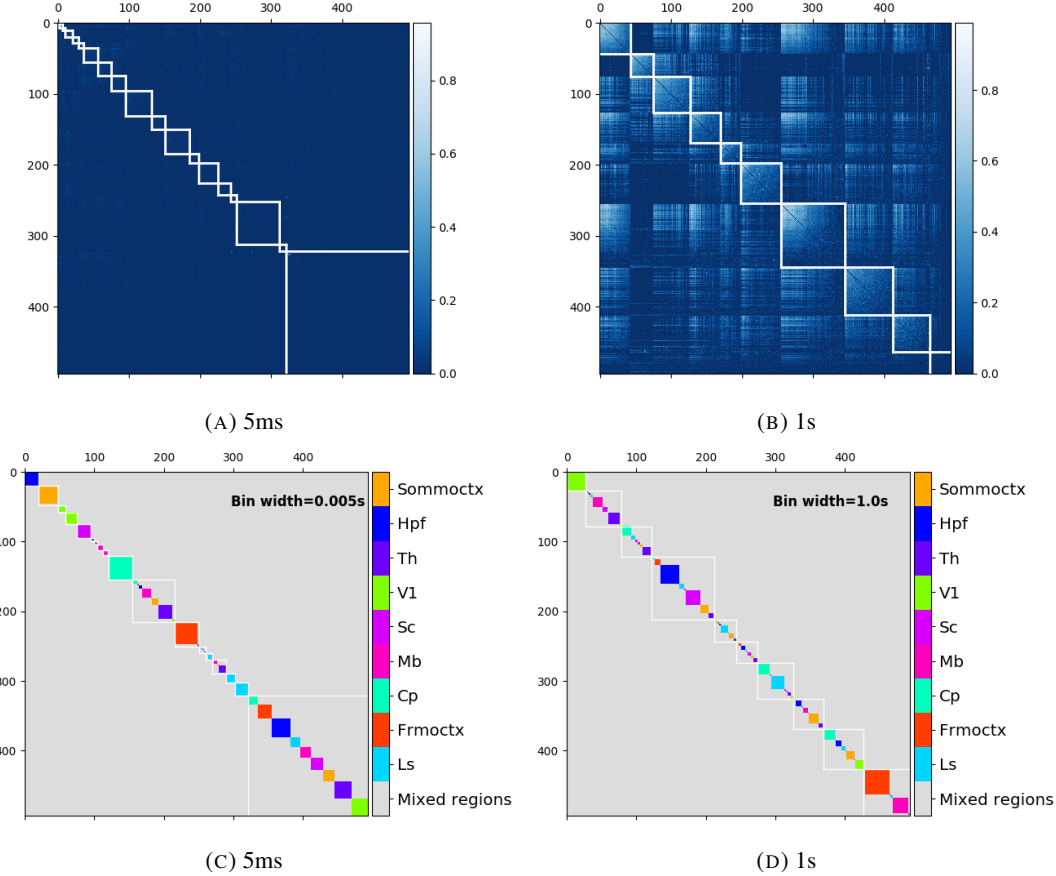


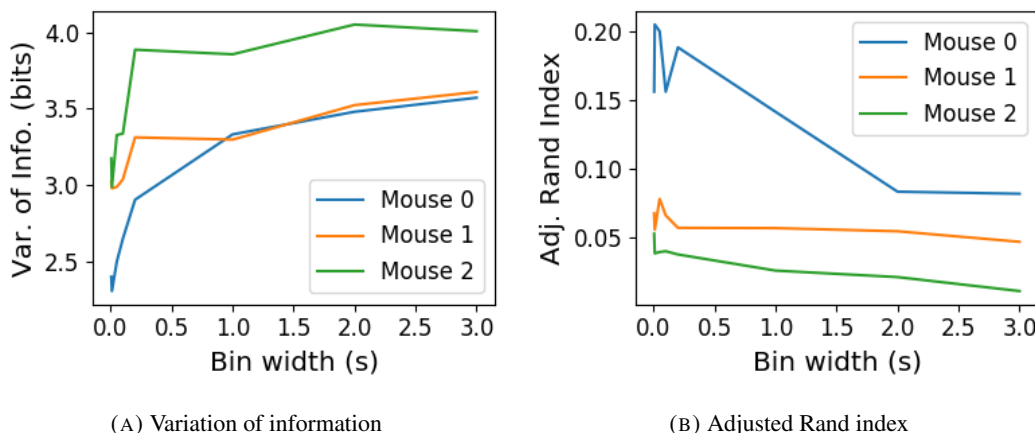
FIGURE 3.7: (A-B) Correlation matrices with detected communities indicated by white lines. Each off main diagonal entry in the matrix represents a pair of neurons. Those entries within a white square indicate that both of those neurons are in the same community as detected by our community detection procedure. Matrices shown are for 5ms and 1s time bin widths respectively. Main diagonal entries were set to 0. (C-D) Matrices showing the anatomical distribution of pairs along with their community membership. Entries where both cells are in the same region are given a colour indicated by the colour bar. Entries where cells are in different regions are given the grey colour also indicated by the colour bar.

1275 to quantify the difference or similarity between the detected communities and the anatomical
 1276 division. Details of these measures can be found in section 3.5.6 or in (Vinh, Epps, and
 1277 Bailey, 2010).

1278 We used two different types of measures for clustering comparison; information based
 1279 measures (see section 3.5.6) and pair counting based measures (see section 3.5.6). We include
 1280 one example of each in figure 3.8.

1281 The variation of information is the information based measure included in figure 3.8a.
 1282 This measure forms a metric on the space of clusterings. The larger the value for the variation
 1283 of information, the more different the clusterings.

1284 The adjusted Rand index is the pair counting based measure included in figure 3.8b. In
 1285 contrast with the variation of information, the adjusted Rand index is a normalised similarity
 1286 measure. The adjusted Rand index takes value 1 when the clusterings are identical, and takes
 1287 value 0 when the clusterings are no more similar than chance.



(A) Variation of information

(B) Adjusted Rand index

FIGURE 3.8: (A) The variation of information is a measure of distance between clusterings. The distance between the anatomical ‘clustering’ and community detection ‘clustering’ increases with increasing time bin width. (B) The adjusted Rand index is a normalised similarity measure between clusterings. The anatomical and community detection clusterings become less similar as the time bin width increases.

1288 Both measures indicated that the detected communities and the anatomical division of the
 1289 cells were more similar when we used shorter time bins widths (see figure 3.8). This indicates
 1290 that correlated behaviour in neuronal ensembles is more restricted to individual brain regions
 1291 at short timescales (< 250ms), and the correlated activity spreads out across brain regions
 1292 over longer time scales.

1293 **3.2.7 Conditional correlations & signal correlations**

1294 In light of the excellent research of Stringer et al (2019) showing that spontaneous behaviours
 1295 can drive activity in neuronal ensembles across the visual cortex and midbrain (Stringer et
 1296 al., 2019), we decided to control for the mouse’s behaviour when performing our analyses.
 1297 It is possible that our community detection process may be detecting communities across
 1298 multiple brain regions at longer time scales due to aggregating neuronal activity driven by
 1299 several spontaneous behaviours occurring during the time interval covered by a given time
 1300 bin. A time bin of 1s, for example, could contain a spike count where those spikes were driven
 1301 by different spontaneous behaviours. We aimed to investigate this possibility by applying our
 1302 community detection analysis to conditional correlation measures.

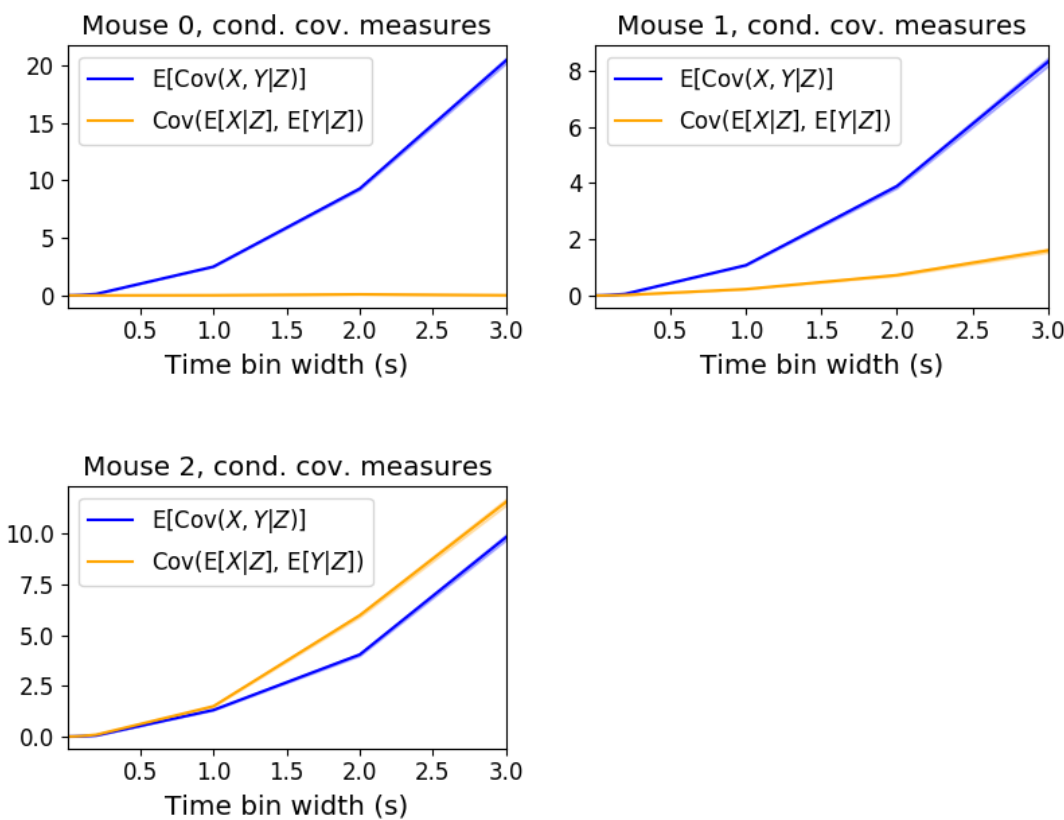


FIGURE 3.9: Comparing the components of the total covariance across different values for the time bin width. We observed a consistent increase in $E[\text{cov}(X, Y|Z)]$ as the time bin width increased. But we saw different trends for $\text{cov}(E[X|Z], E[Y|Z])$ for each mouse.

1303 We used the top 500 principal components of a video of the mouse’s face as a measure of
 1304 the mouse’s behaviour (see section 3.4.2). We modelled the spike counts as a linear combi-
 1305 nation of the principal components using linear regression with ElasticNet regularisation (see

section 3.5.3). Using this model, we quantified the expected spike count given the mouse’s behaviour $E[X|Z_1, \dots, Z_{500}]$.

We used these expected values to measure $\text{cov}(E[X|Z], E[Y|Z])$, and we used that value, the covariance $\text{cov}(X, Y)$, and the *law of total covariance* (see section 3.5.3) to measure $E[\text{cov}(X, Y|Z)]$. Here X and Y represent spike counts from individual cells, and Z is short-hand for the 500 principal components mentioned above. The two components of the covariance, $\text{cov}(E[X|Z], E[Y|Z])$ and $E[\text{cov}(X, Y|Z)]$, represent a ‘signal covariance’ and expected value of a ‘spike count covariance’ respectively, analogous to the signal correlation and spike count correlation (Cohen and Kohn, 2011).

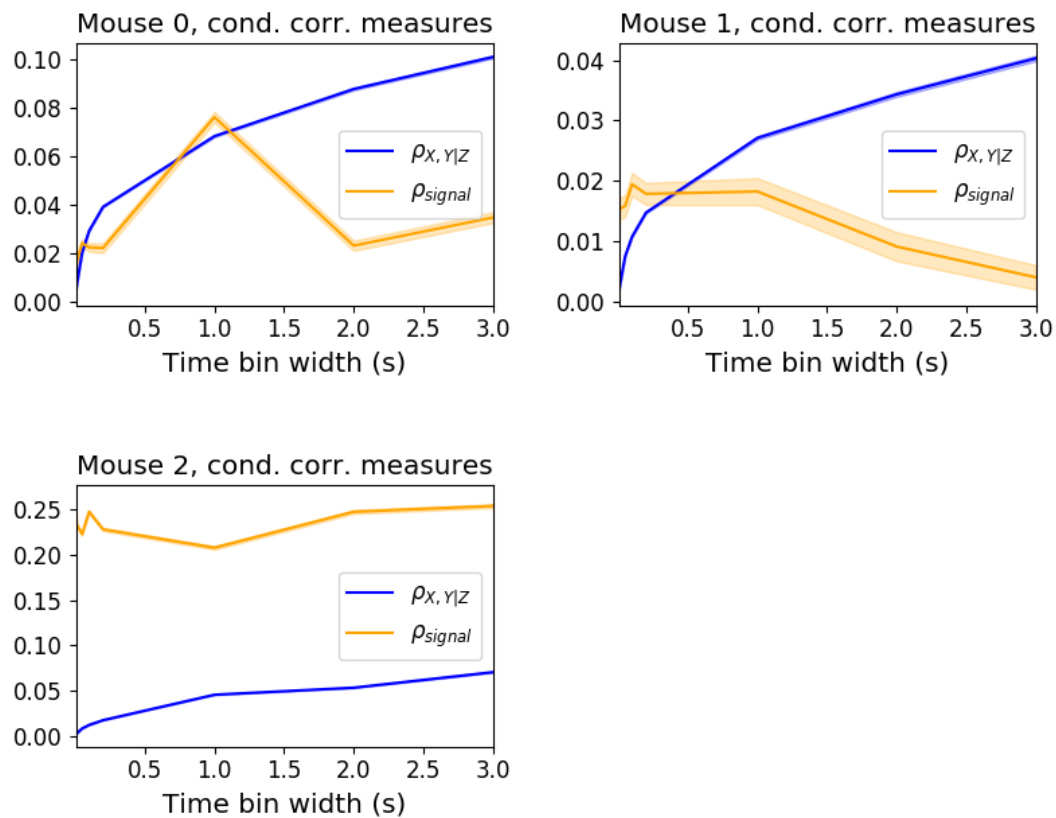


FIGURE 3.10: Comparing the components of the total covariance across different values for the time bin width. We saw a consistent increase in $\rho_{X,Y|Z}$ as the time bin width increased in all three subjects. But we saw different trends in ρ_{signal} for each of the subjects.

We examined the means of these components for different values of the time bin width (see figure 3.9). We observed a consistent increase in $E[\text{cov}(X, Y|Z)]$ as the time bin width increased. But we saw different trends for $\text{cov}(E[X|Z], E[Y|Z])$ for each mouse.

Using $\text{cov}(E[X|Z], E[Y|Z])$ we measured the signal correlation, ρ_{signal} , and using $E[\text{cov}(X, Y|Z)]$ we measured the event conditional correlation, $\rho_{X,Y|Z}$ (see section 3.5.3 for more details).

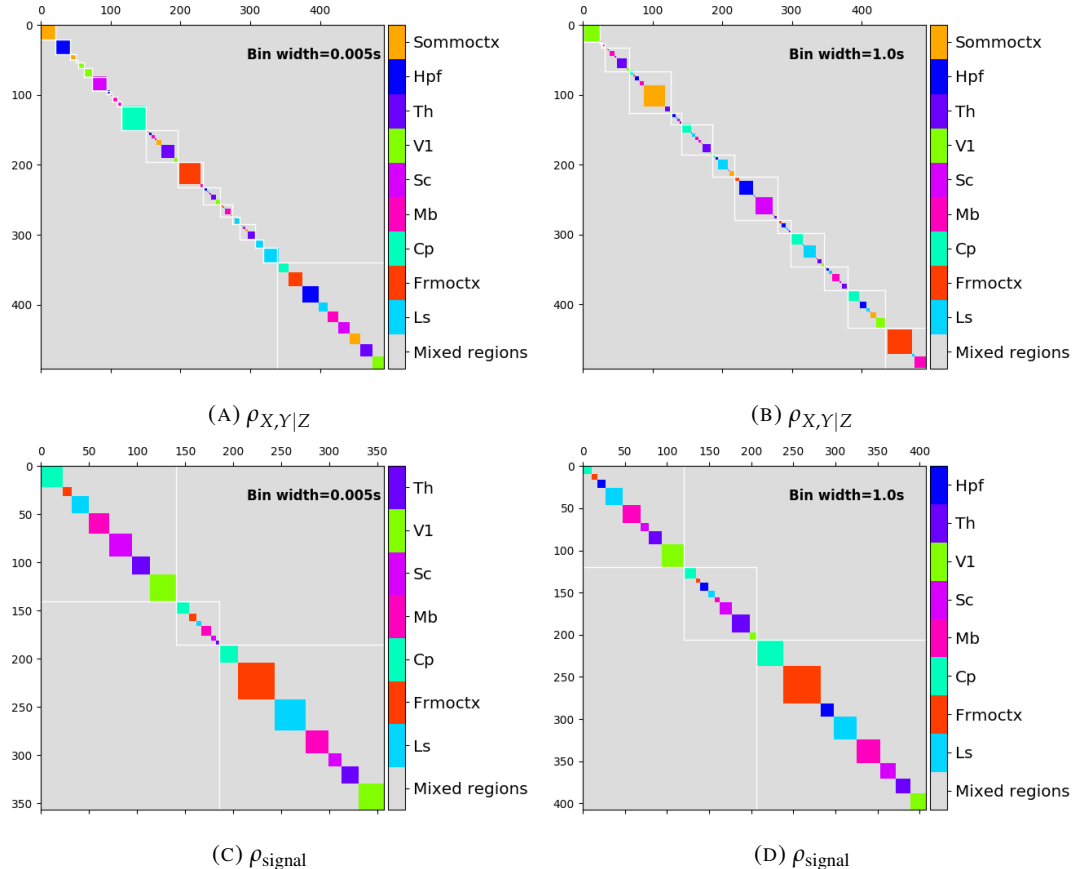


FIGURE 3.11: Matrices showing the regional membership of pairs by colour, and the communities in which those pairs lie. (A-B) Detected communities and regional membership matrix for network based on rectified spike count correlation $\rho_{X,Y|Z}$, using time bin widths of 0.005s and 1s respectively. (C-D) Detected communities and regional membership matrix for network based on rectified signal correlation ρ_{signal} , using time bin widths of 0.005s and 1s respectively.

1320 We saw a consistent increase in $\rho_{X,Y|Z}$ as the time bin width increased, this corresponds to
 1321 the result for $E[\text{cov}(X, Y|Z)]$. We observed different trends for ρ_{signal} for each mouse, this
 1322 corresponds to the result for $\text{cov}(E[X|Z], E[Y|Z])$.

1323 We applied our network noise rejection and community detection process to networks
 1324 based on the spike count correlations $\rho_{X,Y|Z}$ and the signal correlations ρ_{signal} . We noted that
 1325 the community detection on $\rho_{X,Y|Z}$ behaved similarly to the community detection on the total
 1326 correlation. We can see this in figures 3.11a and 3.11b. At very short time bin widths, we
 1327 detect more communities, and those communities often contain cells from one brain region
 1328 only. At longer time bin widths, we detect fewer communities, and those communities tend
 1329 to contain cells from multiple brain regions. When we examine the distance between (or
 1330 similarity between) the anatomical division of the cells, and the detected communities we
 1331 notice that the two clusterings are more similar at shorter time bin widths (see figure 3.12).

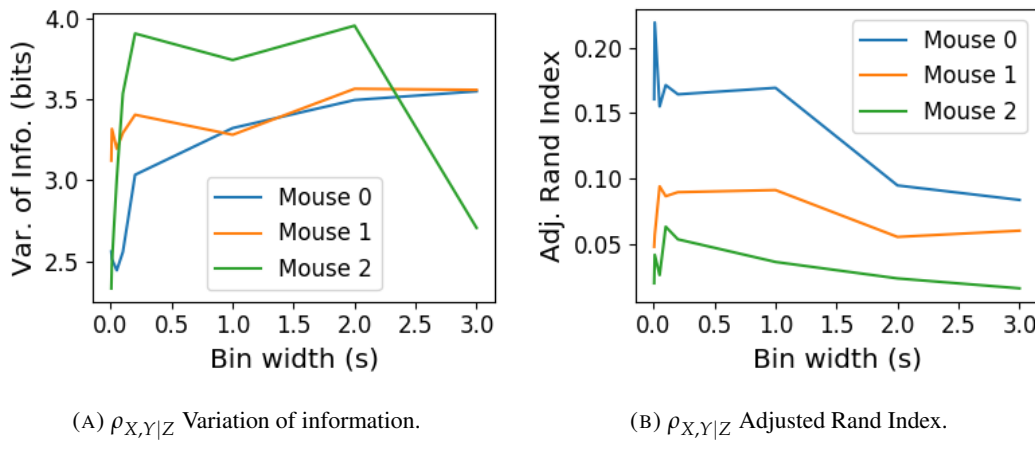
(A) $\rho_{X,Y|Z}$ Variation of information.(B) $\rho_{X,Y|Z}$ Adjusted Rand Index.

FIGURE 3.12: Distance and similarity measures between the anatomical division of the neurons, and the communities detected in the network based on the spike count correlations $\rho_{X,Y|Z}$. (A) The variation of information is a ‘distance’ measure between clusterings. The distance between the anatomical ‘clustering’ and the community clustering increases as the time bin width increases. (B) The adjusted Rand index is a similarity measure between clusterings. The detected communities become less similar to the anatomical division of the cells as the time bin width increases.

1332 When we applied the network noise rejection and community detection process to the
 1333 networks based on the signal correlations ρ_{signal} we found the number of communities we
 1334 detected reduced with increasing time bin width. But the number of communities detected
 1335 was less than that for the total correlations or the spike count correlations. The communi-
 1336 ties detected always tended to contain cells from multiple regions at both short and long
 1337 timescales (see figures 3.11c and 3.11d). The communities detected bore very little relation
 1338 to the anatomical division of the cells. The adjusted Rand index between the community

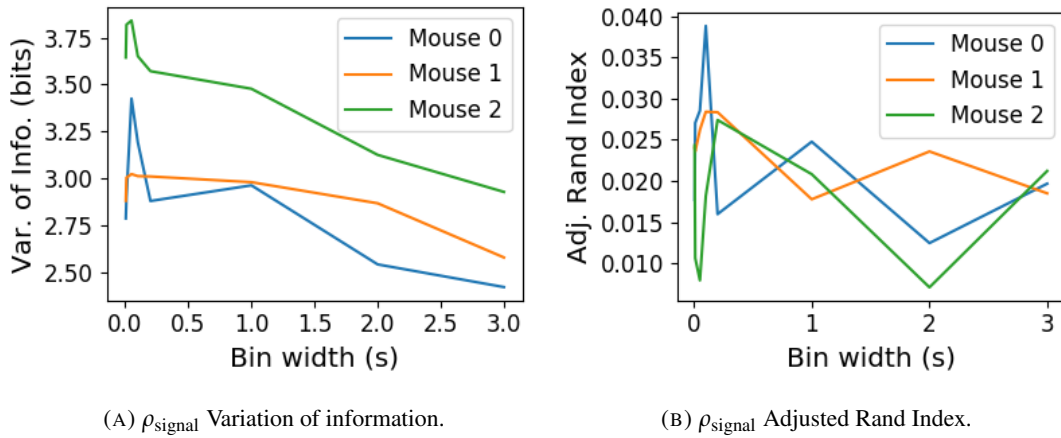
(A) ρ_{signal} Variation of information.(B) ρ_{signal} Adjusted Rand Index.

FIGURE 3.13: Distance and similarity measures between the anatomical division of the neurons, and the communities detected in the network based on the signal correlations ρ_{signal} . (A) The variation of information is a ‘distance’ measure between clusterings. The distance between the anatomical ‘clustering’ and the community clustering increases as the time bin width increases. (B) The adjusted Rand index is a similarity measure between clusterings. The detected communities become less similar to the anatomical division of the time bin width increases.

1339 clustering and the anatomical ‘clustering’ is close to zero for every time bin width (see figure
 1340 3.13b). This indicates that the similarity between the clusterings is close to chance. We did
 1341 observe a slight downward trend in the variation of information with increasing bin width
 1342 (see figure 3.13a), but this is more likely due to a decrease in the number of communities
 1343 detected rather than any relationship with anatomy.

1344 We also observed that the network noise rejection process rejected some of the cells
 1345 when applied to the network based on the signal correlations. This means that those cells
 1346 did not contribute to the additional structure of the network beyond that captured by the
 1347 sparse weighted configuration model. This is why the matrices in figures 3.11c and 3.11d are
 1348 smaller than their analogues in figures 3.11a and 3.11b.

1349 3.2.8 Absolute correlations and negative rectified correlations

1350 At the moment, the network noise rejection protocol can only be applied to weighted undi-
 1351 rected graphs with non-negative weights. This meant that we had to rectify our correlated
 1352 networks before applying the network noise rejection and community detection process. We
 1353 wanted to investigate what would happen if instead of rectifying the correlations, we used the
 1354 absolute value, or reversed the signs of the correlations and then rectified.

1355 When we used the absolute value of the correlations, we found very similar results to

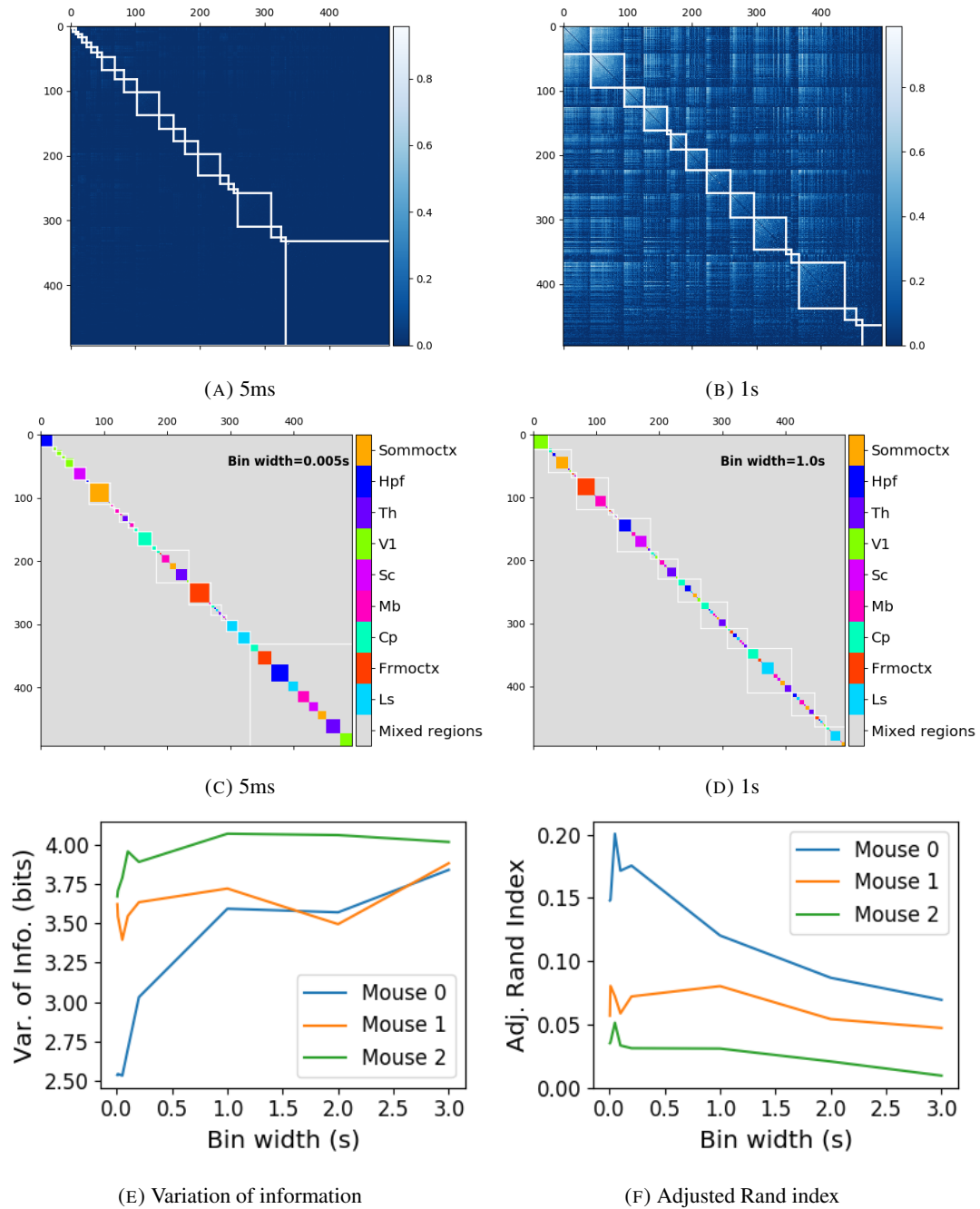


FIGURE 3.14: (A-B) Absolute correlation matrices with detected communities indicated by white lines. These communities are based on the absolute value of the total correlation between each pair of cells. Those entries within a white square indicate that both of those neurons are in the same community. Matrices shown are for 5ms and 1s time bin widths respectively. Main diagonal entries were set to 0. (C-D) Matrices showing the anatomical distribution of pairs along with their community membership. Regional membership is indicated by the colour bar. (E) Variation of information between the anatomical division of the cells, and the detected communities. (F) Adjusted Rand index between the anatomical division, and the detected communities.

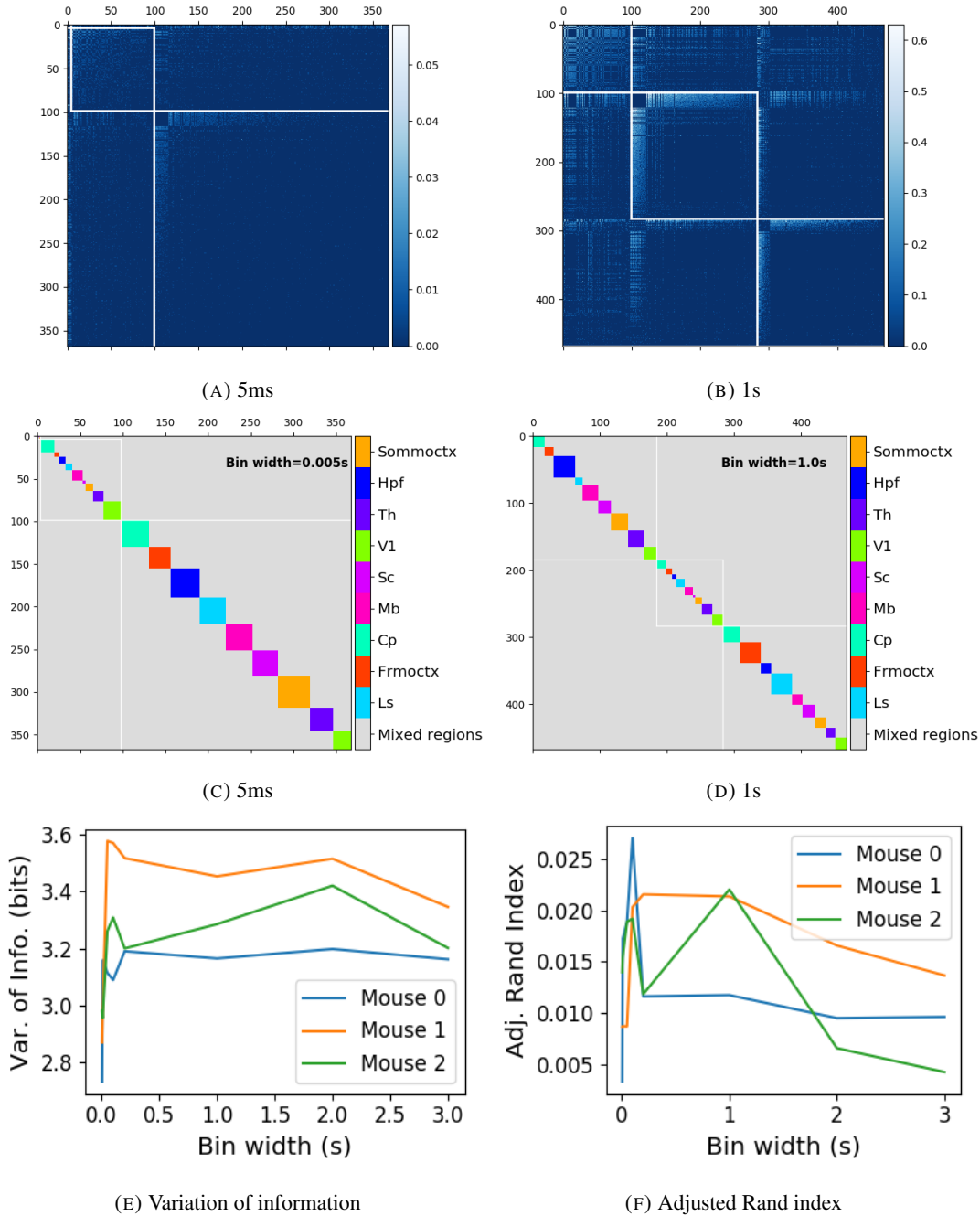


FIGURE 3.15: (A-B) Sign reversed rectified correlation matrices with detected communities indicated by white lines. Those entries within a white square indicate that both of those neurons are in the same community. Matrices shown are for 5ms and 1s time bin widths respectively. Main diagonal entries were set to 0. (C-D) Matrices showing the anatomical distribution of pairs along with their community membership. Regional membership is indicated by the colour bar. (E) Variation of information between the anatomical division of the cells, and the detected communities. (F) Adjusted Rand index between the anatomical division, and the detected communities.

1356 those shown above for the rectified total correlations and the rectified spike count corre-
1357 lations. We detected more communities using shorter bin widths, and these communities
1358 were more similar to the brain's anatomy than those communities detected using a longer bin
1359 width (see figure 3.14). The only exception being that we detected more communities. This
1360 could indicate that we detected both positively and negatively correlated communities, but
1361 we haven't done any further investigation so we cannot say for sure.

1362 When we used the sign reversed rectified correlated networks, we tended to find fewer
1363 communities. Each community contained cells from many different anatomical regions, at
1364 both long and short bin widths (see figures 3.15a, 3.15b, 3.15c, 3.15d). The communities
1365 bore little relation to the anatomical distribution of the cells, this can be seen in figure 3.15f,
1366 the values close to zero indicate that the similarity between the two clusterings are around
1367 chance level. This indicates that there was not much structure in the negatively correlated
1368 networks beyond that captured by the sparse weighted configuration model.

1369 3.3 Discussion

1370 It is well established that the brain uses correlated behaviour in neuronal ensembles to repre-
1371 sent the information taken in through sensation (Cohen and Maunsell, 2009; Litwin-Kumar,
1372 Chacron, and Doiron, 2012; deCharms and Merzenich, 1996). However, most studies that
1373 examine the nature of these correlations in-vivo, study an ensemble of cells from only one or
1374 two brain regions (Cohen and Kohn, 2011; Wierzynski et al., "2009"; Patterson et al., 2014;
1375 Girard, Hupé, and Bullier, 2001). Furthermore, recent results have shown that behaviour can
1376 drive correlated activity in multiple brain regions, including those not normally associated
1377 with motor control (Stringer et al., 2019; Gründemann et al., 2019; Allen et al., 2019). In this
1378 study, we utilised one of the newly recorded large datasets containing electrophysiological
1379 recordings from multiple brain regions simultaneously. We investigated correlated behaviour
1380 in these different brain regions and we investigated correlated behaviour between neurons in
1381 different regions, during spontaneous behaviour.

1382 A number of studies have found that the timescale of correlated behaviour induced by a
1383 stimulus can be modulated by the stimulus structure and behavioural context. For example,
1384 the spike train correlations between cells in weakly electric fish are modulated by the spa-
1385 tial extent of the stimulus (Litwin-Kumar, Chacron, and Doiron, 2012), and neurons in the
1386 marmoset primary auditory cortex modulate their spike timing (and therefore correlation) in
1387 response to stimulus features without modulating their firing rate (deCharms and Merzenich,

1388 1996). Furthermore, the width of the time bins over which spike counts are measured has
1389 been shown to have an effect on the magnitude of those correlations (Cohen and Kohn, 2011).
1390 Despite this, very little research has been done comparing correlation measures from the same
1391 dataset at different timescales. We investigated this by varying the time bin width used to bin
1392 spike times into spike counts from as short as 5ms up to 3s.

1393 In order to further investigate the effect of these correlations at different timescales, we
1394 regarded our neuronal ensemble as a weighted undirected graph, where each neuron is rep-
1395 resented by a node, and the weight on each edge is the correlation between the neurons
1396 connected by that edge. We then applied a novel clustering method from network science
1397 (Humphries et al., 2019) to identify communities in these networks. Communities in a net-
1398 work graph refer to sets of nodes that are more strongly connected to each other than the
1399 nodes outside of their set. Another way to put this is to say that the nodes in a community
1400 are more strongly connected than *expected*. What connection strength might be expected is
1401 defined by a null network model. We chose a null network model that matched the sparsity
1402 and total strength of our correlation based data networks. So, if two cells were in the same
1403 community, those cells were more correlated than would be expected given the correlation
1404 strength of their ensemble.

1405 These networks, and the community detection process, were completely agnostic of the
1406 anatomical division of the cells in our ensemble. When we compared the detected commu-
1407 nities with the anatomical division of the cells using distance and similarity measures for
1408 clusterings, we found that the detected communities were more similar to the anatomical
1409 division at shorter timescales. That is, when we used a wider time bin to count spikes, and
1410 computed pairwise correlations with these spike counts, the correlated communities tended to
1411 exist within anatomical regions at shorter timescales, and tended to span anatomical regions
1412 at longer timescales. This could reflect localised functional correlations at short time scales
1413 rippling outwards across brain regions at longer timescales. The brain may be processing
1414 some information quickly locally, and carrying out further, perhaps more detailed, represen-
1415 tation over a longer timescale across many regions using the representations that were just
1416 built locally.

1417 These changes in communities across timescales could also be driven by the anatomy
1418 of the individual cells. For example, it may simply take longer to transmit action potentials
1419 over longer distances, hence correlated activity over longer timescales will exist between
1420 anatomical regions, rather than within. However, the switch to almost exclusively multi-
1421 regional functional networks at 1s bin widths, rather than a mixture of multi-region, and

single-region suggests that the inter-regional correlations either overpower, or inhibit the local correlations. So there may be more at play than just timescales.

We acknowledged that the region spanning correlated communities that we detected at longer time scales could exist due to collating activity driven by distinct spontaneous activities. In order to account for this, we modelled the spike counts as a linear function of the top 500 principal components of a video of the mouse's face filmed simultaneously with the electrophysiological readings. We applied our network noise rejection and community detection process to the weighted undirected networks formed by the spike count correlations (or noise correlations) and the signal correlations that we calculated using our model. For the spike count correlation networks, we found much the same results as for the total correlations as described above. For the signal correlations, the communities detected in these networks bore little relation to the anatomical division of the cells. Recent findings have shown that behavioural data accounts for correlations in many brain regions that would otherwise be dismissed as noise (Stringer et al., 2019), our finding to shows that these correlations are still governed by the timescale division between local communication and across-region communication.

There is a lot of room for further investigation based on this research. For a start, the data that we used here were collected from nine different regions in the mouse brain, but none of these regions were part of the somatosensory cortex. Given that a mouse experiences so much of its environment through its sense of smell, some data from this region would be interesting to investigate. On the same theme, the mice in the experiment from which the data were collected were headfixed and placed on a rotating ball, but were otherwise behaving spontaneously. Had these mice been exposed to a visual, aural, or olfactory stimulus, we could have examined the responses of the cells in the brain regions corresponding to vision, hearing, and olfaction, and compared these responses to the responses from the other brain regions. Furthermore, we could have investigated the interaction between the sets of responses.

Another space for further investigation is the community detection. The algorithm that we used here never detects overlapping communities. But functional communities could indeed have overlaps. Clustering methods that detect overlapping clusters do exist (Baadel, Thabtah, and Lu, 2016). Applying one of those algorithms could yield some interesting results. Also, the community detection algorithm that we used here cannot process graphs with negative weights, this forced us to separate positive and negative correlations before applying our network noise rejection and community detections process, or use the absolute value of our

1456 correlations. A community detection algorithm that can work on weighted undirected graphs
1457 with negative weights could yield some interesting results here.

1458 **3.4 Data**

1459 The data that we used in this project were collected by Nick Steinmetz and his lab members
1460 (Stringer et al., 2019).

1461 **3.4.1 Brain regions**

1462 Neuropixels probes were used to collect extracellular recordings (Jun et al., 2017) from three
1463 different mice. The mice were awake, headfixed, and engaging in spontaneous behaviour.
1464 The mice were of different sexes and different ages. One mouse was ‘wild-type’, the others
1465 were mutants. Details as follows:

- 1466 1. male, wild type, P73.
- 1467 2. female, TetO-GCaMP6s, Camk2a-tTa, P113
- 1468 3. male, Ai32, Pvalb-Cre, P99

1469 Eight probes were used to collect readings from 2296, 2668, and 1462 cells respectively.

1470 Data were collected from nine brain regions in each mouse:

- 1471 • Caudate Putamen (CP)
- 1472 • Frontal Motor Cortex (Frmoctx)
- 1473 • Hippocampal formation (Hpf)
- 1474 • Lateral Septum (Ls)
- 1475 • Midbrain (Mb)
- 1476 • Superior Colliculus (Sc)
- 1477 • Somatomotor cortex (Sommocctx)
- 1478 • Thalamus (Th)
- 1479 • Primary visual cortex (V1)

1480 Readings were continuous and lasted for about 1 hour (Stringer et al., 2019). Locations of
1481 each of the probes can be seen in figure 3.16.

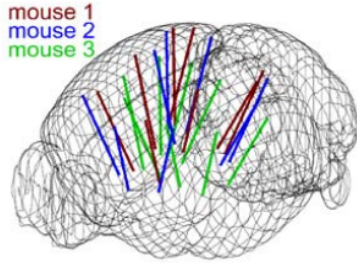


FIGURE 3.16: **Probe Locations:** The locations of the probes in each of the three mouse brains (Stringer et al., 2019).

3.4.2 Video recordings

Video recordings of the mouse's face were taken during the spontaneous behaviour. We had access to the top 500 principle components and top 500 eigenvectors of the processed videos. The frequency of recording was slightly less than 40Hz. Each frame contained 327×561 pixels. These principal components were used as behavioural data. We controlled for these components when taking measurements conditioned on behaviour.

3.5 Methods

3.5.1 Binning data

We transformed the spike timing data into binned spike count data by dividing the experimental period into time bins and counting the spikes fired by each cell within the time period covered by each of those bins. The data were divided into time bins of various widths ranging from 0.01s to 4s.

If the total length of the recording period was not an integer multiple of the time bin width, we cut off the remaining time at the end of the recording period. This period was at most 3.99s. This is far less than the total recording time of around 1 hour. So, this detail would not affect our results.

3.5.2 Correlation coefficients

We calculated Pearson's correlation coefficient for pairs of spike counts from pairs of neurons. For jointly distributed random variables X and Y , Pearson's correlation coefficient is

defined as:

$$\rho_{XY} = \frac{\text{cov}(X, Y)}{\sigma_X \sigma_Y} \quad (3.1)$$

$$= \frac{E[(X - \mu_X)(Y - \mu_Y)]}{\sigma_X \sigma_Y} \quad (3.2)$$

1499 where E denotes the expected value, μ denotes the mean, and σ denotes the standard deviation.
 1500 The correlation coefficient is a normalised measure of the covariance. It can take values
 1501 between 1 (completely correlated) and -1 (completely anti-correlated). Two independent
 1502 variables will have a correlation coefficient of 0. But, having 0 correlation does not imply
 1503 independence.

If we do not know the means and standard deviations required for equation 3.1, but we have samples from X and Y , Pearson's sample correlation coefficient is defined as:

$$r_{XY} = \frac{\sum_{i=1}^n (x_i - \bar{x})(y_i - \bar{y})}{\sqrt{\sum_{i=1}^n (x_i - \bar{x})^2} \sqrt{\sum_{i=1}^n (y_i - \bar{y})^2}} \quad (3.3)$$

1504 where $\{(x_i, y_i)\}$ for $i \in \{1, \dots, n\}$ are the paired samples from X and Y , and $\bar{x} = \frac{1}{n} \sum_{i=1}^n x_i$,
 1505 and $\bar{y} = \frac{1}{n} \sum_{i=1}^n y_i$ are the sample means.

1506 In practice we used the python function `scipy.stats.pearsonr` to calculate the
 1507 correlation coefficients.

1508 Total correlations, r_{SC}

1509 The total correlation (r_{SC}) of two cells is the correlation between the spike counts of those
 1510 cells in response to a given stimulus condition.

1511 Shuffled total correlations

1512 We measured the shuffled total correlations between two neurons by randomly permuting one
 1513 of the neuron's spike counts and measuring the total correlations. These shuffled correlations
 1514 were useful when measuring the effect of time bin width on correlations, and when decid-
 1515 ing which correlations should be preserved when creating correlation networks (see section
 1516 3.5.5).

1517 Separating Correlations & Anti-correlations

1518 In order to compare the effect of bin width on measures of negative r_{SC} (anti-correlation) and
 1519 positive r_{SC} separately, we had to separate correlated and anti-correlated pairs. To do this, we

simply measured the mean r_{SC} , taking the mean across all the bin widths. If this quantity was positive or zero we regarded the pair as positively correlated. If this quantity was negative we regarded the pair as anti-correlated.

3.5.3 Conditioning on behavioural data

Our behavioural data consisted of the top 500 principal components (PCs) of a processed video recording of the mouse's face (see section 3.4.2). Denoting the spike count of a given cell by X , and the PCs by Z_1, \dots, Z_{500} , we wanted to model X as a function of Z_1, \dots, Z_{500} in order to estimate

$$E[X|Z_1, \dots, Z_{500}] = \int_{x \in X} x P(X = x|Z_1, \dots, Z_{500}) dx \quad (3.4)$$

$$= \int_{x \in X} x \frac{P(X = x, Z_1, \dots, Z_{500})}{P(Z_1, \dots, Z_{500})} dx \quad (3.5)$$

Given the 500 components, a naïve estimation of $P(Z_1, \dots, Z_{500})$ or $P(X, Z_1, \dots, Z_{500})$ by histogramming was impossible. Therefore we modelled X as a linear combination of the PCs.

Linear regression

We modelled the spike count of a given cell, X , as a linear combination of the PCs of the video of the mouse's face, $\mathbf{Z} = Z_1, \dots, Z_{500}$. We tried three different types of regularization

- $L1$ or 'Lasso'
 - $L2$ or 'Ridge regression'
 - 'Elastic net' regularisation (a linear combination of both $L1$ and $L2$ regularisation penalties)
- The elastic net regularisation performed the best, so we stuck with that.

Elastic net regularisation

Suppose we wish to model n observations of a random variable X , $\mathbf{x} = (x_1, \dots, x_n)$ using n instances of m predictors $\mathbf{Z} = (Z_1, \dots, Z_m)$. The naïve elastic net criterion is

$$L(\lambda_1, \lambda_2, \boldsymbol{\beta}) = |\mathbf{x} - \mathbf{Z}\boldsymbol{\beta}|^2 + \lambda_2|\boldsymbol{\beta}|_2 + \lambda_1|\boldsymbol{\beta}|_1 \quad (3.6)$$

where

$$|\boldsymbol{\beta}|_2 = \sum_{j=1}^m \beta_j^2 \quad (3.7)$$

$$|\boldsymbol{\beta}|_1 = \sum_{j=1}^m |\beta_j| \quad (3.8)$$

The naïve elastic net estimator $\hat{\boldsymbol{\beta}}$ is the minimiser of the system of equations 3.6 (Zou and Hastie, 2005)

$$\hat{\boldsymbol{\beta}} = \arg \min_{\boldsymbol{\beta}} L(\lambda_1, \lambda_2, \boldsymbol{\beta}) \quad (3.9)$$

1536 We implemented the model using the `ElasticNetCV` method of Python's
 1537 `sklearn.linear_models` package.

1538 As well as using the PCs, we also tried fitting the models using the raw video data recon-
 1539 structed from the PCs and eigenvectors. These models performed worse than those using the
 1540 PCs. We expected this because each representation contains the same amount of information,
 1541 but the raw video representation spreads this information across many more components.
 1542 This requires more parameter fitting, but given the same information.

1543 **Conditional covariance**

We calculated the expected value of the conditional covariance using the law of total covari-
 ance.

$$\text{cov}(X, Y) = E[\text{cov}(X, Y|Z)] + \text{cov}(E[X|Z], E[Y|Z]) \quad (3.10)$$

1544 where these expected values are calculated with respect to the distribution of Z as a random
 1545 variable.

1546 The law of total covariance breaks the covariance into two components. The first com-
 1547 ponent $E[\text{cov}(X, Y|Z)]$ is the expected value, under the distribution of Z , of the conditional
 1548 covariance $\text{cov}(X, Y|Z)$. This covariance could be interpreted as the unnormalised version
 1549 of what Cohen et al. (2011) call the spike count correlation (Cohen and Kohn, 2011), aka.
 1550 the noise correlation. In particular, this is the covariance of the spike counts in response to
 1551 repeated presentation of identical stimuli.

1552 The second component is analogous to what Cohn et al. (2011) call the *signal correlation*
 1553 (Cohen and Kohn, 2011). In particular, $\text{cov}(E[X|Z], E[Y|Z])$ is the covariance between

1554 spike counts in response to different stimuli.

Using our linear model, we calculated $E[X|Z_1, \dots, Z_{500}]$ for each cell X. Then we proceeded to calculate

$$E[\text{cov}(X, Y|Z_1, \dots, Z_{500})] = \text{cov}(X, Y) - \quad (3.11)$$

$$\text{cov}(E[X|Z_1, \dots, Z_{500}], E[Y|Z_1, \dots, Z_{500}]) \quad (3.12)$$

1555 **Measures of conditional correlation**

As a measure of expected correlation, we measured the ‘event conditional correlation’ (Maugis, 2014)

$$\rho_{XY|Z} = \frac{E[\text{cov}(X, Y|Z)]}{\sqrt{E[\text{var}(X|Z)]}E[\text{var}(Y|Z)]} \quad (3.13)$$

1556 Although this is not an actual correlation, it is an intuitive analogue to the correlation as a
1557 normalised version of the covariance.

For comparison, we also measured the ‘signal correlation’

$$\rho_{\text{signal}} = \frac{\text{cov}(E[X|Z], E[Y|Z])}{\sqrt{\text{var}(E[X|Z])}\sqrt{\text{var}(E[Y|Z])}} \quad (3.14)$$

1558 this is an actual correlation.

1559 **3.5.4 Information Theory**

1560 **Entropy $H(X)$**

The entropy of a random variable X, with outcomes x_1, \dots, x_N , and corresponding probabilities p_1, \dots, p_N is defined as

$$H(X) = - \sum_{n=1}^N p_n \log_2 p_n \quad (3.15)$$

1561 This quantity is also known as the information entropy or the ‘surprise’. It measures the
1562 amount of uncertainty in a random variable. For example, a variable with a probability of 1
1563 for one outcome, and 0 for all other outcomes will have 0 bits entropy, because it contains no
1564 uncertainty. But a variable with a uniform distribution will have maximal entropy as it is the
1565 least predictable. This quantity is analogous to the entropy of a physical system (Shannon,

1566 1948). Note that any base may be used for the logarithm in equation 3.15, but using base 2
 1567 means that the quantity will be measured in ‘bits’.

The joint entropy of two jointly distributed random variables X and Y , where Y has outcomes y_1, \dots, y_M , is defined as

$$H(X, Y) = - \sum_{n=1}^N \sum_{m=1}^M P(X = x_n, Y = y_m) \log_2 P(X = x_n, Y = y_m) \quad (3.16)$$

1568 If X and Y are independent then $H(X, Y) = H(X) + H(Y)$. Otherwise $H(X, Y) <$
 1569 $H(X) + H(Y)$. When X and Y are completely dependent $H(X, Y) = H(X) = H(Y)$.

The conditional entropy of Y conditioned on X is defined as

$$H(Y|X) = - \sum_{n=1}^N \sum_{m=1}^M P(X = x_n, Y = y_m) \log_2 \frac{P(X = x_n, Y = y_m)}{P(X = x_n)} \quad (3.17)$$

1570 When X and Y are independent $H(Y|X) = H(Y)$. Intuitively, we learn nothing of Y by
 1571 knowing X , so Y is equally uncertain whether we know X or not. If Y is totally dependent
 1572 on X , then the fraction in the logarithm is 1, which gives $H(Y|X) = 0$.

1573 These entropy measures are the basis of the mutual information measure.

1574 Maximum entropy limit

When spiking data is binned into spike counts there is an upper limit on the entropy of these data. The maximum entropy discrete distribution is the discrete uniform distribution. A random variable with this distribution will take values from some finite set with equal probabilities. Binned spike count data will take values between 0 and some maximum observed spike count n_{\max} . A neuron with responses that maximises entropy will take these values with equal probability, i.e. if $i \in \{0, \dots, n_{\max}\}$ then $P(X = i) = \frac{1}{n_{\max}+1}$. The entropy of this neuron will be

$$\begin{aligned} H(X) &= - \sum_{i=0}^{n_{\max}} P(X = i) \log_2 P(X = i) \\ &= - \sum_{i=0}^{n_{\max}} \frac{1}{n_{\max}+1} \log_2 \left(\frac{1}{n_{\max}+1} \right) \\ &= - \log_2 \left(\frac{1}{n_{\max}+1} \right) \\ &= \log_2 (n_{\max} + 1) \end{aligned}$$

1575 Therefore, the maximum entropy of the binned spike counts of a neuron is $\log_2(n_{\max} + 1)$.
 1576 Of course, it would be very unusual for a neuron to fire in accordance with the discrete
 1577 uniform distribution. Most measurements of entropy taken on binned spiking data will be
 1578 much lower than the maximum. See figure 3.17 to see the maximum entropy as a function of
 1579 the maximum observed spike count.

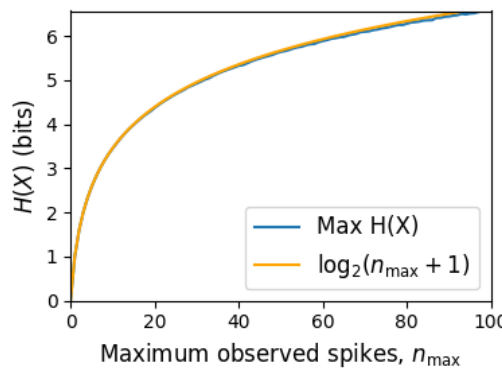


FIGURE 3.17: **Entropy Limit:** The upper limit on entropy of binned spike count data as a function of the maximum observed spike count. The orange line is the analytical maximum. The blue line is the entropy of samples with $N = 1000$ data points taken from the discrete uniform distribution.

1580 **Mutual Information $I(X; Y)$**

1581 The mutual information can be defined mathematically in a number of ways, all of which are
 1582 equivalent. These definitions illustrate the different ways of interpreting the mutual informa-
 1583 tion.

For two jointly distributed random variables X and Y , the mutual information $I(X; Y)$ is defined as

$$I(X; Y) = H(Y) - H(Y|X) \quad (3.18)$$

$$= H(X) - H(X|Y) \quad (3.19)$$

1584 Equation 3.18 fits with the following intuition: The mutual information between X and Y is
 1585 the reduction in uncertainty about X gained by knowing Y , or vice versa. We could also say
 1586 the mutual information is the amount of information gained about X by knowing Y , or vice
 1587 versa.

Another useful entropy based definition for the mutual information is

$$I(X; Y) = H(X) + H(Y) - H(X, Y) \quad (3.20)$$

1588 This definition is useful because it does not require the calculation of conditional probabilities.
 1589

The mutual information can also be defined in terms of marginal, joint, and conditional distributions. For example,

$$I(X;Y) = - \sum_{n=1}^N \sum_{m=1}^M P(X = x_n, Y = y_m) \log_2 \frac{P(X = x_n, Y = y_m)}{P(X = x_n)P(Y = y_m)} \quad (3.21)$$

Notice that this can be rewritten as a Kullback–Leibler divergence.

$$I(X;Y) = D_{KL}(P(X,Y) || P(X)P(Y)) \quad (3.22)$$

1590 So, we can also think of the mutual information as a measure of the difference between
 1591 the joint distribution of X and Y , and the product of their marginal distributions. Since the
 1592 product of the marginal distributions is the joint distribution for independent variables, we
 1593 can think of the mutual information as a measure of the variables' dependence on one another.

1594 The minimum value that $I(X;Y)$ can take is 0. This occurs when the random variables
 1595 X and Y are independent. Then we have $H(X|Y) = H(X)$, and $H(Y|X) = H(Y)$, which
 1596 according to equation 3.18, gives $I(X;Y) = 0$. We also have that $H(X,Y) = H(X) +$
 1597 $H(Y)$ in this case, which according equation 3.20, gives $I(X;Y) = 0$. Finally, we also have
 1598 $P(X,Y) = P(X)P(Y)$, which leaves us with 1 in the argument for the logarithm in equation
 1599 3.21, which again gives $I(X;Y) = 0$.

1600 The mutual information reaches its maximum value when one of the variables X and
 1601 Y is completely determined by knowing the value of the other. In that case $I(X;Y) =$
 1602 $\min\{H(X), H(Y)\}$.

1603 Variation of Information $VI(X,Y)$

The variation of information is another information theoretical quantity based on the mutual information. It is defined as

$$VI(X;Y) = H(X) + H(Y) - 2I(X;Y) \quad (3.23)$$

We can rewrite this as the summation of two positive quantities

$$VI(X;Y) = [H(X) - I(X;Y)] + [H(Y) - I(X;Y)] \quad (3.24)$$

1604 In English, the variation of information is the summation of the uncertainty in the random
1605 variables X and Y excluding the uncertainty shared by those variables.

1606 This measure will become more relevant when we go on to talk about clusterings because
1607 $VI(X; Y)$ forms a metric on the space of clusterings.

1608 **Measuring entropies & mutual information**

1609 In practice, we measured the mutual information between spike counts using Python and the
1610 python package `pyitlib`. We used the PT-bias correction technique to estimate the bias of
1611 our measurements when measuring the mutual information between the spike counts of two
1612 cells (Treves and Panzeri, 1995).

1613 When measuring the mutual information between clusterings we used Python, but we
1614 used the `mutual_info_score`, `adjusted_mutual_info_score`, and
1615 `normalized_mutual_info_score` functions from the `sklearn.metrics` part of
1616 the `sklearn` package.

1617 **3.5.5 Network analysis**

1618 **Correlation networks**

1619 In order to analyse functional networks created by the neurons in our ensemble, we mea-
1620 sured the total correlation between each pair of neurons. These measurements induced an
1621 undirected weighted graph/network between the neurons. The weight of each connection
1622 was equal to the total correlation between each pair of neurons.

1623 We followed the same procedure for total correlations 3.5.2, spike count correlations, and
1624 signal correlations 3.5.3.

1625 **Rectified correlations**

1626 At the time of writing, the community detection method outlined in (Humphries et al., 2019)
1627 could only be applied to networks with positively weighted connections. But many neuron
1628 pairs were negatively correlated. To apply the community detection method, we *rectified* the
1629 network, by setting all the negative weights to zero.

1630 We also looked for structure in the network created by negative correlations by reversing
1631 the signs of the correlations, and rectifying these correlations before applying our network
1632 analysis.

1633 Finally, we used the absolute value of the correlations as the weights for the graph/network.
1634 By doing this, we hoped to identify both correlated and anti-correlated functional communi-
1635 ties of neurons.

1636 **Sparsifying data networks**

1637 When creating our correlation networks, we wanted to exclude any correlations that could
1638 be judged to exist ‘by chance’. To do this, we measured the 5th and 95th percentile of
1639 the shuffled correlations (see section 3.5.2) for the given mouse and time bin width. We
1640 then set all the data correlations between these two values to 0. This excluded any ‘chance’
1641 correlations from our network, and created a sparser network. This allowed us to make use
1642 of the ‘sparse weighted configuration model’ as described in section 3.5.5.

1643 **Communities**

1644 Given some network represented by an adjacency matrix \mathbf{A} , a community within that net-
1645 work is defined as a collection of nodes where the number of connections within these nodes
1646 is higher than the expected number of connections between these nodes. In order to quan-
1647 tify the ‘expected’ number of connections, we need a model of expected networks. This is
1648 analogous to a ‘null model’ in traditional hypothesis testing. We test the hypothesis that our
1649 data network departs from the null network model to a statistically significant degree. For
1650 undirected unweighted networks, the canonical model of a null network is the configuration
1651 model (Fosdick et al., 2016). Since we are working with weighted sparse networks, we used
1652 more suitable null models, described below.

1653 **Weighted configuration model**

1654 The *weighted configuration model* is a canonical null network model for weighted networks.
1655 Given some data network, the weighted configuration model null network will preserve the
1656 degree sequence and weight sequence of each node in the data network. But the edges will
1657 be distributed randomly (Fosdick et al., 2016). Any structure in the data network beyond
1658 its degree sequence and weight sequence will not be captured in the weighted configuration
1659 model. So, this model can be used in testing the hypothesis that this extra structure exists.

1660 **Sparse weighted configuration model**

1661 The *sparse weighted configuration model* is another null network model. Similar in nature to
1662 the weighted configuration model (see section 3.5.5), but the sparsity of the data network is

1663 preserved in the null network. This is achieved by sampling from a probability distribution
 1664 for the creation or non-creation of each possible connection, then distributing the weight of
 1665 the data network randomly in this sparse network (Humphries et al., 2019). This is the null
 1666 network that we used when searching for additional structure in our data networks.

1667 **Spectral rejection**

1668 We made use of the spectral rejection algorithm as outlined in (Humphries et al., 2019). The
 1669 spectral rejection algorithm is a method for finding structure in a network not captured by a
 1670 supposed null model, if such structure exists.

To describe the method, we denote our data network matrix \mathbf{W} , we denote the expected network of our null network model as $\langle \mathbf{P} \rangle$. Then the departure of our data network from the null network can be described by the matrix

$$\mathbf{B} = \mathbf{W} - \langle \mathbf{P} \rangle \quad (3.25)$$

1671 a common choice for $\langle \mathbf{P} \rangle$ in community detection is the ‘configuration model’ (Fosdick et
 1672 al., 2016; Humphries, 2011). The matrix \mathbf{B} is often called the configuration matrix, in this
 1673 context we will use the term ‘deviation matrix’ as it captures the deviation of \mathbf{W} from the
 1674 null model.

1675 To test for structure in the network represented by \mathbf{W} , we examine the eigenspectrum of \mathbf{B}
 1676 and compare it to the eigenspectrum of our null model. Firstly, note that since our data model
 1677 doesn’t allow self loops, and is not directed, the matrix representing the network will be
 1678 symmetric and positive semi-definite, and will therefore be invertible with real eigenvalues.
 1679 We selected a null model with the same characteristics.

1680 To find the eigenspectrum of the null model, we generated N samples from our null
 1681 model P_1, \dots, P_N , and we measured their deviation matrices B_1, \dots, B_N . We then calculated
 1682 the eigenspectrum of each of those samples. We calculated the upper bound of the null model
 1683 eigenspectrum by taking the mean of the largest eigenvalues of B_1, \dots, B_N . We calculated a
 1684 lower bound on the null model eigenspectrum by taking the mean of the smallest eigenvalues
 1685 of B_1, \dots, B_N .

1686 We then calculated the eigenspectrum of \mathbf{B} , our data network deviation matrix. If any of
 1687 those eigenvalues lay outside of the upper or lower bounds of the null model eigenspectrum,
 1688 this is evidence of additional structure not captured by the null model. If we chose the sparse
 1689 weighted configuration model (see section 3.5.5) as our null network model, then eigenvalues

1690 lying below the lower bound indicate k -partite structure in the network. For example, if one
1691 eigenvalue lay below the lower bound, this would indicate some bipartite structure in the data
1692 network. If any eigenvalues lay above the upper bound of the null model eigenspectrum, this
1693 is evidence of community structure in the data network. For example, one eigenvalue of \mathbf{B}
1694 lying above the upper bound of the null model eigenspectrum indicates the presence of two
1695 communities in the network (Humphries, 2011).

1696 **Node rejection**

1697 If there are d data eigenvalues lying outside of the null network eigenspectrum, the d eigen-
1698 vectors corresponding to these eigenvalues will form a vector space. If we project the nodes
1699 of our network into this vector space, by projecting either rows or columns of the data ma-
1700 trix, we can see how strongly each node contributes to the vector space. Nodes that contribute
1701 strongly to the additional structure will project far away from the origin, nodes that do not
1702 contribute to the additional structure will project close to the origin. We want to use this
1703 information to discard those nodes that do not contribute.

1704 We can test whether a node projects *far* away from the origin or *close* to the origin
1705 using the eigenvalues and eigenvectors of B_1, \dots, B_N . The j th eigenvector and eigenvalue
1706 of B_i gives a value for a null network's projection into the j th dimension of the additional
1707 structure vector space. The matrices B_1, \dots, B_N give N projections into that dimension.
1708 These projections are a distribution of the null networks' projections. If the data node's
1709 projection exceeds that of the null network projections this node is judged to project *far* from
1710 the origin, and therefore contribute to the additional structure. Otherwise, the node is judged
1711 to project *close* to the origin, and is therefore rejected (Humphries et al., 2019).

1712 **Community detection**

1713 Another application for this d dimensional space is community detection. We first project
1714 all of the nodes into this d -dimensional space, then perform the clustering in this space. The
1715 clustering and community detection procedure is described in (Humphries, 2011).

1716 In practice, the procedure is carried out n times (we chose $n = 100$ times), this returns n
1717 clusterings. We resolve these n clusterings to one final clustering using *consensus clustering*.
1718 We used the consensus clustering method that uses an explicit null model for the consensus
1719 matrix, as outlined in (Humphries et al., 2019).

3.5.6 Clustering Comparison

A clustering \mathcal{C} is a partition of a set D into sets C_1, C_2, \dots, C_K , called clusters, that satisfy the following for all $k, l \in \{1, \dots, K\}$:

$$C_k \cap C_l = \emptyset \quad (3.26)$$

$$\bigcup_{k=1}^K C_k = D \quad (3.27)$$

If we consider two clusterings, \mathcal{C} with clusters C_1, C_2, \dots, C_K and \mathcal{C}' with clusters C'_1, C'_2, \dots, C'_K . There are a number of measurements we can use to compare \mathcal{C} and \mathcal{C}' . In the following, the number of elements in D is denoted by n , and the number of elements in cluster C_k is n_k .

Adjusted Rand Index

The *adjusted Rand Index* is a normalised similarity measure for clusterings based on pair counting.

If we consider the clusterings \mathcal{C} and \mathcal{C}' , and denote

- the number of pairs in the same cluster in \mathcal{C} and \mathcal{C}' by N_{11}

- the number of pairs in different clusters in \mathcal{C} and \mathcal{C}' by N_{00}

- the number of pairs in the same cluster in \mathcal{C} and different clusters in \mathcal{C}' by N_{10}

- the number of pairs in different clusters in \mathcal{C} and the same cluster in \mathcal{C}' by N_{01}

then the *Rand Index* is defined as

$$RI = \frac{N_{11} + N_{00}}{N_{11} + N_{00} + N_{10} + N_{01}} = \frac{N_{11} + N_{00}}{\binom{n}{2}} \quad (3.28)$$

The Rand Index is 1 when the clusterings are identical, and 0 when the clusterings are completely different.

The *adjusted Rand Index* intends on correcting the Rand Index for chance matching pairs.

This is defined as

$$ARI = \frac{2(N_{00}N_{11} - N_{01}N_{10})}{(N_{00} + N_{01})(N_{01} + N_{11}) + (N_{00} + N_{10})(N_{10} + N_{11})} \quad (3.29)$$

The adjusted Rand Index is 1 when the clusterings are identical, and 0 when the Rand Index is equal to its expected value.

1737 **Clusterings as random variables**

If we take any random element of D , the probability that this element is in cluster C_k of clustering \mathcal{C} is

$$P(K = k) = \frac{n_k}{n} \quad (3.30)$$

1738 this defines a probability distribution, which makes the clustering a random variable. Any
1739 clustering can be considered as a random variable this way.

This means that we can measure any of the information theoretic quantities defined in section 3.5.4 with respect to clusterings. For example, the entropy of a clustering is

$$H(\mathcal{C}) = - \sum_{k=1}^K \frac{n_k}{n} \log \frac{n_k}{n} \quad (3.31)$$

If we have two clusterings, the joint probability distribution of these clusterings is defined as

$$P(K = k, K' = k') = \frac{|C_k \cap C'_{k'}|}{n} \quad (3.32)$$

1740 The joint distribution allows us to define the mutual information between two clusterings,
1741 $I(\mathcal{C}; \mathcal{C}')$ (Meilă, 2007).

1742 **Information based similarity measures**

The mutual information between two clusterings is a similarity measure, with $I(\mathcal{C}; \mathcal{C}') = 0$ if \mathcal{C} and \mathcal{C}' are completely different, and $I(\mathcal{C}; \mathcal{C}') = H(\mathcal{C}) = H(\mathcal{C}')$ if \mathcal{C} and \mathcal{C}' are identical. This can be normalised in a number of different ways to make more similarity measures (Vinh, Epps, and Bailey, 2010)

$$NMI_{joint} = \frac{I(\mathcal{C}; \mathcal{C}')}{H(\mathcal{C}, \mathcal{C}')} \quad (3.33)$$

$$NMI_{max} = \frac{I(\mathcal{C}; \mathcal{C}')}{\max\{H(\mathcal{C}), H(\mathcal{C}')\}} \quad (3.34)$$

$$NMI_{sum} = \frac{2I(\mathcal{C}; \mathcal{C}')}{H(\mathcal{C}) + H(\mathcal{C}')} \quad (3.35)$$

$$NMI_{sqrt} = \frac{I(\mathcal{C}; \mathcal{C}')}{\sqrt{H(\mathcal{C})H(\mathcal{C}')}} \quad (3.36)$$

$$NMI_{min} = \frac{I(\mathcal{C}; \mathcal{C}')}{\min\{H(\mathcal{C}), H(\mathcal{C}')\}} \quad (3.37)$$

We can control for chance similarities between the two clusterings by measuring the *adjusted mutual information* between the clusterings. This is defined as

$$AMI_{sum} = \frac{I(\mathcal{C}; \mathcal{C}') - E\{I(\mathcal{C}; \mathcal{C}')\}}{\frac{1}{2}[H(\mathcal{C}) + H(\mathcal{C}')] - E\{I(\mathcal{C}; \mathcal{C}')\}} \quad (3.38)$$

1743 The first term in the denominator, taking the average of the marginal entropies, can be re-
1744 placed by taking the maximum, minimum, or the geometric mean (Vinh, Epps, and Bailey,
1745 2010).

1746 Information based metrics

The variation of information between two clusterings $VI(\mathcal{C}; \mathcal{C}')$ (see section 3.5.4) is a metric on the space of clusterings (Meilă, 2007). That is,

$$VI(\mathcal{C}; \mathcal{C}') \geq 0 \quad (3.39)$$

$$VI(\mathcal{C}; \mathcal{C}') = 0 \iff \mathcal{C} = \mathcal{C}' \quad (3.40)$$

$$VI(\mathcal{C}; \mathcal{C}') = VI(\mathcal{C}'; \mathcal{C}) \quad (3.41)$$

$$VI(\mathcal{C}; \mathcal{C}'') \leq VI(\mathcal{C}; \mathcal{C}') + VI(\mathcal{C}'; \mathcal{C}'') \quad (3.42)$$

Another metric is the *information distance* (Vinh, Epps, and Bailey, 2010)

$$D_{max} = \max\{H(\mathcal{C}), H(\mathcal{C}')\} - I(\mathcal{C}; \mathcal{C}') \quad (3.43)$$

Both of these can be normalised

$$NVI(\mathcal{C}; \mathcal{C}') = 1 - \frac{I(\mathcal{C}; \mathcal{C}')}{H(\mathcal{C}, \mathcal{C}')} \quad (3.44)$$

$$d_{max} = 1 - \frac{I(\mathcal{C}; \mathcal{C}')}{\max\{H(\mathcal{C}), H(\mathcal{C}')\}} \quad (3.45)$$

1747 Comparing detected communities and anatomical divisions

1748 In order to quantify the difference or similarity between the communities detected in our cor-
1749 relation network and the anatomical classification of the cells in that network, we considered
1750 the communities and the anatomical regions as clusters in two different clusterings, \mathcal{C}_{comm}
1751 and \mathcal{C}_{anat} , respectively. We then measured the similarity between the clusterings using the
1752 mutual information, the adjusted mutual information, and the normalised mutual informa-
1753 tion. We measured the difference between, or the distance between, the clusterings using the

1754 variation of information, the normalised variation of information, and the normalised infor-
1755 mation distance. We also measured the difference between the clusterings using the adjusted
1756 Rand Index, just to use a non-information based measure.

1757 We took all of these measures for communities detected using different time bin widths.
1758 This gave us an idea of the effect of time bin width on correlation networks in neural ensem-
1759 bles relative to anatomical regions within those ensembles.

1760 **Chapter 4**

1761 **A simple two parameter distribution
1762 for modelling neuronal activity and
1763 capturing neuronal association**

1764 *Abstract*

1765 Recent developments in electrophysiological technology have lead to an increase in the size
1766 of electrophysiology datasets. Consequently, there is a requirement for new analysis tech-
1767 niques that can make use of these new datasets, while remaining easy to use in practice. In
1768 this work, we fit some one or two parameter probability distributions to spiking data collected
1769 from a mouse exposed to visual stimuli. We show that the Conway-Maxwell-binomial dis-
1770 tribution is a suitable model for the number of active neurons in a neuronal ensemble at any
1771 given moment. This distribution fits these data better than binomial or beta-binomial distribu-
1772 tions. It also captures the correlated activity in the primary visual cortex induced by stimulus
1773 onset more effectively than simply measuring the correlations, at short timescales (< 10ms).
1774 We also replicate the finding of Churchland et al (2010) relating to stimulus onset quenching
1775 neural variability in cortical areas, and we show a correspondence between this quenching
1776 and changes in one of the parameters of the fitted Conway-Maxwell-binomial distributions.

1777 4.1 Introduction

1778 Recent advances in electrophysiological technology, such as ‘Neuropixels’ probes (Jun et al.,
1779 2017) have allowed extracellular voltage measurements to be collected from larger numbers
1780 of cells than traditional methods, in multiple brain regions simultaneously, and routinely.
1781 These larger datasets require innovative methods to extract information from the data in a
1782 reasonable amount of time, ‘reasonable’ being subjective in this case.

1783 Theoretically, all the information at any given moment in an electrophysiological dataset
1784 with n neurons could be captured by calculating the probability distribution for every possi-
1785 ble spiking pattern. This would require defining a random variable with 2^n possible values, a
1786 task that quickly becomes impossible as n increases. Attempts at approximating this random
1787 variable often involve measuring pairwise or higher order correlations (Schneidman et al.,
1788 2006; Flach, 2013; Ganmor, Segev, and Schneidman, 2011). But pairwise correlations may
1789 not be enough to characterise instantaneous neural activity (Tkačik et al., 2014). Further-
1790 more, these kinds of models tend to ignore the temporal structure of neuronal data, in favour
1791 of smaller model size, and scalability.

1792 Higher order correlations would be helpful here, but defining these correlations can be
1793 tricky, never-mind quantifying them. If we use the interaction parameters arising from the
1794 exponential family model as measures of higher order correlations, measuring these correla-
1795 tions becomes computationally impractical quite quickly also (the number of ‘three neuron
1796 correlations’ to measure scales with $\binom{n}{3}$). In this paper, we dispense with measuring correla-
1797 tions directly, and attempt to characterise correlated behaviour by measuring ‘association’; a
1798 more general concept that includes correlation.

1799 In this work, we examined the ability of simple distributions to model the number of
1800 active (spiking) neurons in a neuronal ensemble at any given timepoint. We compared a
1801 little-known distribution named the Conway-Maxwell-binomial distribution to the binomial
1802 distribution and the beta-binomial distribution. The binomial distribution is a probability dis-
1803 tribution over the number of successes in a sequence of independent and identical Bernoulli
1804 trials. The beta-binomial distribution is similar, but allows for a bit more flexibility while still
1805 being a model for heterogeneity. Similar to the binomial and beta-binomial, the Conway-
1806 Maxwell-binomial distribution is a probability distribution over the number of successes in a
1807 series of Bernoulli trials, but allows over- and under-dispersion relative to the binomial dis-
1808 tribution. This distribution should therefore be a good candidate for our purposes. We found
1809 that Conway-Maxwell-binomial distribution was usually the best candidate of the three that

1810 we examined.

1811 We also observed some interesting changes in the number of active neurons in the primary
1812 visual cortex and hippocampus at stimulus onset and some changes in this activity in the
1813 thalamus which were sustained for the full duration of the stimulus presentation. This let us
1814 know that there were some responses to model.

1815 We found that fitting a Conway-Maxwell-binomial distribution was a better method of
1816 capturing association between neurons than measuring the spike count correlation for the
1817 short time bins that we used (< 10ms).

1818 Finally, we also wanted to investigate parallels between the parameters of the Conway-
1819 Maxwell-binomial distribution and quantities that have been established as relevant to sen-
1820 sory processing. So, we replicated the findings made by Churchland et al. (2010) relating
1821 to a reduction in neural variability at stimulus onset in the macaque cortical regions, but for
1822 data taken from the mouse primary visual cortex. We compared these findings to the values
1823 of the fitted Conway-Maxwell-binomial distribution parameters.

1824 4.2 Data

1825 We used data collected by Nick Steinmetz and his lab ‘CortexLab at UCL’ (Steinmetz, Caran-
1826 dini, and Harris, 2019). The data can be found online ¹ and are free to use for research
1827 purposes.

1828 Two ‘Phase3’ Neuropixels (Jun et al., 2017) electrode arrays were inserted into the brain
1829 of an awake, head-fixed mouse for about an hour and a half. These electrode arrays recorded
1830 384 channels of neural data each at 30kHz and less than $7\mu\text{V}$ RMS noise levels. The sites
1831 are densely spaced in a ‘continuous tetrode’-like arrangement, and a whole array records
1832 from a 3.8mm span of the brain. One array recorded from visual cortex, hippocampus, and
1833 thalamus, the other array recorded from motor cortex and striatum. The data were spike-
1834 sorted automatically by Kilosort and manually by Nick Steinmetz using Phy. In total 831
1835 well-isolated individual neurons were identified.

1836 4.2.1 Experimental protocol

1837 The mouse was shown a visual stimulus on three monitors placed around the mouse at right
1838 angles to each other, covering about ± 135 degrees azimuth and ± 35 degrees elevation.

¹<http://data.cortexlab.net/dualPhase3/>

1839 The stimulus consisted of sine-wave modulated full-field drifting gratings of 16 drift di-
1840 rections ($0^\circ, 22.5^\circ, \dots, 337.5^\circ$) with 2Hz temporal frequency and 0.08 cycles/degree spatial
1841 frequency displayed for 2 seconds plus a blank condition. Each of these 17 conditions were
1842 presented 10 times in a random order across 170 different trials. There were therefore 160
1843 trials with a drifting-grating visual stimulus present, and 10 trials with a blank stimulus.

1844 **4.3 Methods**

1845 **4.3.1 Binning data**

1846 We converted the spike times for each cell into spike counts by putting the spike times into
1847 time bins of a given ‘width’ (in milliseconds). We used time bins of 1ms, 5ms, and 10ms.
1848 We used different time bin widths to assess the impact of choosing a bin width.

1849 **4.3.2 Number of *active* neurons**

1850 To count the number of active neurons in each neuronal ensemble, we split the time interval
1851 for each trial into bins of a given width. We counted the number of spikes fired by each cell
1852 in each bin. If a cell fired *at least* one spike in a given bin, we regarded that cell as active in
1853 that bin. We recorded the number of active cells in every bin, and for the purposes of further
1854 analysis, we recorded each cell’s individual spike counts.

1855 It should be noted that when we used a bin width of 1ms, the maximum number of
1856 spikes in any bin was 1. For the wider time bins, some bins had spike counts greater than
1857 1. Consequently when using a bin width of 1ms, the number of active neurons and the total
1858 spike count of a given bin were identical. But for wider bin widths, the total spike count was
1859 greater than the number of active neurons.

1860 So for the 1ms bin width, the activity of a neuron and the number of spikes fired by that
1861 neuron in any bin can be modelled as a Bernoulli variable. But for wider time bins, only the
1862 activity can be modelled in this way.

1863 **4.3.3 Moving windows for measurements**

1864 When taking measurements (e.g. moving average over the number of active neurons) or
1865 fitting distributions (eg. the beta binomial distribution) we slid a window containing a certain
1866 number of bins across the data, and made our measurements at each window position. For
1867 example, when analysing 1ms bin data, we used a window containing 100 bins, and we slid

Bin width (ms)	Window size (bins)	Window size (ms)	Windows per trial
1ms	100	100ms	296
5ms	40	200ms	286
10ms	40	400ms	266

TABLE 4.1: Details of the different bin width and analysis window sizes used when binning spike times, and analysing those data.

1868 the window across the time interval for each trial moving 10 bins at a time. So that for
 1869 3060ms of data, we made 296 measurements.

1870 For the 5ms bin width data, we used windows containing 40 bins, and slid the window 2
 1871 bins at a time when taking measurements.

1872 For the 10ms bin width data, we used windows containing 40 bins, and slid the window
 1873 1 bin at a time when taking measurements (see table 4.1 for concise details).

1874 By continuing to use windows containing 40 bins, we retained statistical power but sac-
 1875 rificed the number of measurements taken.

1876 There was an interval between each trial with a grey image in place of the moving of
 1877 the moving bar stimulus. This interval varied in time. But we included some of this interval
 1878 when recording the data for each trial. We started recording the number of active neurons,
 1879 and the number of spikes from each neuron from 530ms before each trial until 1030ms after
 1880 each trial. This way, we could see the change in our measurements at the onset of a stimulus
 1881 and the end of stimulus presentation.

1882 As mentioned in section 4.3.2, we recorded the number of active neurons in each bin, and
 1883 the spike count for each neuron in each bin. The actual measurements we took using these
 1884 data in each window were as follows:

1885 **Moving average** The average number of active cells in each window.

1886 **Moving variance** The variance of the number of active cells in each window.

1887 **Average correlation** We measured the correlation between the spike counts of each pair of
 1888 cells in the ensemble, and took the average of these measurements.

1889 **Binomial p** We fitted a binomial distribution to the data in each window and recorded the
 1890 fitted probability of success, p in each case.

1891 **Beta-binomial α, β** We fitted a beta-binomial distribution to the data in each window, and
 1892 recorded the values of the fitted shape parameters, α and β , of each distribution.

1893 **Conway-Maxwell-binomial distribution p, ν** We fitted a Conway-Maxwell-binomial dis-
 1894 tribution to the data in each window, and recorded the fitted values of p and ν for each
 1895 distribution.

1896 **Log-likelihoods** We also recorded the log-likelihood of each of the fitted distributions for
 1897 each window.

1898 **4.3.4 Fano factor**

The *Fano factor* of a random variable is defined as the ratio of the variable's variance to its mean.

$$F = \frac{\sigma^2}{\mu} \quad (4.1)$$

1899 We measured the Fano factor of the spike count of a given cell by measuring the mean and
 1900 variance of the spike count across trials, and taking the ratio of those two quantities. When
 1901 calculated in this way the Fano factor can be used as a measure of neural variability that
 1902 controls for changes in the firing rate. This is similar to the calculation used in (Churchland
 1903 et al., 2010).

1904 **4.3.5 Probability Distributions suitable for modelling ensemble activity**

1905 We present here three different probability distributions that could be suitable to model the
 1906 number of active neurons in an ensemble. Each distribution has the set $\{0, \dots, n\}$ as its sup-
 1907 port, where n is the number of neurons in the ensemble. These are simple distributions with
 1908 either two or three parameters each. However, we regard n as known when using these dis-
 1909 tributions for modelling, so in effect each distribution has either one or two free parameters.

1910 **Association**

1911 *Association* between random variables is similar to the correlation between random variables
 1912 but is more general in concept. The correlation is a measure of association; and association
 1913 doesn't have a mathematical definition like correlation does. Essentially, the association
 1914 between two random variables is their tendency to take the same or similar values. Positively
 1915 associated variables tend to take the same value, and negatively associated variables tend to
 1916 take different values. In this research, we work with probability distributions of the number of
 1917 successes in a set of Bernoulli trials. These Bernoulli variables may or may not be associated.

1918 A probability distribution over the number of successes in n Bernoulli trials, where the
 1919 Bernoulli variables may be associated, could constitute a good model for the number of active
 1920 neurons in an ensemble of n neurons.

1921 **Binomial distribution**

The binomial distribution is a two parameter discrete probability distribution that can be thought of as a probability distribution the number of successes from n independent Bernoulli trials, each with the same probability of success. The parameters of the binomial distribution are n the number of trials, and $0 \leq p \leq 1$, the probability of success for each of these trials. A random variable with the binomial distribution can take values from $\{0, \dots, n\}$. The probability mass function of the distribution is

$$P(k; n, p) = \binom{n}{k} p^k (1-p)^{n-k} \quad (4.2)$$

1922 As a model for the activity of a neuronal ensemble, the main problem with the binomial
 1923 distribution is that it treats each neuron, represented as a Bernoulli trial, as independent. It is
 1924 well known that neurons are not independent, and that correlated behaviour between neurons
 1925 is vital for representing sensory information (Cohen and Maunsell, 2009). The binomial dis-
 1926 tribution falls short in this regard, but it is useful as performance benchmark when assessing
 1927 the performance of other models.

1928 **Beta-binomial distribution**

1929 The beta distribution is the conjugate distribution of the binomial distribution. The beta-
 1930 binomial distribution is the combination of the beta distribution and the binomial distribution,
 1931 in that the probability of success for the binomial distribution is sampled from the beta dis-
 1932 tribution. This allows the beta-binomial distribution to capture some over dispersion relative
 1933 to the binomial distribution.

The beta-binomial distribution is a three parameter distribution, n the number of Bernoulli trials, and $\alpha \in \mathbb{R}_{>0}$ and $\beta \in \mathbb{R}_{>0}$ the shape parameters of the beta distribution. The probability mass function for the beta-binomial distribution is

$$P(k; n, \alpha, \beta) = \binom{n}{k} \frac{B(k + \alpha, n - k + \beta)}{B(\alpha, \beta)} \quad (4.3)$$

1934 where $B(\alpha, \beta)$ is the beta function.

This probability distribution can be reparametrised in a number of ways. One of which defines new parameters π and ρ by

$$\pi = \frac{\alpha}{\alpha + \beta} \quad (4.4)$$

$$\rho = \frac{1}{\alpha + \beta + 1} \quad (4.5)$$

1935 This reparametrisation is useful because π acts as a location parameter analogous to the p
 1936 parameter of a binomial distribution. A value of $\rho > 0$ indicates over-dispersion relative to a
 1937 binomial distribution.

1938 As a model for the activity of a neuronal ensemble, the beta-binomial distribution is
 1939 more suitable than a binomial distribution because the over-dispersion of the beta-binomial
 1940 distribution can be used to model positive association between the neurons. An extreme
 1941 example of this over-dispersion/positive association can be seen in figure 4.1b. In this figure,
 1942 the neurons are positively associated and so tend to take the same value, consequently the
 1943 probability mass of the beta-binomial distribution builds up close to $k = 0$ and $k = n$. It is
 1944 worth noting that the location parameter for each distribution has the same value, $p = \pi =$
 1945 0.5.

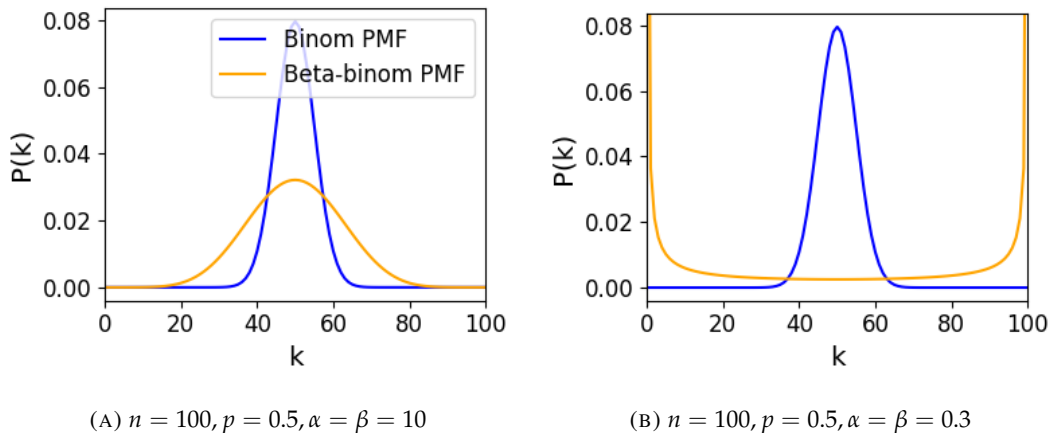


FIGURE 4.1: Figures showing the over-dispersion possible for a beta-binomial distribution relative to a binomial distribution. Parameters are shown in the captions.

1946 Conway-Maxwell-binomial distribution

1947 The Conway-Maxwell-binomial distribution (COMb distribution) is a three parameter generalisation of the binomial distribution that allows for over dispersion and under dispersion
 1948

relative to the binomial distribution. The parameters of the distribution are n the number of Bernoulli trials, and two shape parameters $0 \leq p \leq 1$, and $\nu \in \mathbb{R}$.

The probability mass function of the COMb distribution is

$$P(k; n, p, \nu) = \frac{1}{S(n, p, \nu)} \binom{n}{k}^{\nu} p^k (1-p)^{n-k} \quad (4.6)$$

where

$$S(n, p, \nu) = \sum_{j=0}^n \binom{n}{j}^{\nu} p^j (1-p)^{n-j} \quad (4.7)$$

The only difference between this PMF and the PMF for the standard binomial is the introduction of ν and the consequent introduction of the normalising function $S(n, p, \nu)$.

Indeed, if $\nu = 1$ the COMb distribution is identical to the binomial distribution with the same values for n and p . We can see in figure 4.2d that the KL-divergence $D_{KL}(P_{COMb}(n, p, \nu) || P_{Bin}(n, p)) = 0$ along the line where $\nu = 1$. The analytical expression for the divergence is

$$D_{KL}(P_{COMb}(k; n, p, \nu) || P_{Bin}(k; n, p)) = (\nu - 1) E_{P_{COMb}(k; n, p, \nu)} \left[\log \binom{n}{k} \right] \quad (4.8)$$

$$- \log S(n, p, \nu) \quad (4.9)$$

At $\nu = 1$, we have $S(n, p, 1)$ which is just the sum over the binomial PMF, so $S(n, p, 1) = 1$ and therefore $D_{KL}(P_{COMb}(n, p, \nu) || P_{Bin}(n, p)) = 0$.

If $\nu < 1$ the COMb distribution will exhibit over-dispersion relative to the binomial distribution. If $p = 0.5$ and $\nu = 0$ the COMb distribution is the discrete uniform distribution, and if $\nu < 0$ the mass of the COMb distribution will tend to build up near $k = 0$ and $k = n$. This over-dispersion represents positive association in the Bernoulli variables. An example of this over-dispersion can be seen in figure 4.2b.

If $\nu > 1$ the COMb distribution will exhibit under-dispersion relative to the binomial distribution. The larger the value of ν the more probability mass will build up at $n/2$ for even n , or at $\lfloor n/2 \rfloor$ and $\lceil n/2 \rceil$ for odd n . This under-dispersion represents negative association in the Bernoulli variables. An example of this under-dispersion can be seen in figure 4.2a.

It should be noted that the p parameter of the COMb distribution does not correspond to the mean of the distribution, as is the case for the binomial p parameter, and beta-binomial π parameter. That is, the COMb p parameter is not a location parameter. An illustration of this can be seen in figure 4.2c. This is because an interaction between the p and ν parameters skews the mean. There is no analytical expression for the mean of the COMb distribution.

ν	Relative dispersion	Association between neurons/variables
< 1	over	positive
1	none	none
> 1	under	negative

TABLE 4.2: Relative dispersion of the COMb distribution, and association between Bernoulli variables as represented by the value of the ν parameter.

1969 Since the COMb distribution has the potential to capture positive and negative associa-
 1970 tions between the neurons/Bernoulli variables, it should be an excellent candidate for mod-
 1971 elling the number of active neurons in a neuronal ensemble.

1972 We wrote a dedicated Python package to enable easy creation and fitting of COMb dis-
 1973 tribution objects. The format of the package imitates the format of other distribution objects
 1974 from the `scipy.stats` Python package. The COMb package can be found here:
 1975 https://github.com/thomasjdelaney/Conway_Maxwell_Binomial_Distribution

1976 4.3.6 Fitting

1977 We fitted binomial, beta-binomial, and Conway-Maxwell-binomial (COMb) distributions to
 1978 the neural activity in each of the overlapping windows covering each trial. To fit the distribu-
 1979 tions we minimised the appropriate negative log likelihood function using the data from the
 1980 window.

There is an analytical solution for maximum likelihood estimate of the binomial distribution's p parameter.

$$\hat{p} = \frac{1}{n} \sum_{i=1}^N k_i \quad (4.10)$$

1981 We minimised the negative log likelihood function of the beta-binomial distribution nu-
 1982 merically. We calculated the negative log likelihood for a sample directly, by taking the sum
 1983 of the log of the probability mass function for each value in the sample. We minimised the
 1984 negation of that function using the `minimise` function of the `scipy.optimize` Python
 1985 package.

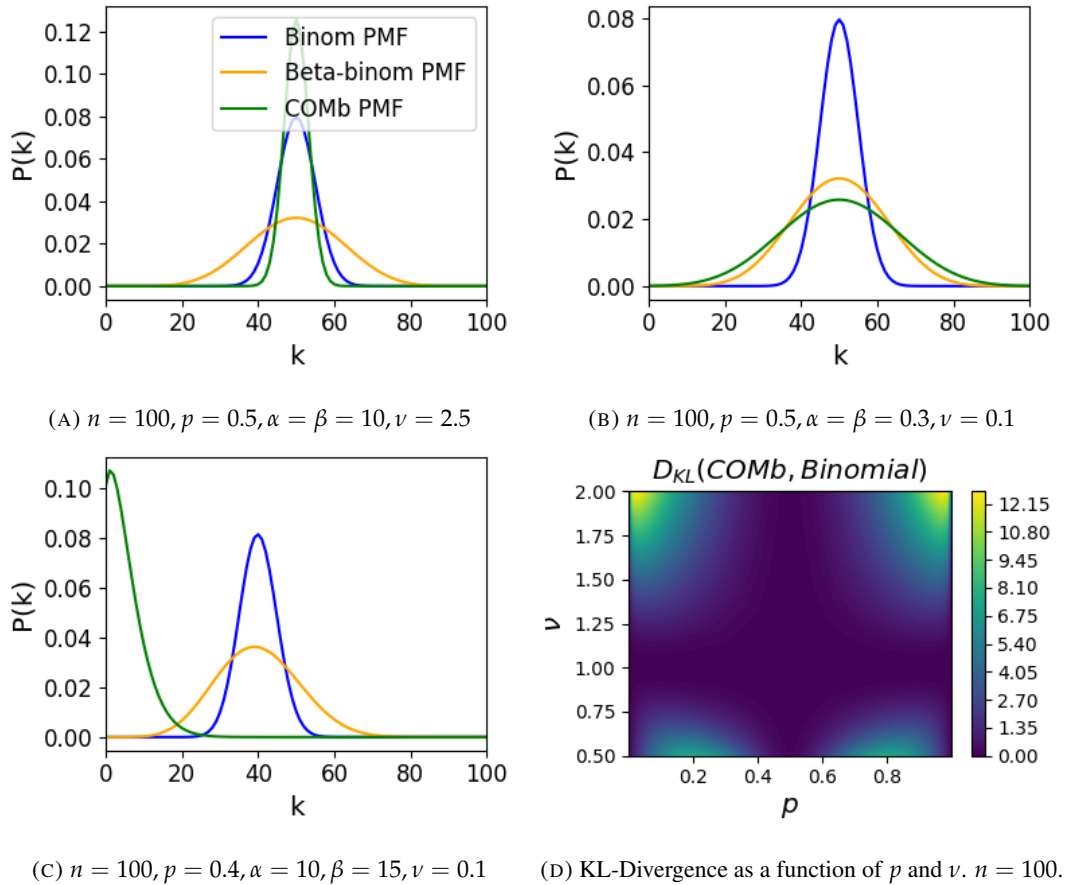


FIGURE 4.2: Figures showing (A) the under-dispersion and (B) over-dispersion permitted by the COMb distribution relative to a binomial distribution. (C) illustrates that the p parameter of the COMb distribution does not correspond to the mean of the distribution, as it does for the binomial and beta-binomial distributions. (D) shows a heatmap for the value of the Kullback-Liebler divergence between the COMb distribution and the standard binomial distribution with same value for n , as a function of p and ν . Parameters are shown in the captions.

The log likelihood function of the COMb distribution given some sample $\{k_1, \dots, k_N\}$ is

$$\ell(p, \nu | k_1, \dots, k_N) = N [n \log(1 - p) - \log S(n, p, \nu)] \quad (4.11)$$

$$+ \log \frac{p}{1 - p} \sum_{i=1}^N k_i \quad (4.12)$$

$$+ \nu \sum_{i=1}^N \log \binom{n}{k_i} \quad (4.13)$$

1986 We minimised the negation of this function using numerical methods. More specifically, we
 1987 used the `minimise` function of the `scipy.optimize` Python package.

1988 **4.3.7 Goodness-of-fit**

1989 After fitting, we measured the goodness-of-fit of each model/distribution with their log like-
 1990 lihood. We calculated this directly using the `logpmf` functions of the distribution objects in
 1991 Python.

1992 **4.4 Results**

1993 We defined a neuron as *active* in a time bin if it fires at least one spike during the time interval
 1994 covered by that bin. We measured the number of active neurons in the primary visual cortex
 1995 of a mouse in 1ms bins across 160 trials of a moving bar visual stimulus. We then slid a
 1996 100ms window across these 1ms bins taking measurements, and fitting distributions along
 1997 the way. We did the same for neurons in the thalamus, hippocampus, striatum, and motor
 1998 cortex. We repeated the analysis for 5ms time bins with 40 bin windows, and 10ms time bins
 1999 with 40 bin windows.

2000 **4.4.1 Increases in mean number of active neurons and variance in number of
 2001 active neurons at stimulus onset in some regions**

2002 We measured the average number of active neurons, and the variance of the number of active
 2003 neurons in a 100ms sliding window starting 500ms before stimulus onset until 1000ms after
 2004 stimulus onset. We found differences in the response across regions. There were no observed
 2005 changes in response to the stimulus in the motor cortex or the striatum. The changes in the
 2006 other regions are detailed below.

2007 **Primary visual cortex**

2008 We found a transient increase in both the average and variance of the number of active neu-
2009 rons at stimulus onset, followed by a fall to pre-stimulus levels, followed by another transient
2010 increase (see figure 4.3). The oscillation in both of these measurements appear to reflect the
2011 frequency of the stimulus (see Data section 4.2.1), and it is known that stimulus structure can
2012 influence response structure(Litwin-Kumar, Chacron, and Doiron, 2012). We see a similar
2013 but lower amplitude oscillation at the end of the stimulus presentation.

2014 **Hippocampus**

2015 In the hippocampus we observed a transient increase in the average number of active neurons
2016 and in the variance of the number of active neurons at stimulus onset (see figure 4.4). The
2017 increase lasted about 125ms, and the subsequent fall to baseline took the a similar amount of
2018 time.

2019 **Thalamus**

2020 In the thalamus we observed a transient increase in the both the average and variance of
2021 the number of active neurons on stimulus onset, followed by a fall to pre-stimulus levels,
2022 followed by a sustained increase until the stimulus presentation ends.

2023 As one you might expect for a visual stimulus, the change in the average number of active
2024 neurons was greatest in the primary visual cortex. In this region, this quantity doubled on
2025 stimulus onset. In contrast, in the hippocampus and the thalamus, the average number of
2026 active neurons only increased by a fraction of the unstimulated baseline value. The duration
2027 of the response in V1 and the hippocampus at stimulus onset was 300 – 400ms, but the
2028 response in the thalamus appeared to last for the duration of stimulus presentation. The V1
2029 also showed a change in the average number of active neurons at stimulus end. The change
2030 was similar to that observed at stimulus onset, but smaller in magnitude (see figures 4.3, 4.4,
2031 and 4.5)

2032 **4.4.2 Conway-Maxwell-binomial distribution is usually a better fit than bino-
2033 mial or beta-binomial**

2034 Since the Conway-Maxwell-binomial distribution has not been fitted to neuronal data before,
2035 it is not clear that it would be a better fit than the binomial or beta-binomial distributions.
2036 In order to find out which parametric distribution was the best fit for the largest proportion

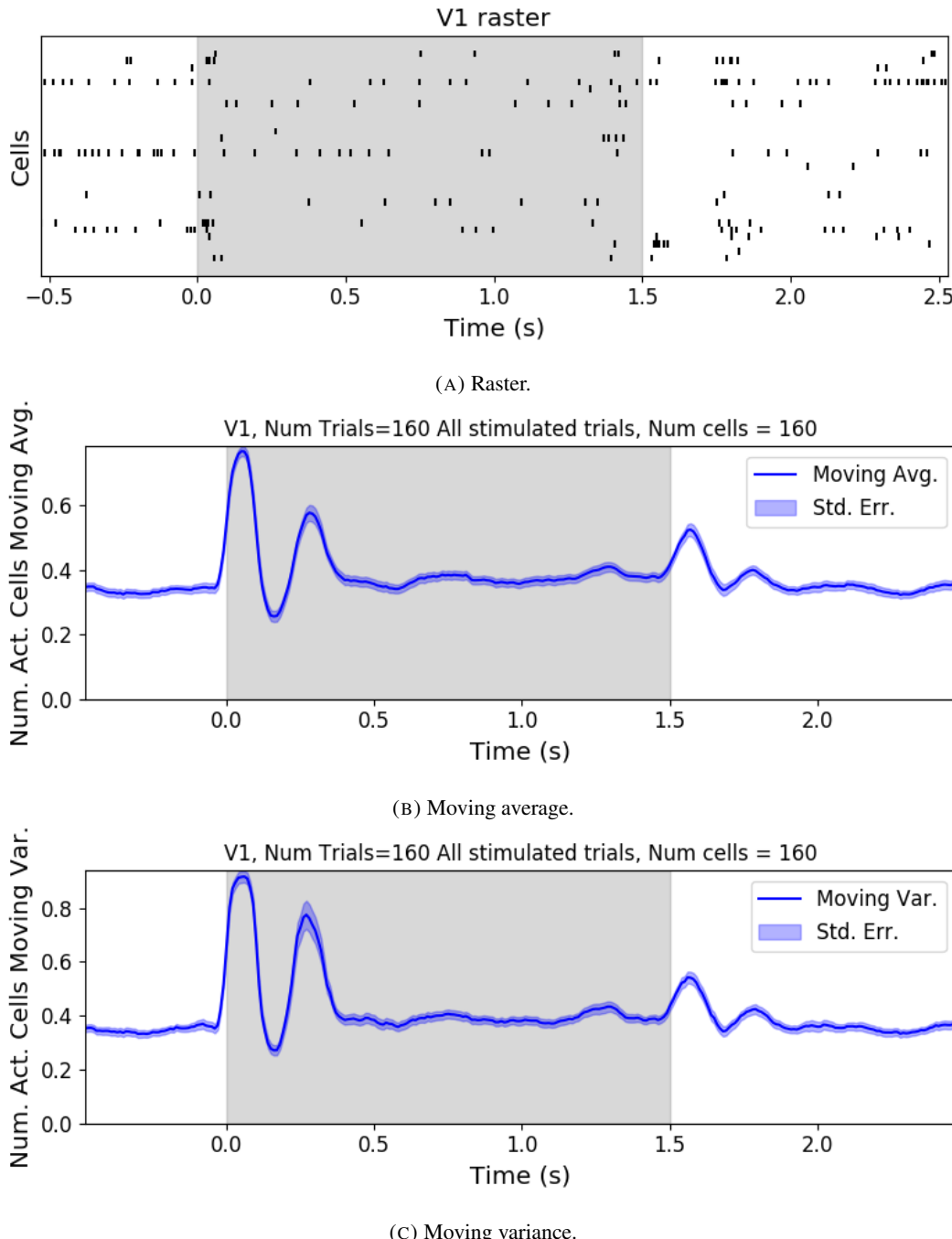


FIGURE 4.3: (A) Raster plot showing the spikes fired by 33 randomly chosen neurons in the primary visual cortex. (B-C) (B) average and (C) variance of the number of active neurons, measured using a sliding window 100ms wide, split into 100 bins. The midpoint of the time interval for each window is used as the timepoint (x-axis point) for the measurements using that window. The grey shaded area indicates the presence of a visual stimulus. The opaque line is an average across the 160 trials that included a visual stimulus of any kind. We can see a transient increase in the average number of active neurons and the variance of this number, followed by a fluctuation and another increase.

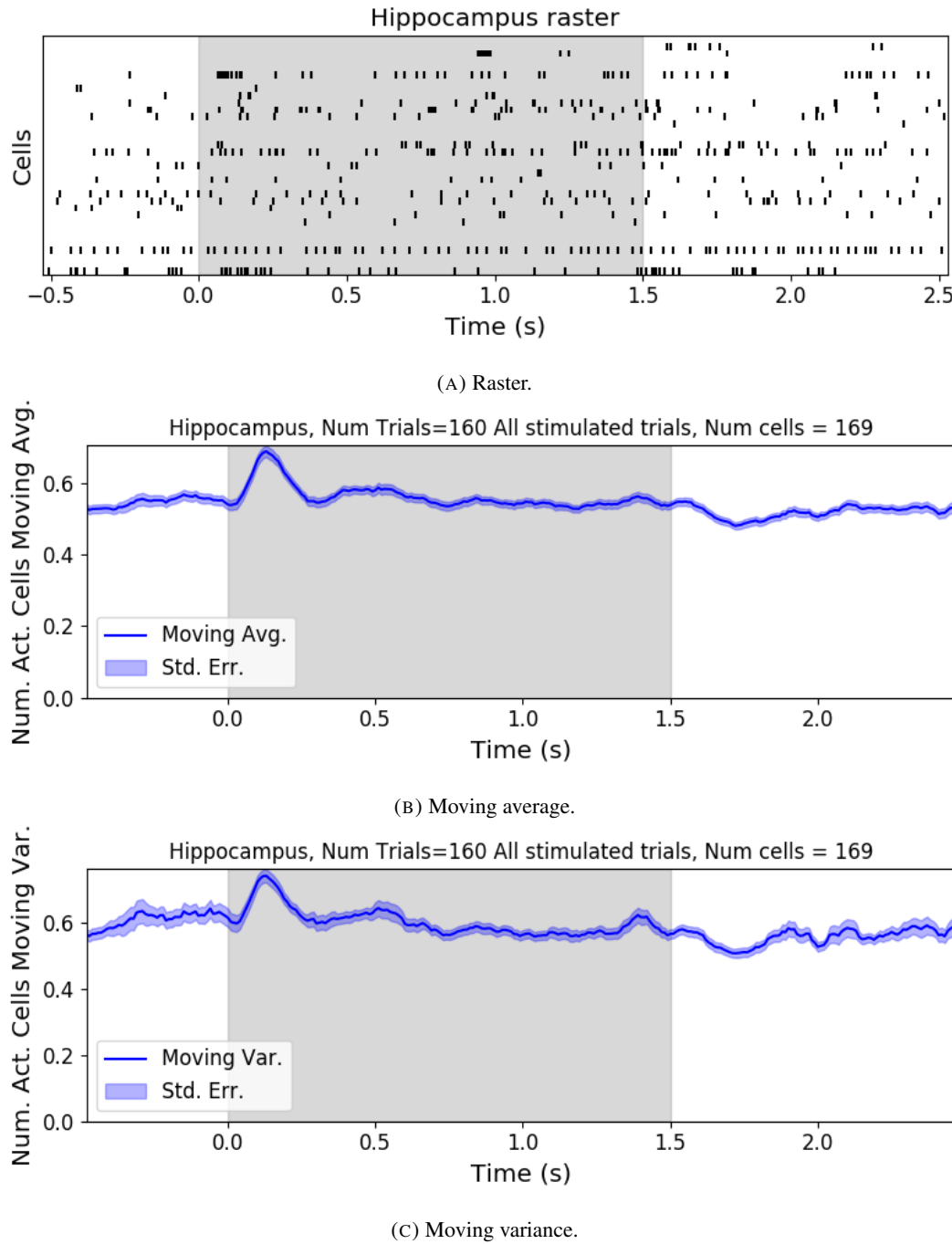


FIGURE 4.4: (A) Raster plot showing the spikes fired by 33 randomly chosen neurons in the hippocampus. (B-C) (B) average and (C) variance of the number of active neurons, measured using a sliding window 100ms wide, split into 100 bins. The midpoint of the time interval for each window is used as the timepoint (x-axis point) for the measurements using that window. The grey shaded area indicates the presence of a visual stimulus. The opaque line is an average across the 160 trials that included a visual stimulus of any kind. We can see a transient increase in the average number of active neurons and the variance of this number at stimulus onset.

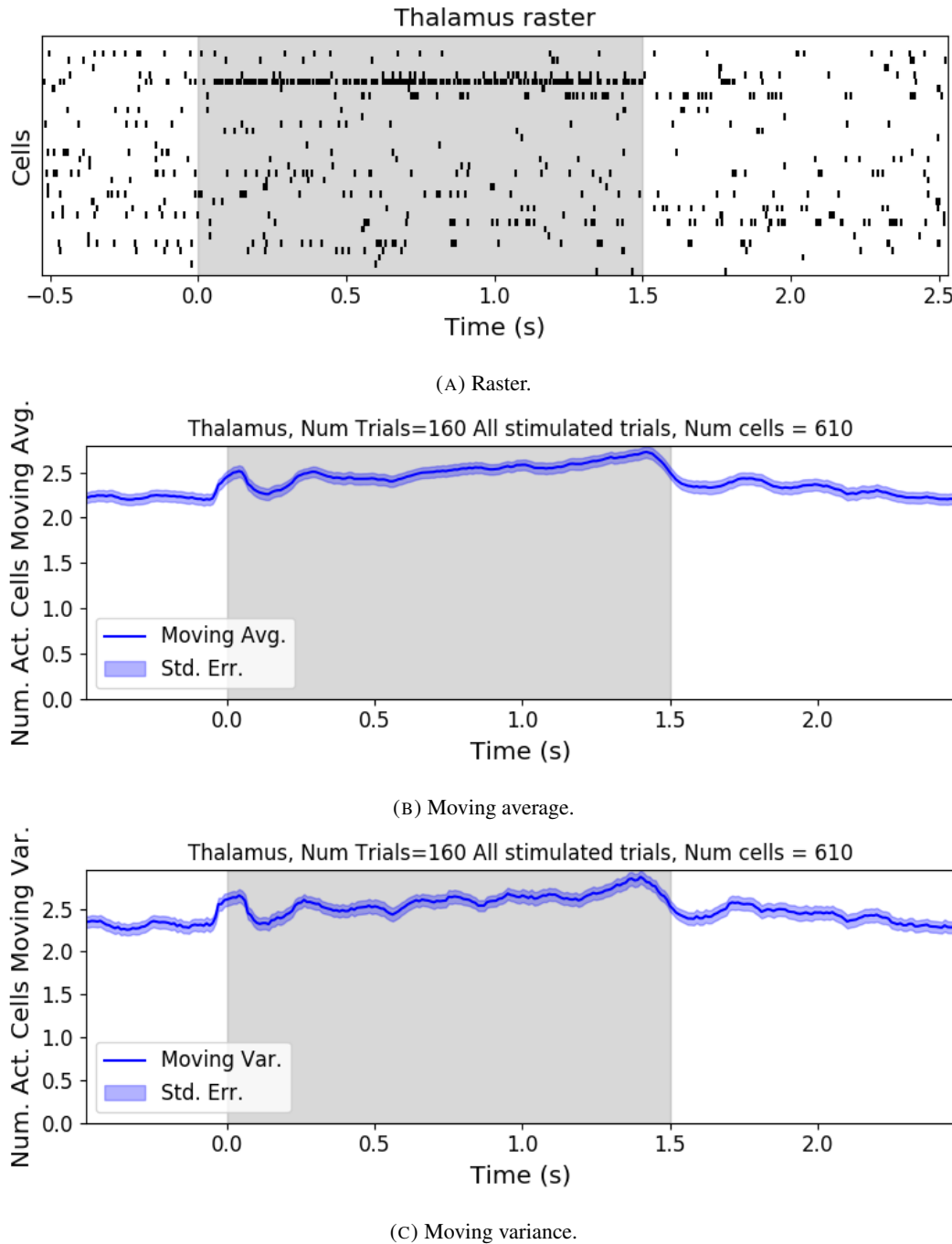
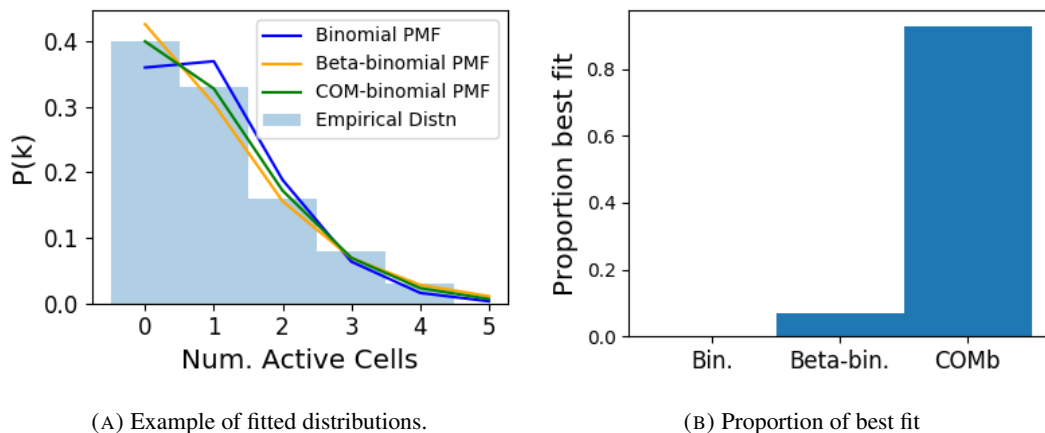


FIGURE 4.5: (A) Raster plot showing the spikes fired by 33 randomly chosen neurons in the thalamus. (B-C) (B) average and (C) variance of the number of active neurons, measured using a sliding window 100ms wide, split into 100 bins. The midpoint of the time interval for each window is used as the timepoint (x-axis point) for the measurements using that window. The grey shaded area indicates the presence of a visual stimulus. The opaque line is an average across the 160 trials that included a visual stimulus of any kind. We can see an immediate increase at stimulus onset, a subsequent fall, and another sustained increase until the stimulus presentation ends.

of our data, we fit a binomial, a beta-binomial, and a Conway-Maxwell-binomial (COMb) distribution to each window for each bin width, and each region. Then we assessed the goodness-of-fit of each distribution by calculating the log-likelihood of each fitted distribution using the associated sample. We measured the proportion of samples for which each distribution was the best fit, for each bin width value and each region.

We found that the COMb distribution was the best fit for most of the samples regardless of bin width or region. The bin width had an effect on the number of samples for which the COMb distribution was the best fit. The results are summarised in table 4.3. For a bin width of 1ms, the COMb distribution was the best fit for over 90% of samples, the beta-binomial distribution was the best fit for less than 10% of samples, and the binomial distribution was the best fit for less than 1% of samples, across regions. For 5ms bins, the COMb distribution was the best fit for 70 – 80% of samples, the beta-binomial distribution was the best fit for 20 – 30% of the samples, and again the binomial distribution was the best fit for less than 1% of samples, across regions. Finally, for 10ms bins, the COMb distribution was the best fit for 53 – 80% of samples, the beta-binomial distribution was the best fit for 20 – 47% of the samples, and the binomial distribution was the best fit for less than 0.1% of samples, across regions.



(A) Example of fitted distributions.

(B) Proportion of best fit

FIGURE 4.6: (A) An example of the binomial, beta-binomial, and Conway-Maxwell-binomial distributions fitted to a sample of neural activity. The Conway-Maxwell-binomial distribution is the best fit in this case. The histogram shows the empirical distribution of the sample. The probability mass function of each distribution is indicated by a different coloured line. (B) Across all samples in all trials, the proportion of samples for which each fitted distribution was the best fit. The Conway-Maxwell-binomial distribution was the best fit for 93% of the samples taken from V1 using a bin width of 1ms.

Bin Width (ms)	Binomial	Beta-binomial	COMb
1ms	< 1%	< 10%	> 90%
5ms	< 0.1%	20 – 30%	70 – 80%
10ms	< 0.1%	20 – 47%	53 – 80%

TABLE 4.3: Proportion of samples for which each distribution was the best fit, grouped by bin width. The COMb distribution is the best fit most of the time.

2054 **4.4.3 Conway-Maxwell-binomial distribution captures changes in association
2055 at stimulus onset**

2056 We fit a Conway-Maxwell-binomial (COMb) distribution to the number of active neurons in
2057 the 1ms time bins in a 100ms sliding window. We also measured the correlation coefficient
2058 between the spike counts of all possible pairs of neurons, and took the average of these
2059 coefficients. We did this for all the trials with a visual stimulus. We observed a reduction in
2060 the COMb distribution's ν parameter at stimulus onset from around 1 to between 0 and 1 (see
2061 figure 4.7a). A value of ν less than 1 indicates positive association between the neurons (see
2062 section 4.3.5). We might expect to see this positive association reflected in the correlation
2063 coefficients, but this is not the case. We see no change in the time series of average correlation
2064 measures at stimulus onset.

2065 This may be due to the very short time bin we used in this case. We know that using small
2066 time bins can artificially reduce correlation measurements (Cohen and Kohn, 2011). In this
2067 case, fitting the COMb distribution may be a useful way to measure association in a neuronal
2068 ensemble over very short timescales (< 10ms).

2069 **4.4.4 Replicating stimulus related quenching of neural variability**

2070 Churchland et al. (2010) inspected the effect of a stimulus on neural variability. One of the
2071 measures of neural variability that they employed was the Fano factor of the spike counts of
2072 individual cells (see section 4.3.4). They found a reduction in neural variability as measured
2073 by the Fano factor in various cortical areas in a macaque at the onset of various visual stimuli,
2074 or a juice reward (Churchland et al., 2010).

2075 We measured the Fano factor of the spike count of each cell in each brain region, during
2076 each trial. We measured the mean and standard error of these Fano factors from 500ms
2077 before stimulus onset until 1000ms after stimulus end. For the primary visual cortex, we
2078 found a transient reduction in the Fano factor immediately after stimulus onset. We used
2079 a Mann-Whitney U test to check that the Fano factors measured in a window starting at

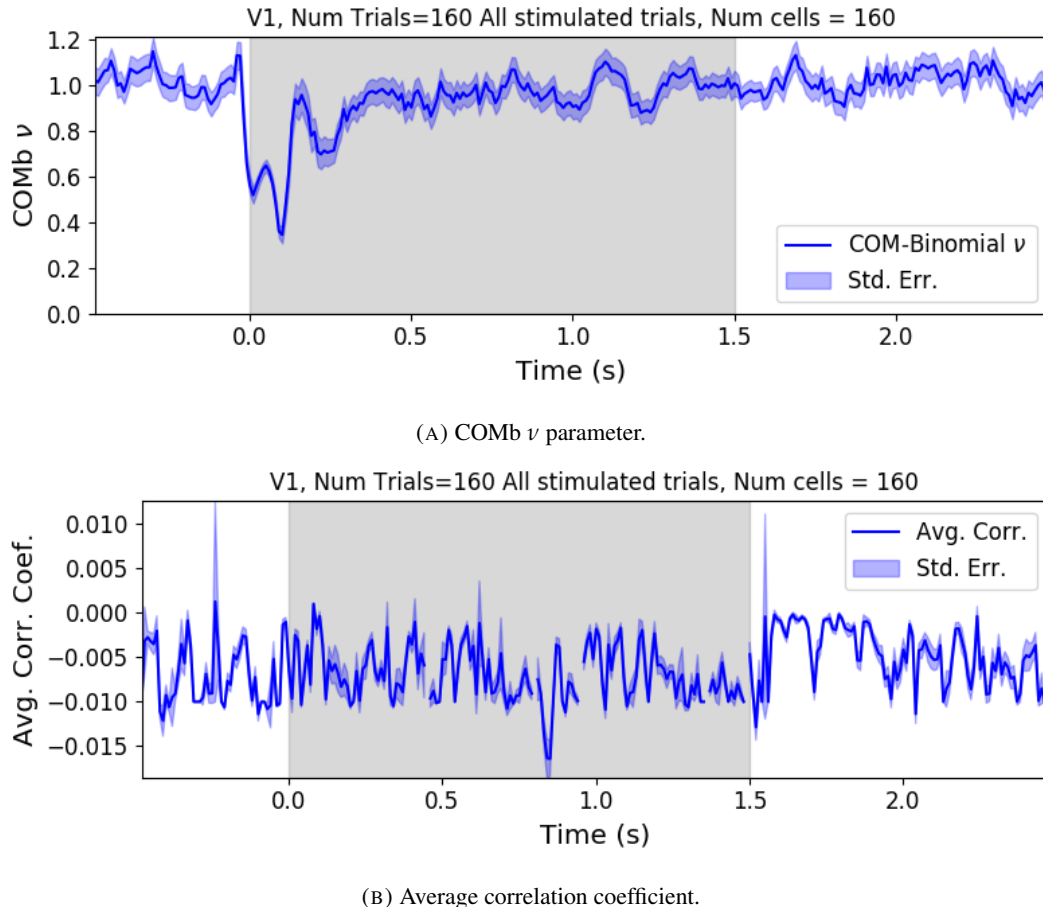


FIGURE 4.7: (A) We fit a Conway-Maxwell-binomial distribution to the number of active neurons in 1ms time bins of a 100ms sliding window. We did this for all trials with a visual stimulus and took the average across those trials. We see a transient drop in value for the distribution’s ν parameter at stimulus onset. This shows an increase in association between the neurons. (B) We measured the correlation coefficient between the spike counts of all possible pairs of neurons in the same sliding window. The took the average of those coefficients. We also did this for every visually stimulated trial, and took the average across trials. The increase in association is not reflected with an increase in average correlation.

stimulus onset and ending 100ms later were significantly lower than the factors measured in a window ending at stimulus onset ($p < 0.001$, see figure 4.8a). We did not get this statistically significant result in any other region.

Our findings agree with those of Churchland et al. for the primary visual cortex. However Churchland also found a reduction in the Fano factor in the dorsal premotor cortex (PMd) at stimulus onset. Our measurements from the mouse motor cortex show no change at stimulus onset (see figure 4.8b). This could indicate some difference in the functionality of the motor cortex in a macaque and the motor cortex of a mouse.

Similar to these findings in the Fano factor, we found a reduction in the ν parameter of the COMB distribution on stimulus onset in V1 (figure 4.7a) and in no other region from

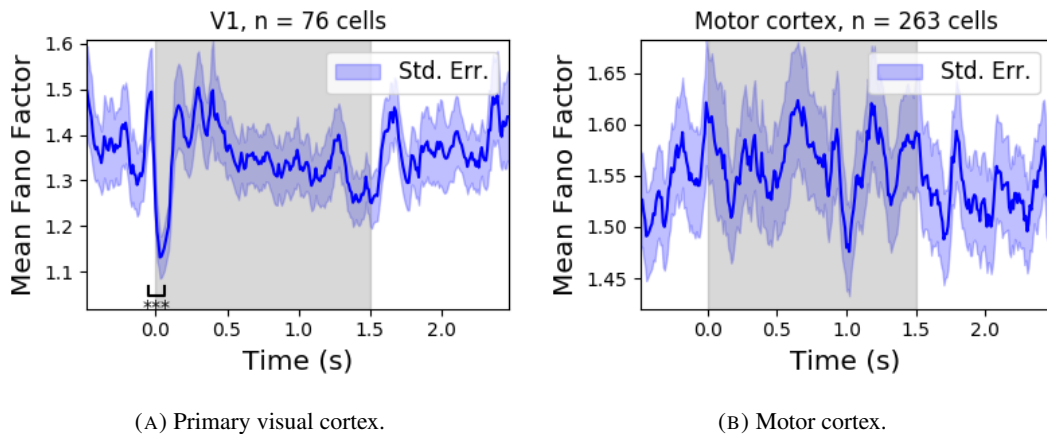


FIGURE 4.8: (A) The mean Fano factor of the spike counts of the cells in the primary visual cortex. Means were taken across cells first, then across trials. There was a significant decrease in the Fano factors immediately after stimulus onset. (B) The mean Fano factor of the spike counts of the cells in the motor cortex. No significant change in measurements at any point.

which we had data. Specifically, the ν parameter reduced from around 1, to between 1 and 0. This represents a change from no association between the neurons, to a positive association. It is possible that this positive association may be responsible for the reduction in the Fano factor.

4.5 Discussion

Our aim in this research was to develop a new statistical method for analysing the activity of a neuronal ensemble at very short timescales. We wanted our method to use information taken from the whole ensemble, but we also wanted the method to be quick and easy to implement. It is likely that analysis methods with these characteristics will become valuable as electrophysiological datasets include readings from more cells over longer time periods. In this case, we used the number of active, or spiking, neurons in a very short time bin ($< 10\text{ms}$) as a measure of ensemble activity.

First of all, we showed that there were changes in response that we could model at these very short time scales in some of the brain regions from which we had recordings. We observed changes in the average number of active neurons, and the variance of the number of active neurons in three different brain regions in response to visual stimuli. Since we know that correlated behaviour is associated with sensory perception (deCharms and Merzenich, 1996), we might hope to measure the pairwise correlations within the neuronal population in order to further investigate these responses. But, using such short time bins can produce

artificially small spike count correlation measurements (Cohen and Maunsell, 2009). Overcoming this limitation was one of our objectives for our new method. In order to do this, we abandoned the idea of measuring the correlations directly and embraced the concept of *association*. In order to quantify the association between neurons, we used the Conway-Maxwell-binomial distribution to model the number of active (spiking) neurons in an ensemble as a sum of possibly associated Bernoulli random variables.

We showed that the Conway-Maxwell-binomial distribution performed better than the more common options of the binomial and beta-binomial distributions. Furthermore, we showed that the positively associated behaviour between neurons in the primary visual cortex could be captured by fitting a Conway-Maxwell-binomial distribution, but was not captured by the more standard approach of measuring the spike count correlation. The associated behaviour could not be measured using spike count correlations, because of the very short bins required to capture short timescale behaviour.

We replicated a famous result from Churchland et al (2010) relating to the quenching of neural variability in cortical areas at stimulus onset, and in doing so, we established a correspondence between the association quantifying parameter of the Conway-Maxwell-binomial (COMb) distribution and the neural variability as measured by the Fano factor. We found a reduction in the ν parameter of the COMB distribution at stimulus onset, indicating a change from no association to positive association between neurons in V1. We found a corresponding reduction in the Fano factor of the individual cells in V1. The positive association between neurons induced by the stimulus would constrain the neurons to fire at the same time. The stimulus also induced a larger number of neurons to spike. These two actions combined could cause an increase in the firing rate of individual cells that is greater in magnitude than the increase in firing rate variability. If this is indeed the case, then the association as captured by the COMB distribution could be regarded as one of the ‘natural parameters’ of the ensemble response for short timescales. That is, a quantity that directly measures some aspect of the behaviour of the ensemble. In this case, it the correlated behaviour of the individual neurons is captured.

This work could be just a first step in creating analysis methods based on the Conway-Maxwell-binomial distribution, or similar statistical models. One way to extend the method would be to pair it up with the ‘Population Tracking model’ (O’Donnell et al., 2017). This model attempts to characterise the interaction between an ensemble and each member of the ensemble by quantifying the probability of spiking for a given a cell, given the number of active cells in the whole population. Combining this model with the COMB distribution

2143 would give us a model that could accurately fit the number of active neurons at any moment,
2144 and that gives a probability of firing for each cell, and therefore probabilities for full spiking
2145 patterns, without adding a huge number of parameters to fit.

2146 A more complex way to extend the model would be to fit a Conway-Maxwell-binomial
2147 distribution to data recorded from multiple brain regions simultaneously, with a different fit
2148 for each region, then to analyse the temporal relationship between the fitted parameters of
2149 each region. If we analysed the time series of the COMB distribution parameters from the
2150 different regions, looking at cross-correlations between regions, this may give some results
2151 relating to the timescales in which information is processed in different brain regions.

2152 **Chapter 5**

2153 **Studies with practical limitations &**
2154 **negative results**

2155 *Abstract*

2156 Here I will present some details on research topics that I started, but that unfortunately did not
2157 lead anywhere useful. There are two pieces of research, based on two papers. Each paper is
2158 related to the overall theme of my PhD of analysing and modelling behaviours of populations
2159 of neurons. The first part is based on a model of parallel spike trains including higher order
2160 interactions by Shimazaki et al (2012). The second part is based on a multiscale model for
2161 making inferences on hierarchical data.

2162 **5.1 Dynamic state space model of pairwise and higher order neu-**
2163 **ronal correlations**

2164 In their paper Shimazaki et al (2012) aimed to model spike trains from populations of neurons
2165 in parallel, with pairwise and higher order dynamic interactions between the trains. They
2166 modelled the spike trains as multi-variate binary processes using a log-linear model, and they
2167 extracted spike interaction parameters using a Bayesian filter/EM-algorithm. They developed
2168 a goodness-of-fit measure for the model to test if including these higher order correlations
2169 is necessary for an accurate model. Their measure was based on the Bayes factor but they
2170 also assessed the suitability of higher order models using the AIC and BIC. So the increase
2171 in the number of parameters associated with fitting higher order interactions was taken into
2172 account. They tested the performance of the model on synthetic data with known higher
2173 order correlations. They used the model to look for higher order correlations in data from
2174 awake behaving animals. They use the model to demonstrate dynamic appearance of higher
2175 order correlations in the monkey motor cortex (Shimazaki et al., 2012).

2176 We used the available Python repository to implement the model, and we successfully
2177 worked through the tutorial provided. But we found that the model did not scale well to
2178 larger populations. We attempted to fit the model to a population of 10 neurons and found we
2179 didn't manage to finish the process. Since, our goal was to find a model to scale to hundreds
2180 or thousands of neurons, we decided that this model was no longer worth pursuing.

2181 **5.2 A multiscale model for hierarchical data applied to**
2182 **neuronal data**

2183 In their paper Kolaczyk et al (2001) developed a framework for a modelling hierarchically
2184 aggregated data, and making inferences based on a model arising from this framework. They
2185 assumed that a hierarchical aggregation existed on the data in question, where each element at
2186 each level of the hierarchy had some associated measurements, an associated mean process,
2187 which was the expected value of these measurements. They also assumed that the measure-
2188 ments of each parent were equal to the sum of the measurements from all of its children.
2189 They showed that these assumptions gave rise to a relationship between parent and child
2190 measurements across all levels of the hierarchy, where the product of the likelihood of the
2191 parameters of the lowest level of the hierarchy can be expressed as products of conditional
2192 likelihoods of the elements of higher levels of the hierarchy (Kolaczyk and Huang, 2010).

2193 They gave examples of these expressions for measurements sampled from Gaussian dis-
2194 tributions, and Poisson distributions, and showed the definitions of the hierarchical param-
2195 eters which reparametrise the distribution of these data taking the hierarchy into account.
2196 They go on to suggest prior distributions for this multiscale model, and integrate these priors
2197 to give posterior distributions for the measurements from each element at each level in the hi-
2198 erarchy, and expressions for the MAP estimated parameters of each the associated processes
2199 (Kolaczyk and Huang, 2010).

2200 We implemented their model in Python by creating some synthetic data from Poisson
2201 distributions, and defining a hierarchy by agglomerating these data. We calculated the MAP
2202 estimates using our knowledge of the hierarchy, and using the expressions given in the paper.
2203 We found that the MAP estimates were far less accurate than would be achieved by simply
2204 ignoring the hierarchy during estimation, and using a maximum likelihood approach. After
2205 that, we decided to move on.

2206 5.3 Discussion

2207 Ideas (not in order):

- 2208 • Calcium imaging limitations (spike inference not always possible)
- 2209 • Judging by Greenberg biophysical modelling is the way to go.
- 2210 • our fluorescence model could be useful in a number of situations.
- 2211 • Applied new network science to new electrophysiological dataset.
- 2212 • Abandon calcium
- 2213 • Multi region calcium imaging dataset would be useful?
- 2214 • Results might be intuitive, but are new nonetheless (as far as I know)
- 2215 • Potential for more network science applications?
- 2216 • Applied the COMB distribution to neuronal data for the first time.
- 2217 • captures correlated behaviour by quantifying *association*.
- 2218 • Abandon correlations.
- 2219 • coupling with existing models could yield some nice models.
- 2220 • More statistical invention could be useful.

Bibliography

- 2221 Allen, William E. et al. (2019). “Thirst regulates motivated behavior through modulation of
 2222 brainwide neural population dynamics”. In: *Science* 364.6437. ISSN: 0036-8075. DOI:
 2223 [10.1126/science.aav3932](https://doi.org/10.1126/science.aav3932). eprint: <https://science.sciencemag.org/content/364/6437/eaav3932.full.pdf>. URL: <https://science.sciencemag.org/content/364/6437/eaav3932>.
- 2227 Baadel, S., F. Thabtah, and J. Lu (2016). “Overlapping clustering: A review”. In: *2016 SAI Computing Conference (SAI)*, pp. 233–237. DOI: [10.1109/SAI.2016.7555988](https://doi.org/10.1109/SAI.2016.7555988).
- 2229 Baldassano, Christopher et al. (2017). “Discovering Event Structure in Continuous Narrative Perception and Memory”. In: *Neuron* 95.3, 709 –721.e5. ISSN: 0896-6273. DOI: <https://doi.org/10.1016/j.neuron.2017.06.041>. URL: <http://www.sciencedirect.com/science/article/pii/S0896627317305937>.
- 2233 Bartol, Thomas M. et al. (2015). “Computational reconstitution of spine calcium transients from individual proteins”. In: *Frontiers in Synaptic Neuroscience* 7, p. 17. ISSN: 1663-3563. DOI: [10.3389/fnsyn.2015.00017](https://doi.org/10.3389/fnsyn.2015.00017). URL: <https://www.frontiersin.org/article/10.3389/fnsyn.2015.00017>.
- 2237 Berens, Philipp et al. (May 2018). “Community-based benchmarking improves spike rate inference from two-photon calcium imaging data”. In: *PLOS Computational Biology* 14.5, pp. 1–13. DOI: [10.1371/journal.pcbi.1006157](https://doi.org/10.1371/journal.pcbi.1006157). URL: <https://doi.org/10.1371/journal.pcbi.1006157>.
- 2241 Bezanson, Jeff et al. (Sept. 2012). “Julia: A Fast Dynamic Language for Technical Computing”. In: *MIT*.
- 2243 Chen, Tsai-Wen et al. (July 2013). “Ultrasensitive fluorescent proteins for imaging neuronal activity”. In: *Nature* 499, 295–300. DOI: [10.1038/nature12354](https://doi.org/10.1038/nature12354). URL: <https://doi.org/10.1038/nature12354>.
- 2246 Churchland, Mark M. et al. (2010). “Stimulus onset quenches neural variability: a widespread cortical phenomenon”. eng. In: *Nature neuroscience* 13.3. 20173745[pmid], pp. 369–378. ISSN: 1546-1726. DOI: [10.1038/nn.2501](https://doi.org/10.1038/nn.2501). URL: <https://pubmed.ncbi.nlm.nih.gov/20173745>.

- 2250 Cohen, Marlene R. and Adam Kohn (2011). “Measuring and interpreting neuronal correla-
2251 tions”. In: *Nature Neuroscience* 14.7, pp. 811–819. ISSN: 1546-1726. DOI: [10.1038/nrn.2842](https://doi.org/10.1038/nrn.2842). URL: <https://doi.org/10.1038/nrn.2842>.
- 2253 Cohen, Marlene R. and John H. R. Maunsell (2009). “Attention improves performance pri-
2254 marily by reducing interneuronal correlations”. eng. In: *Nature neuroscience* 12.12. 19915566[pmid],
2255 pp. 1594–1600. ISSN: 1546-1726. DOI: [10.1038/nrn.2439](https://doi.org/10.1038/nrn.2439). URL: <https://pubmed.ncbi.nlm.nih.gov/19915566>.
- 2257 Dana, Hod et al. (Sept. 2014). “Thy1-GCaMP6 Transgenic Mice for Neuronal Population
2258 Imaging In Vivo”. In: *PloS one* 9, e108697. DOI: [10.1371/journal.pone.0108697](https://doi.org/10.1371/journal.pone.0108697).
- 2260 deCharms, R. Christopher and Michael M. Merzenich (1996). “Primary cortical represen-
2261 tation of sounds by the coordination of action-potential timing”. In: *Nature* 381.6583,
2262 pp. 610–613. ISSN: 1476-4687. DOI: [10.1038/381610a0](https://doi.org/10.1038/381610a0). URL: <https://doi.org/10.1038/381610a0>.
- 2264 Deneux, Thomas et al. (July 2016). “Accurate spike estimation from noisy calcium signals
2265 for ultrafast three-dimensional imaging of large neuronal populations in vivo”. In: *Nature
2266 Communications* 7.1. DOI: [10.1038/ncomms12190](https://doi.org/10.1038/ncomms12190). URL: <https://doi.org/10.1038/ncomms12190>.
- 2268 Faas, G. C. et al. (Mar. 2011). “Calmodulin as a direct detector of Ca²⁺ signals”. In: *Nature
2269 neuroscience* 14.3, pp. 301–304. DOI: [10.1038/nrn.2746](https://doi.org/10.1038/nrn.2746). URL: <https://doi.org/10.1038/nrn.2746>.
- 2271 Fiala, John C. and Kristen M. Harris (1999). *Dendrite Structure*.
- 2272 Flach, Boris (Sept. 2013). “A Class of Random Fields on Complete Graphs with Tractable
2273 Partition Function”. In: *IEEE transactions on pattern analysis and machine intelligence*
2274 35, pp. 2304–6. DOI: [10.1109/TPAMI.2013.99](https://doi.org/10.1109/TPAMI.2013.99).
- 2275 Forney, G. D. (1973). “The viterbi algorithm”. In: *Proceedings of the IEEE* 61.3, pp. 268–
2276 278. ISSN: 1558-2256. DOI: [10.1109/PROC.1973.9030](https://doi.org/10.1109/PROC.1973.9030).
- 2277 Fosdick, Bailey et al. (Aug. 2016). “Configuring Random Graph Models with Fixed Degree
2278 Sequences”. In: *SIAM Review* 60. DOI: [10.1137/16M1087175](https://doi.org/10.1137/16M1087175).
- 2279 Friedrich, Johannes and Liam Paninski (2016). “Fast Active Set Methods for Online Spike
2280 Inference from Calcium Imaging”. In: *Advances in Neural Information Processing Systems* 29. Ed. by D. D. Lee et al. Curran Associates, Inc., pp. 1984–1992. URL: <http://papers.nips.cc/paper/6505-fast-active-set-methods-for-online-spike-inference-from-calcium-imaging.pdf>.

- 2284 Ganmor, Elad, Ronen Segev, and Elad Schneidman (2011). “Sparse low-order interaction
2285 network underlies a highly correlated and learnable neural population code”. In: *Proceed-
2286 ings of the National Academy of Sciences* 108.23, pp. 9679–9684. ISSN: 0027-8424. DOI:
2287 [10.1073/pnas.1019641108](https://doi.org/10.1073/pnas.1019641108). eprint: <https://www.pnas.org/content/108/23/9679.full.pdf>. URL: <https://www.pnas.org/content/108/23/9679>.
- 2290 Girard, P., J. M. Hupé, and J. Bullier (2001). “Feedforward and Feedback Connections Be-
2291 tween Areas V1 and V2 of the Monkey Have Similar Rapid Conduction Velocities”. In:
2292 *Journal of Neurophysiology* 85.3. PMID: 11248002, pp. 1328–1331. DOI: [10.1152/jn.2001.85.3.1328](https://doi.org/10.1152/jn.2001.85.3.1328). eprint: <https://doi.org/10.1152/jn.2001.85.3.1328>. URL: <https://doi.org/10.1152/jn.2001.85.3.1328>.
- 2295 Greenberg, David et al. (Nov. 2018). “Accurate action potential inference from a calcium
2296 sensor protein through biophysical modeling:” in: DOI: [10.1101/479055](https://doi.org/10.1101/479055).
- 2297 Gründemann, Jan et al. (2019). “Amygdala ensembles encode behavioral states”. In: *Science*
2298 364.6437. ISSN: 0036-8075. DOI: [10.1126/science.aav8736](https://doi.org/10.1126/science.aav8736). eprint: <https://science.sciencemag.org/content/364/6437/eaav8736.full.pdf>. URL: <https://science.sciencemag.org/content/364/6437/eaav8736>.
- 2302 Hodgkin, A. L. and A. F. Huxley (1939). “Action Potentials Recorded from Inside a Nerve Fi-
2303 bre”. In: *Nature* 144.3651, pp. 710–711. ISSN: 1476-4687. DOI: [10.1038/144710a0](https://doi.org/10.1038/144710a0).
2304 URL: <https://doi.org/10.1038/144710a0>.
- 2305 Humphries, Mark et al. (Jan. 2019). “Spectral rejection for testing hypotheses of structure in
2306 networks”. In:
- 2307 Humphries, Mark D. (2011). “Spike-Train Communities: Finding Groups of Similar Spike
2308 Trains”. In: *Journal of Neuroscience* 31.6, pp. 2321–2336. ISSN: 0270-6474. DOI: [10.1523/JNEUROSCI.2853-10.2011](https://doi.org/10.1523/JNEUROSCI.2853-10.2011). eprint: <https://www.jneurosci.org/content/31/6/2321.full.pdf>. URL: <https://www.jneurosci.org/content/31/6/2321>.
- 2312 Jun, James J. et al. (2017). “Fully integrated silicon probes for high-density recording of
2313 neural activity”. In: *Nature* 551.7679, pp. 232–236. ISSN: 1476-4687. DOI: [10.1038/nature24636](https://doi.org/10.1038/nature24636). URL: <https://doi.org/10.1038/nature24636>.

- 2315 Kilhoffer, Marie-Claude et al. (Sept. 1992). “Use of Engineered Proteins With Internal Tryp-
2316 tophean Reporter Groups and Perturbation Techniques to Probe the Mechanism of Ligand-
2317 Protein Interactions: Investigation of the Mechanism of Calcium Binding to Calmod-
2318 ulin”. In: *Biochemistry* 31.34, pp. 8098–8106. DOI: [10.1021/bi00149a046](https://doi.org/10.1021/bi00149a046). URL:
2319 <https://doi.org/10.1021/bi00149a046>.
- 2320 Koch, Christoff (1999). *Biophysics of Computation: Information Processing in Single Neu-*
2321 *rons*. Oxford University Press. ISBN: ISBN 0-19-510491-9.
- 2322 Kolaczyk, Eric and Haiying Huang (Sept. 2010). “Multiscale Statistical Models for Hier-
2323 archical Spatial Aggregation”. In: *Geographical Analysis* 33, pp. 95 –118. DOI: [10.1111/j.1538-4632.2001.tb00439.x](https://doi.org/10.1111/j.1538-4632.2001.tb00439.x).
- 2325 Lee, Suk-HO et al. (July 2000). “Differences in Ca²⁺ buffering properties between excitatory
2326 and inhibitory hippocampal neurons from the rat”. In: *The Journal of Physiology* 525.
2327 DOI: [10.1111/j.1469-7793.2000.t01-3-00405.x](https://doi.org/10.1111/j.1469-7793.2000.t01-3-00405.x).
- 2328 Litwin-Kumar, Ashok, Maurice Chacron, and Brent Doiron (Sept. 2012). “The Spatial Struc-
2329 ture of Stimuli Shapes the Timescale of Correlations in Population Spiking Activity”.
2330 In: *PLoS computational biology* 8, e1002667. DOI: [10.1371/journal.pcbi.1002667](https://doi.org/10.1371/journal.pcbi.1002667).
- 2332 Maravall, M et al. (May 2000). “Estimating intracellular calcium concentrations and buffer-
2333 ing without wavelength ratioing”. In: *Biophysical Journal* 78.5, pp. 2655–2667. DOI:
2334 [10.1016/S0006-3495\(00\)76809-3](https://doi.org/10.1016/S0006-3495(00)76809-3). URL: [https://doi.org/10.1016/S0006-3495\(00\)76809-3](https://doi.org/10.1016/S0006-3495(00)76809-3).
- 2336 Maugis, Pa (Jan. 2014). “Event Conditional Correlation: Or How Non-Linear Linear Depen-
2337 dence Can Be”. In:
- 2338 Meilă, Marina (2007). “Comparing clusterings—an information based distance”. In: *Journal*
2339 *of Multivariate Analysis* 98.5, pp. 873 –895. ISSN: 0047-259X. DOI: <https://doi.org/10.1016/j.jmva.2006.11.013>. URL: <http://www.sciencedirect.com/science/article/pii/S0047259X06002016>.
- 2342 Murray, John D. et al. (2014). “A hierarchy of intrinsic timescales across primate cortex”.
2343 In: *Nature Neuroscience* 17.12, pp. 1661–1663. ISSN: 1546-1726. DOI: [10.1038/nn.3862](https://doi.org/10.1038/nn.3862). URL: <https://doi.org/10.1038/nn.3862>.
- 2345 Neher, E. and G. J. Augustine (1992). “Calcium gradients and buffers in bovine chromaffin
2346 cells”. eng. In: *The Journal of physiology* 450. 1331424[pmid], pp. 273–301. ISSN: 0022-
2347 3751. DOI: [10.1113/jphysiol.1992.sp019127](https://doi.org/10.1113/jphysiol.1992.sp019127). URL: <https://pubmed.ncbi.nlm.nih.gov/1331424>.

- 2349 O'Donnell, Cian et al. (Jan. 2017). "The population tracking model: a simple, scalable statis-
2350 tical model for neural population data". English. In: *Neural Computation* 29.1, pp. 50–
2351 93. ISSN: 0899-7667. DOI: [10.1162/NECO_a_00910](https://doi.org/10.1162/NECO_a_00910).
- 2352 Ouzounov, Dimitre G. et al. (2017). "In vivo three-photon imaging of activity of GCaMP6-
2353 labeled neurons deep in intact mouse brain". eng. In: *Nature methods* 14.4. 28218900[pmid],
2354 pp. 388–390. ISSN: 1548-7105. DOI: [10.1038/nmeth.4183](https://doi.org/10.1038/nmeth.4183). URL: <https://pubmed.ncbi.nlm.nih.gov/28218900>.
- 2355 Patterson, Carolyn A. et al. (2014). "Similar adaptation effects in primary visual cortex and
2356 area MT of the macaque monkey under matched stimulus conditions". In: *Journal of Neu-
2357 rophysiology* 111.6. PMID: 24371295, pp. 1203–1213. DOI: [10.1152/jn.00030.2013](https://doi.org/10.1152/jn.00030.2013).
2358 eprint: <https://doi.org/10.1152/jn.00030.2013>. URL: <https://doi.org/10.1152/jn.00030.2013>.
- 2359 Peron, Simon P. et al. (2015). "A Cellular Resolution Map of Barrel Cortex Activity during
2360 Tactile Behavior". In: *Neuron* 86.3, pp. 783–799. ISSN: 0896-6273. DOI: [10.1016/j.neuron.2015.03.027](https://doi.org/10.1016/j.neuron.2015.03.027). URL: <https://doi.org/10.1016/j.neuron.2015.03.027>.
- 2361 Pnevmatikakis, E.A. et al. (Jan. 2016). "Simultaneous Denoising, Deconvolution, and Demix-
2362 ing of Calcium Imaging Data". In: *Neuron* 89.2, pp. 285–299. DOI: [10.1016/j.neuron.2015.11.037](https://doi.org/10.1016/j.neuron.2015.11.037). URL: <https://doi.org/10.1016/j.neuron.2015.11.037>.
- 2363 Pnevmatikakis, Eftychios et al. (Nov. 2013). "Bayesian spike inference from calcium imaging
2364 data". In: *Conference Record - Asilomar Conference on Signals, Systems and Computers*.
DOI: [10.1109/ACSSC.2013.6810293](https://doi.org/10.1109/ACSSC.2013.6810293).
- 2365 Pnevmatikakis, Eftychios et al. (Sept. 2014). "A structured matrix factorization framework
2366 for large scale calcium imaging data analysis". In:
- 2367 Schneidman, Elad et al. (2006). "Weak pairwise correlations imply strongly correlated net-
2368 work states in a neural population". eng. In: *Nature* 440.7087. 16625187[pmid], pp. 1007–
2369 1012. ISSN: 1476-4687. DOI: [10.1038/nature04701](https://doi.org/10.1038/nature04701). URL: <https://pubmed.ncbi.nlm.nih.gov/16625187>.
- 2370 Shannon, C. E. (1948). "A Mathematical Theory of Communication". In: *Bell System Techni-
2371 cal Journal* 27.3, pp. 379–423. DOI: [10.1002/j.1538-7305.1948.tb01338.x](https://doi.org/10.1002/j.1538-7305.1948.tb01338.x).
2372 eprint: <https://onlinelibrary.wiley.com/doi/pdf/10.1002/j.1538-7305.1948.tb01338.x>. URL: <https://onlinelibrary.wiley.com/doi/abs/10.1002/j.1538-7305.1948.tb01338.x>.

- 2383 Shimazaki, Hideaki et al. (2012). “State-space analysis of time-varying higher-order spike
2384 correlation for multiple neural spike train data”. eng. In: *PLoS computational biology* 8.3.
2385 22412358[pmid], e1002385–e1002385. ISSN: 1553-7358. DOI: [10.1371/journal.pcbi.1002385](https://doi.org/10.1371/journal.pcbi.1002385). URL: <https://pubmed.ncbi.nlm.nih.gov/22412358>.
- 2387 Staude, Benjamin, Sonja Grün, and Stefan Rotter (2010). “Higher-Order Correlations and
2388 Cumulants”. In: *Analysis of Parallel Spike Trains*. Ed. by Sonja Grün and Stefan Rotter.
2389 Boston, MA: Springer US, pp. 253–280. ISBN: 978-1-4419-5675-0. DOI: [10.1007/978-1-4419-5675-0_12](https://doi.org/10.1007/978-1-4419-5675-0_12). URL: https://doi.org/10.1007/978-1-4419-5675-0_12.
- 2392 Stein, Astrid von and Johannes Sarnthein (2000). “Different frequencies for different scales
2393 of cortical integration: from local gamma to long range alpha/theta synchronization”. In:
2394 *International Journal of Psychophysiology* 38.3, pp. 301 –313. ISSN: 0167-8760. DOI:
2395 [https://doi.org/10.1016/S0167-8760\(00\)00172-0](https://doi.org/10.1016/S0167-8760(00)00172-0). URL: <http://www.sciencedirect.com/science/article/pii/S0167876000001720>.
- 2397 Steinmetz, Nick, Matteo Carandini, and Kenneth D. Harris (2019). ”*Single Phase3*” and
2398 ”*Dual Phase3*” *Neuropixels Datasets*. DOI: [10.6084/m9.figshare.7666892.v2](https://doi.org/10.6084/m9.figshare.7666892.v2). URL: https://figshare.com/articles/dataset/_Single_Phase3_Neuropixels_Dataset/7666892/2.
- 2401 Steinmetz, Nick et al. (Mar. 2019). “Eight-probe Neuropixels recordings during sponta-
2402 neous behaviors”. In: DOI: [10.25378/janelia.7739750.v4](https://doi.org/10.25378/janelia.7739750.v4). URL: <https://doi.org/10.25378/janelia.7739750.v4>. URL: https://janelia.figshare.com/articles/Eight-probe_Neuropixels_recordings_during_spontaneous_behaviors/7739750.
- 2405 Stringer, Carsen et al. (2019). “Spontaneous behaviors drive multidimensional, brainwide ac-
2406 tivity”. In: *Science* 364.6437. ISSN: 0036-8075. DOI: [10.1126/science.aav7893](https://doi.org/10.1126/science.aav7893).
2407 eprint: <https://science.sciencemag.org/content/364/6437/eaav7893.full.pdf>. URL: <https://science.sciencemag.org/content/364/6437/eaav7893>.
- 2410 Tada, Mayumi et al. (2014). “A highly sensitive fluorescent indicator dye for calcium imag-
2411 ing of neural activity in vitro and in vivo”. In: *European Journal of Neuroscience* 39.11,
2412 pp. 1720–1728. DOI: [10.1111/ejn.12476](https://doi.org/10.1111/ejn.12476). eprint: <https://onlinelibrary.wiley.com/doi/pdf/10.1111/ejn.12476>. URL: <https://onlinelibrary.wiley.com/doi/abs/10.1111/ejn.12476>.
- 2415 Tian, Lin et al. (2009). “Imaging neural activity in worms, flies and mice with improved
2416 GCaMP calcium indicators”. eng. In: *Nature methods* 6.12. 19898485[pmid], pp. 875–

- 2417 881. ISSN: 1548-7105. DOI: [10.1038/nmeth.1398](https://doi.org/10.1038/nmeth.1398). URL: <https://pubmed.ncbi.nlm.nih.gov/19898485>.
- 2418
- 2419 Tkačik, Gašper et al. (2014). “Searching for collective behavior in a large network of sen-
2420 sory neurons”. eng. In: *PLoS computational biology* 10.1. 24391485[pmid], e1003408–
2421 e1003408. ISSN: 1553-7358. DOI: [10.1371/journal.pcbi.1003408](https://doi.org/10.1371/journal.pcbi.1003408). URL:
2422 <https://pubmed.ncbi.nlm.nih.gov/24391485>.
- 2423 Treves, Alessandro and Stefano Panzeri (1995). “The Upward Bias in Measures of Informa-
2424 tion Derived from Limited Data Samples”. In: *Neural Computation* 7.2, pp. 399–407.
2425 DOI: [10.1162/neco.1995.7.2.399](https://doi.org/10.1162/neco.1995.7.2.399). eprint: <https://doi.org/10.1162/neco.1995.7.2.399>. URL: <https://doi.org/10.1162/neco.1995.7.2.399>.
- 2426
- 2427
- 2428 Vinh, Nguyen Xuan, Julien Epps, and James Bailey (Dec. 2010). “Information Theoretic
2429 Measures for Clusterings Comparison: Variants, Properties, Normalization and Correc-
2430 tion for Chance”. In: *J. Mach. Learn. Res.* 11, 2837–2854. ISSN: 1532-4435.
- 2431 Vogelstein, Joshua T. et al. (Oct. 2010). “Fast nonnegative deconvolution for spike train infer-
2432 ence from population calcium imaging”. In: *Journal of neurophysiology* 104.6, 295–300.
2433 DOI: [10.1152/jn.01073.2009](https://doi.org/10.1152/jn.01073.2009). URL: <https://doi.org/10.1152/jn.01073.2009>.
- 2434
- 2435 Wierzynski, ”Casimir M. et al. (”2009”). ”State-Dependent Spike-Timing Relationships be-
2436 tween Hippocampal and Prefrontal Circuits during Sleep””. In: ”*Neuron*” ”61.””4”, ”587
2437 –596”. ISSN: ”0896-6273”. DOI: <https://doi.org/10.1016/j.neuron.2009.01.011>. URL: <http://www.sciencedirect.com/science/article/pii/S0896627309000786>.
- 2436
- 2437
- 2438
- 2439
- 2440 Zariwala, Hatim A. et al. (2012). “A Cre-dependent GCaMP3 reporter mouse for neuronal
2441 imaging in vivo”. eng. In: *The Journal of neuroscience : the official journal of the Society
2442 for Neuroscience* 32.9. 22378886[pmid], pp. 3131–3141. ISSN: 1529-2401. DOI: [10.1523/JNEUROSCI.4469-11.2012](https://doi.org/10.1523/JNEUROSCI.4469-11.2012). URL: <https://pubmed.ncbi.nlm.nih.gov/22378886>.
- 2441
- 2442
- 2443
- 2444
- 2445 Zou, Hui and Trevor Hastie (2005). “Regularization and variable selection via the Elastic
2446 Net”. In: *Journal of the Royal Statistical Society, Series B* 67, pp. 301–320.